SISSA ISAS

SCUOLA INTERNAZIONALE SUPERIORE DI STUDI AVANZATI
INTERNATIONAL SCHOOL FOR ADVANCED STUDIES

AB-INITIO STUDY ON SYNTHESIS OF NEW MATERIALS AT HIGH PRESSURE

transition-metal nitrides and non-molecular CO_2 phases

Thesis submitted for the degree of
Doctor Philosophiæ

Candidate:

Javier Antonio Montoya Martinez

Supervisors:

Prof. Sandro Scandolo
and
Prof. Roger Rousseau

October 2007

TO NICOLAS

Contents

PART I **3**

1 Introduction **5**

2 Methodology **9**
2.1 Ab-initio calculations 9
2.1.1 The crystal Hamiltonian 9
2.1.2 The Born-Oppenheimer approach 10
2.1.3 Density as basic variable 11
2.1.4 Density Functional Theory 12
2.1.5 The Hohenberg-Kohn theorem 13
2.1.6 The Kohn-Sham ansatz 15
2.1.7 Generalized Gradient Approximation (GGA) 16
2.2 Molecular Dynamics (MD) 17
2.2.1 Classical MD 17
2.2.2 Ab-initio MD 19
2.2.3 Car-Parrinello MD 19
2.2.4 Variable cell 21
2.3 The link between dynamic and electronic properties 23
2.3.1 Linear response 23
2.3.2 Force theorem 24
2.3.3 Density Functional Perturbation Theory (DFPT) 25
2.4 Plane waves and pseudo-potentials 26
2.5 The Quantum-Espresso package 28

PART II **31**

3 Nitrides **33**
3.1 PtN_2 35
3.1.1 Introduction 35

3.1.2 Methodology . . . 35
3.1.3 Results and discussion . . . 36
3.1.4 Beyond PtN_2-pyrite . . . 48
3.1.5 Conclusions . . . 49
3.2 OsN_2 . . . 50
3.2.1 Introduction . . . 50
3.2.2 Methodology . . . 51
3.2.3 Results and discussion . . . 52
3.2.4 Superconductivity in OsN_2 . . . 56
3.2.5 Conclusions . . . 64

4 CO_2 65
4.1 Amorphous phase . . . 69
4.1.1 Introduction . . . 69
4.1.2 Methodology . . . 70
4.1.3 Results and discussion . . . 71
4.1.4 Conclusions . . . 77
4.2 Catalysis of extended CO_2 phases . . . 78
4.2.1 Introduction . . . 78
4.2.2 Methodology . . . 80
4.2.3 Simulation protocol . . . 82
4.2.4 Results and discussion . . . 86
4.2.5 Conclusions . . . 92

5 Conclusions 95

Appendices 96

A Some useful conversion tables 97

B Pseudo-potential tests on platinum and nitrogen 99
B.1 Platinum crystal . . . 99
B.2 Nitrogen molecule . . . 100

C Input-file example for fpmd.x 105

PART I

Chapter 1

Introduction

Despite the tremendous growth of high-pressure research in the last two or three decades, this is not a new topic in experimental physics, also it is not true that it started being relevant only after the Nobel prize awarded to Percy W. Bridgman in 1946, or after the dawn of the atomic era with the megabar pressures created by atomic explosions. The history of high-pressure experiments is strongly linked, instead, to the history of man-made diamonds, in fact, a book exists that contains a romantic and detailed description of the many enterprises that took place in history and the procedures used by the so-called "diamond makers" [1]. When heated up to very high temperatures diamonds burn and disappear, and it was observed, to the great surprise of scientists in the 18th century, that the only byproduct that remained after such combustion process was simply CO_2. Soon after that, people realized that diamonds were made out of pure carbon in a particular and very stable atomic configuration, and so, the hunt to the artificially-made diamond began. After decades of research trying to mimic the natural pressure and temperature conditions at which natural diamonds are created, by continuously improving on the experimental techniques, and also after tens of false or non-reproducible claims of man-made diamonds, finally in December of 1954, a small research group formed by not more than five members at General Electric's Labs., succeeded in synthesizing reproducibly the first artificial diamonds in history. First synthetic diamonds were obtained in very small quantities in the form of very tiny grains, but nowadays artificial diamonds are a huge industry generating giant revenues to the companies that produce them, and with an always increasing base of clients, which look for them mainly due to their unique mechanical and optical properties, that imply also a wide range of applications in industrial processes.

The discovery, in more recent years, of a huge amount of novel materials com-

ing from high pressures which are interesting both, from the point of view of their possible technological applications and for their contribution to the basic understanding of the electronic processes leading to rupture and formation of atomic bonds, has been made possible by the huge progress in the last decades in three fronts of high pressure technology, namely the extension of maximum attainable pressure, the development of multiple analytical techniques for *in-situ* characterization, and the order-of-magnitude improvements in accuracy and sensitivity of measurements at megabar pressures.

Electronic-structure models predict that, in the very high pressure regime, all materials tend to transform into a metallic phase due to the small distances separating the atoms, which favor the overlapping of atomic orbitals between neighbors and electron delocalization. However, before this event takes place there is a huge amount of states that materials under high-pressure can access. Such variety of states has lead to the discovery and synthesis in recent years of new: superconductors, superhard, superionic, and non-linear optic materials [2, 3, 4, 5, 6], among many others. There exist also some reports of abrupt volume decrease in some materials upon application of pressure [7, 8] even without a change in structure, which has been attributed to some sort of electronic collapse after the reorganization/mixing of the most external electronic levels. In general, the study of all such varieties of new phenomena is the most powerful motivation for scientists devoted to this area of research and, in particular, it served also as motivation for this thesis work in which, as we will see, it reflects in its broad scope and in the variety of generated perspectives.

High-pressure phenomena is one of the fields that have benefited more from computer simulations. In fact, contrary to experiments, where every minor increase in the maximum achievable pressure is considered as a major technical achievement, atomistic simulations at high pressure just require to confine the same number of particles in a smaller simulation box, with periodic boundary conditions, to achieve arbitrarily high pressures[1]. Following the previous order of ideas, it is not so surprising to find that one of the first systems (if not the first) that computer scientists tried to simulate intensively, in order to test the constant-pressure first-principles molecular dynamics was, indeed, compressed carbon and its transformation path from graphite to diamond. In simulations, the carbon to diamond transition was

[1]Technical problems can also be present here, so, the pressures that can be simulated cannot be arbitrarily high. However, most problems in a given range of pressures can be circumvented using different levels of first-principles techniques, if we are aware of them in advance.

correctly reproduced, revealing also details on the sequence of steps for this transformation that were previously unknown [9].

Now, I will proceed with a very brief description of the two main parts that form this thesis work, which are inspired by some new possibilities that high pressure has opened for the synthesis of new phases and compounds. The relevance of these new materials from a practical point of view, lies in the possibility of having them recovered to ambient conditions and then used in a wide variety of technical applications. The two examples covered here, include a new class of transition-metal nitrides, and the synthesis of extended forms of CO_2.

In Chapter 3, it is shown that the new family of late transition-metal nitrides: PtN_2, OsN_2 and IrN_2, all synthesized at similar conditions ($\sim$ 50 GigaPascal and 2000 K) [10, 11], shares common structural properties among its members and opens the door to the synthesis of novel materials of this kind; with possible technological applications since they can be recovered to ambient conditions. The synthesis of these new nitrides is a clear example of how pressure can be used to form compounds between species that do not mix at ambient conditions.

Chapter 4 reports our studies on a different class of high pressure synthesis, namely the chemical transformation of a molecular species (CO_2) into an extended compound with entirely different mechanical and electronic properties. In particular it reports on the transition that molecular CO_2 undergoes at pressures above 40GPa and mild temperatures, into an extended glassy phase. CO_2's pressure-induced phase-transition from a molecular to an extended phase was first observed in 1999 when V. Iota and collaborators at Livermore, obtained a fully tetrahedral silica-like phase of CO_2 whose precise structure remains unresolved up to these days [12]. Recently, two new extended phases that show strong similarities among themselves in many aspects, have been reported [13, 14]. The first [13], is a non-molecular amorphous phase named "a-CO_2" or "carbonia", while the second [14], is a crystalline phase indexed by its discoverers as stishovite-like, i.e. with six-fold coordinated carbon atoms, that instead we believe is the crystalline counterpart of carbonia. However, in contrast with what is observed in the case of the transition-metal nitrides, for CO_2 no recovery of any of the new extended phases to ambient conditions has yet been possible. In fact, it is observed that a-CO_2 and phase VI go back to molecular phases at pressures around 20 GPa which coincides with the pressure at which the crossing between the enthalpies corresponding to the molecular and tetrahedral phases takes place.

Finally, also in Chapter 4, I consider some first-principles high-pressure chemistry applied to the problem of the catalysis and recovery of new CO_2 extended phases. Here, I will show that by means of introducing a transition metal (TM) as an impurity (Ti in our case) in a CO_2 molecular sample (2% concentration) an activation of the amorphization reaction is observed and this leads to a transition that occurs much faster than in the case in which no TM is used. It is also expected that attempts succeeding to lower the transition pressure, will also lead to a lowering of the pressures at which the CO_2's non-molecular phases can be recovered, with the final goal of bringing them to ambient conditions.

In summary, in this thesis it is shown how first-principles calculation techniques can be effectively used in high-pressure physics and chemistry research for clarifying very important issues regarding structural and electronic properties that wouldn't be easily accessible by other means.

Chapter 2

Methodology

In the forthcoming chapters of this work many different methodologies based on ab-initio techniques will be frequently employed, so, even if the core of the present work consists exclusively of applications of such techniques to high pressure physics and not of their development, still, a chapter explaining these methods seems necessary and is included here for the sake of completeness. The different aspects treated in this chapter have already been covered thoroughly in different books and reviews [15, 16, 17, 18] from which I have borrowed different pieces, gluing them together in a way that seemed to me as a convenient one for the understanding of the subsequent chapters of this work.

2.1 Ab-initio calculations

In ab-initio calculations, the goal is to perform the complete quantum-mechanical treatment of the many-body problem. In the following sections I will describe how, even if achieving this goal is not always possible, in practice the problem still can be addressed by applying some physical considerations so that we can then impose reasonable approximations to the full problem.

2.1.1 The crystal Hamiltonian

First of all, I am going to describe the crystal Hamiltonian; which is the one that in principle contains all the physics of the many-body system. From its solution, we could then derive all the observable quantities. Its form is:

$$\begin{aligned} \mathrm{H} \;=\; & \sum_i \left(-\frac{\hbar^2}{2m} \nabla_i^2 \right) \;+\; \sum_\alpha \left(-\frac{\hbar^2}{2M_\alpha} \nabla_\alpha^2 \right) \;+ \\ & \frac{1}{2} \sum_{i \neq j} \frac{e^2}{r_{ij}} + \frac{1}{2} \sum_{\alpha \neq \beta} \frac{Z_\alpha Z_\beta e^2}{R_{\alpha\beta}} - \sum_{i,\alpha} \frac{Z_\alpha e^2}{|r_i - R_\alpha|}. \end{aligned} \tag{2.1}$$

The first term is the electronic kinetic energy, where m is the electronic mass and ∇_i^2 the Laplacian acting over the electronic coordinates $\{r_i\}$. The second term is the energy corresponding to the motion of the nuclei, where M_α is the nuclear mass and ∇_α^2 is the Laplacian acting over the nuclear coordinates $\{R_\alpha\}$. The third and fourth terms are the pairwise electrostatic electron-electron and nucleus-nucleus interactions respectively, where: $r_{ij} = |r_i - r_j|$ and $R_{\alpha\beta} = |R_\alpha - R_\beta|$ are the electron-electron and nucleus-nucleus separations of the pairs which are being considered, and Z_α represents the charge of the αth nucleus. Finally, the fifth term corresponds to the electron-nuclei attraction.

From the Hamiltonian given above, is clear that the number of independent variables in the corresponding Schrödinger's equation is determined by the number of particles involved (which for a macroscopic crystal is of the order of $10^{23} cm^{-3}$). Therefore, an exact solution to such kind of equation is not possible for realistic systems. Hence, when dealing with this kind of problems, people very often try to work them out by applying different successive approximations in order to model the physics of the system, which, in some cases, can compromise the accuracy of the final result or provide results that are not so general. In general, this can lead to non first-principles models (i.e. models containing external parameters) which will work well for only a few kinds of systems and external conditions.

Very frequently, the first approximation that people do is the adiabatic (or *Born-Oppenheimer* [19]) approximation. This one is not very critical in terms of loss of accuracy, and instead simplifies considerably our problem so, next, I am going to present a short description of what it is about.

2.1.2 The Born-Oppenheimer approach

If we divide the system into light particles (electrons) and heavy ones (atomic nuclei), in thermodynamic equilibrium the mean value for the kinetic energy of both kind of particles is of the same order but, due to the big mass difference between protons+neutrons and electrons, the electronic velocities are

much faster than the nuclear ones (approximately two orders of magnitude). Then, for every modification in the position of the atomic nuclei an almost instantaneous rearrangement of the electrons occurs, following the new nuclear positions. This allows us to consider, at least to a first approximation, the movement of the electrons as if they were in an irrotational field due to *fixed* nuclei. While studying the movement of the nuclei, on the contrary, only the potential originated by the mean electronic spatial distribution (and not the instantaneous one) must be taken into account. This kind of approach, is the one which is commonly known as the *adiabatic* or *Born-Oppenheimer approximation*.

Within this framework Schrödinger's equation can be rewritten as:

$$\left(-\sum_{\alpha} \frac{\hbar^2}{2M_\alpha} \nabla_\alpha^2 + E_0(R) \right) \Phi(R) = \varepsilon \Phi(R) \tag{2.2}$$

where $R \equiv \{R_\alpha\}$ is the set of all the nuclear coordinates and $E_0(R)$ the clamped-ion energy of the system, which is often referred to as the *Born-Oppenheimer energy surface*, and $\Phi(R)$ are the atomic eigenvalues. In practice, $E_0(R)$ is the ground-state energy of a system of interacting electrons moving in the field of fixed nuclei, which obeys the Schrödinger's equation $H_{BO}(R)\varphi_n = E_n(R)\varphi_n$ where the Hamiltonian —which acts onto the electronic variables and depends only parametrically upon R— reads

$$H_{BO}(R) = -\frac{\hbar^2}{2m} \sum_i \nabla_i^2 + \frac{e^2}{2} \sum_{i \neq j} \frac{1}{r_{ij}} + \frac{e^2}{2} \sum_{\alpha \neq \beta} \frac{Z_\alpha Z_\beta}{R_{\alpha\beta}} - \sum_{i,\alpha} \frac{Z_\alpha e^2}{|r_i - R_\alpha|}. \tag{2.3}$$

This could be simply taken as a rearrangement of equation 2.1, but it is important to notice that now the electronic part is decoupled from the rest and can be solved independently, using the set of nuclear positions R, only as parameters.

2.1.3 Density as basic variable

In the Born-Oppenheimer approximation, nuclear coordinates act as parameters in the electronic Hamiltonian, $H_{BO}(R)$, whose ground-state energy is found by minimizing iteratively its expectation value with respect to the electronic density. To see this, let's consider the energy surface $E_0(R)$ appearing in Schrödinger's equation for the nuclei (Eq. 2.2); we will then have:

$$E_0(R) = \langle \varphi_0(r,R) \left| H_{BO}(R) \right| \varphi_0(r,R) \rangle \tag{2.4}$$

where $\varphi_0(r,R)$ is the electronic ground-state wave function of the Born-Oppenheimer Hamiltonian, $r \equiv \{r_i\}$ the set of all the electronic coordinates and $R \equiv \{R_\alpha\}$. This Hamiltonian depends on R via the electron-nucleus interaction that couples to the electronic degrees of freedom only through the electron charge density. Therefore, this expression can be written as:

$$E_0(R) = \underbrace{\int n_R(r) \overbrace{\left(\sum_{i,\alpha} \frac{Z_\alpha e^2}{|r_i - R_\alpha|} \right)}^{V_R(r)} dr}_{e^- - nucleus\ interaction} - \underbrace{\overbrace{\left(\frac{e^2}{2} \sum_{\alpha \neq \beta} \frac{Z_\alpha Z_\beta}{R_{\alpha\beta}} \right)}^{E_N(R)}}_{completely\ nuclear\ part} + \underbrace{E_{ee}(n_R(r))}_{e^- - e^-\ interaction} \tag{2.5}$$

where $n_R(r)$ is the ground-state electron charge density corresponding to the nuclear configuration R and the completely nuclear part is just a number which can be calculated exactly for each of those configurations. In the E_{ee} term I have included the electron-electron interaction, which means: Hartree plus exchange and correlation terms. It has been also *assumed* here, that this last term can be written as a well defined function of the electronic density $n_R(r)$.

According to the preceding discussion: the calculation of the Born-Oppenheimer ground-state energy and, as we will see later, also the calculation of the derivatives of the energy surface with respect to the nuclear coordinates, require *only* a knowledge of the *electronic charge-density distribution*. This fact is nothing else than a special case of a much more general property of the systems of interacting electrons, known as the *Hohenberg and Kohn (1964) theorem*, which I will pass to describe.

2.1.4 Density Functional Theory

The fundamental tenet of density functional theory is that any property of a system of many interacting particles can be viewed as a functional of the ground-state density $n_0(r)$; that is, one scalar function of position $n_0(r)$, in principle, determines all the information in the many-body wave functions for the ground-state and all excited states. The existence proofs for such functionals, were given in the original works of Hohenberg and Kohn [20]

and of Mermin [21]. However, as easy to understand as they are, they provide no guidance whatsoever for constructing the functionals, and no exact functionals are known so far for any system of more than one electron.

Density Functional Theory (DFT) would remain a minor curiosity today if it were not for the ansatz made by Kohn and Sham [22], which has provided a way to make useful, approximate ground-state functionals for real systems of many electrons. The Kohn-Sham ansatz replaces the interacting many-body problem with an auxiliary independent particle problem with all many-body effects included in an exchange-correlation functional. This is an ansatz that, in principle, leads to *exact* calculations of properties of many-body systems using independent-particle methods —even though nobody until now knows the exact formulation for the functional which has to be minimized— and has made possible approximate formulations that have proved to be remarkably successful. For the present work I used extensively, the generalized gradient approximations (GGA's) to DFT. GGA is one of those successful, practical but approximate, formulations for the exchange-correlation functional (being this the crucial part in the Kohn-Sham approach as we will see) and allow us to obtain good ground-state elastic properties such as phonon modes and bulk modulus. During the following sections of this chapter we will try to go deeper into the details and motivations of this technique.

2.1.5 The Hohenberg-Kohn theorem

According to the Hohenberg-Kohn theorem [20], no two different potentials (different up to a constant) acting on the electrons of a given system, can give rise to a same ground-state electronic charge density. The prove is quite simple and follows after a reductio-ad-absurdum:

Let us assume that there are two external potentials $V_1(r)$ and $V_2(r)$ which differ by more than a constant and which lead the same ground-state electronic density. Then if we consider H_1 as being the Hamiltonian corresponding to $V_1(r)$ with Ψ_1 being the ground-state wave function associated with this Hamiltonian, and assuming equivalent definitions for $V_2(r)$, then follows that:

$$E_1 = \langle \Psi_1 | H_1 | \Psi_1 \rangle < \langle \Psi_2 | H_1 | \Psi_2 \rangle, \tag{2.6}$$

we are here assuming that these are non-degenerate ground-states so that, the inequality holds as stated in the previous formula. Now, using this expression and rearranging some terms:

$$\langle\Psi_2|H_1|\Psi_2\rangle = \langle\Psi_2|H_2|\Psi_2\rangle + \langle\Psi_2|H_1 - H_2|\Psi_2\rangle$$
$$= E_2 + \int [V_1(r) - V_2(r)] n_R^0(r) dr, \tag{2.7}$$

so that

$$E_1 < E_2 + \int [V_1(r) - V_2(r)] n_R^0(r) dr. \tag{2.8}$$

On the other hand if we consider E_2 in exactly the same way, we find the same kind of equation, with subscripts 1 and 2 interchanged,

$$E_2 < E_1 + \int [V_2(r) - V_1(r)] n_R^0(r) dr. \tag{2.9}$$

And finally, if we add together (2.8) and (2.9), we arrive at the contradictory inequality $E_1 + E_2 < E_1 + E_2$, which establishes the desired result: *there cannot be two different external potentials differing by more than a constant which give rise to the same non-degenerate ground-state charge density. Then, the density uniquely determines the external potential within a constant.*

This theorem provides the foundation of what is currently known as *density-functional theory* (DFT; Parr and Yang [23], 1989; Dreizler and Gross [24], 1990). It allows an enormous conceptual simplification of the ground-state properties of a system of interacting electrons, for it replaces the traditional description based on wave functions (which depend on 3N independent variables, N being the number of electrons) with a much more tractable description in terms of the charge density, which depends on only three variables.

To see this, let us take the ion-ion interaction energy (Eq. 2.5) as a reference point. Then we are left with the following expression which is the one that has to be minimized in order to obtain the ground-state energy and electronic density distribution:

$$E[n_R] = F[n_R] + \int n_R(r) V(r) dr. \tag{2.10}$$

Here we see that (as in equation 2.5) $V(r)$ is the external potential acting over the electronic charge density due to the ions, and it is the remaining part (the one represented by $F[n_R]$) the one which offers major difficulties. In fact there are two main problems: the first is that Hohenberg and Kohn didn't provide an exact form for the $F[n_R]$ functional, and the second is that

the conditions to be fulfilled for a function n_R to be considered an acceptable ground-state charge distribution (and hence domain of the functional F) are poorly characterized. About the last problem, one usually has to be content to impose the proper normalization of the charge density by the use of a Lagrange multiplier; and about the first problem, that is exactly what Kohn and Sham tried to address, so, in the next section we will give a short description of what they did.

2.1.6 The Kohn-Sham ansatz

As mentioned in the previous section, the Hohenberg and Kohn theorem, states that all the physical properties of a system of interacting electrons are uniquely determined by its ground-state charge density distribution. This property holds independently of the precise form of the electron-electron interaction. In particular when the strength of this interaction vanishes, the energy functional defines the ground-state kinetic energy of a system of non-interacting electrons, which can be used as a limiting case, or starting point, for the construction of a general functional. This fact was used by Kohn and Sham [22], to map the problem of a system of interacting electrons onto an equivalent non-interacting problem. To this end, the unknown energy functional can be cast in the form

$$F[n_R] = T_0[n_R] + \frac{e^2}{2}\int \frac{n_R(r)n_R(r')}{r-r'}drdr' + E_{xc}[n_R] \tag{2.11}$$

where $T_0[n_R]$ is the kinetic energy functional for the previously mentioned system of non-interacting electrons having a density $n_R(r)$, the second term is the classical electrostatic self-interaction of the electron charge-density distribution (also called: the *Hartree* term) and finally a new quantity, $E_{xc}[n_R]$, is defined and represents the so-called *exchange-correlation energy*. The only really unknown quantity is this exchange-correlation energy functional[1] and, in principle, the quality of the solution of the full many-body problem will be only limited by the quality of the approximation used for it.

In the weakly inhomogeneous case, where the deviation of the density is small from its homogeneous value, Kohn and Sham proposed that the exchange-correlation energy can be written as

$$E_{xc}[n_R] = \int n_R(r)\epsilon_{xc}[n_R(r)]dr \tag{2.12}$$

[1]Because the energy coming from $T_0[n_R]$ can be obtained in an indirect way, see for example [17].

where $\epsilon_{xc}[n_R(r)]$ is the exchange-correlation energy per particle of a homogeneous system of density n. This approximation implies that an inhomogeneous system is replaced by a piece-wise homogeneous system; precisely due to this, is that this *ansatz* is called: the *local density approximation* (LDA), which has been proved to demonstrate the outstanding capacities of the DFT, even when applied to not very homogeneous systems. In LDA, the only information that we still need to know exactly is the exchange-correlation energy of the homogeneous gas as a function of density; in this respect, the exchange energy of the homogeneous gas is given by a simple analytic form (Chapter 5 in Ref. [15]), while the correlation energy has been calculated to great accuracy with Monte Carlo methods [25, 26].

2.1.7 Generalized Gradient Approximation (GGA)

The first step beyond the local approximation, is a functional of the magnitude of the gradient of the density $|\nabla n^\sigma|$ as well as the value n at each point. However, it has been observed that such a "gradient expansion approximation" does not lead to consistent improvement over the LDA. The basic problem is that gradients in real materials are so large that the expansion breaks down. Indeed, the need for adding some preconditioning to the magnitude of such gradients, led to the development of the so-called generalized-gradient expansion from which the abbreviation "GGA" derives. Numerous recipes to construct such E_{xc} have been developed, some of them are parameter free while others require the fitting of some parameters, in order to fit to molecular data or to be able to extrapolate the parameter-free-accuracy obtained by for example using Monte-Carlo techniques, for atoms with few electrons (like He) to atoms that contain more electrons.

After evidence showing LDA for the exchange and correlation terms to perform much better than originally expected, it was, in general, believed that it could work well enough to describe the properties observed in many kinds of bulk solids (i.e. those that are not affected by strong electronic correlations) while it was known to be not so good for dealing with isolated molecules or with molecular crystals. For this reason, since its introduction by Langreth and Mehl in 1983 [27], twelve years had to pass before it was clearly established that GGA could indeed offer meaningful improvements over LDA, on the description of crystalline phases and their relative stabilities, particularly, when studying phase transitions that occur at high pressures [28]. This, then justified paying the considerable increase in computational resources typically required to carry out GGA calculations with respect to those needed for LDA.

Nowadays, the use of such approximations to the exchange and correlation energy has became a common practice among the ab-initio high-pressure community due mainly to further confirmations regarding the advantages of its use when comparisons between the LDA and GGA have been carried out. It is not to expect, however, that this claim will always be true since, very often, error cancellations make LDA appear in better agreement with observations (for example when trying to reproduce the inter-atomic distances in some particular crystals) but still, the GGA approach is, among the two, the one that from a fundamental point of view is supposed to be able to describe in a more accurate way the electron-electron exchange and correlation interactions. This is particularly true when dealing with open (or low-density) structures, where GGA is capable of a more accurate treatment of the exchange and correlation energy density, due to the fact that it performs better than LDA in regions with exponential charge-decay.

2.2 Molecular Dynamics (MD)

2.2.1 Classical MD

Molecular dynamics simulation is a technique used for computing the equilibrium and transport properties of a classical many-body system. In this context, the word "classical" means that the nuclear motion of the constituent parts obeys the laws of classical mechanics. This is an excellent approximation for a wide range of materials. Only when we consider the translational or rotational motion of light atoms or molecules (He, H_2, D_2) or vibrational motions with frequency ν such that $h\nu < k_B$T should we worry about quantum effects. The expression: "classical MD", is used when the calculation of the forces on the atoms is done by using model potentials that try to mimic the inter-ionic potential without directly having first-principles into account, this also means that on constructing those potentials some parameter fitting is also required if we want them to be reliable.

The idea behind molecular dynamics simulations is to enable us to mimic real experimental conditions, in this sense we proceed in the same way in both cases; first we prepare a sample of the material that we want to study, we set a mechanism for measuring observable quantities (e.g., a thermometer, manometer, viscometer, etc) and we establish a sampling rate for measuring those quantities. The system evolves following Newton's equations and since some time for equilibration is required, the more we let the system run the best are the statistics that we will get from our simulations, and this will

allow better estimations of the measured quantities, comparable to real-life experiments.

To measure an observable quantity in a Molecular Dynamics simulation we must, first of all, be able to express this observable as a function of the positions and momenta of the particles in the system. For instance, a convenient definition of temperature in a classical many-body system makes use of the equipartition theorem. Thus, we have:

$$\left\langle \frac{mv_\alpha^2}{2} \right\rangle = \frac{k_B T}{2} \tag{2.13}$$

In a simulation, we use this equation as an operational definition of the temperature. In practice, we would measure the total kinetic energy of the system and divide this by the number of degrees of freedom N_f. As the total kinetic energy of a system fluctuates, so does the instantaneous temperature:

$$T(t) = \sum_i \left(\frac{mv_i^2(t)}{k_B N_f} \right) \tag{2.14}$$

The relative fluctuations in the temperature will be of the order $(\frac{1}{\sqrt{N_f}})$. As N_f is typically on the order of $10^2 - 10^3$, the statistical fluctuations in the temperature are on the order of 5-10% . This, to say that in order to get an accurate estimate of the temperature, one should average over many fluctuations.

A typical MD program is constructed as follows:

1. We read in the parameters that specify the starting conditions of the system.

2. We compute the forces on all particles.

3. Finally, we integrate Newton's equations of motion. This step and the previous one constitute the core of the simulation and are repeated until we are satisfied with the equilibration+measuring time needed for our statistic averages.

4. After completion of the central loop (steps 2 and 3) we conclude computing and printing the average of measured quantities, and stop.

Very often, however, we need to modify the conditions of our simulation in order to see how our system reacts under the influence of changing external conditions like, for example, pressure and temperature. In order to do this, people have defined ways to achieve this goal without biasing the statistics collected from the system in too strong a way. These, and many other technicalities of MD simulations applied to high pressures, have been covered in a very satisfactory manner by many reviews (see [18, 29, 30], and references therein).

2.2.2 Ab-initio MD

The calculation of the force acting on every particle is the most time-consuming part of almost all Molecular Dynamics simulations. For the most simple case of pair-wise inter-atomic forces, the time needed for the evaluation of these forces if we use a simple functional form of the inter-atomic potential, scales as N^2. In "real" applications of the MD technique, more sophisticated and time-expensive algorithms for the analytical calculation of the forces are used, they include many-body terms, polarizabilities, and some parameters that have to be fitted to experiments. Those algorithms tend to be very precise, but are tuned for determined coordination numbers, pressures, temperatures and other environmental conditions that the researcher could prefer to change during the simulation. Then, a parameter-free algorithm for the force calculations become desirable. We can achieve this by employing an ab-initio Molecular Dynamics technique which uses atomic forces calculated from first principles, with no parametric dependence on the external conditions nor on the material itself. In its most crude version, this approach is known as the Born-Oppenheimer MD and it requires a full self-consistent density-functional minimization at every step in order to access the value of the energy and its derivatives at each point. This is possible only after a full quantum mechanical treatment of the problem, and is in this aspect where the Density Functional Theory, together with some concepts that I am going to develop in the next section regarding the way in which ab-initio forces are calculated, play a crucial role.

2.2.3 Car-Parrinello MD

For many reasons that have to do with the efficiency of the MD codes, it would be very appealing to have a clever first-principles approach that doesn't require the exact calculation of the electronic ground-state energy at every

step. This has been made possible by the use of the technique known as Car-Parrinello MD. This method, is a rather original and very efficient way to evolve the wave functions, and was proposed in 1985 by Roberto Car and Michele Parrinello [31]. Instead of solving very accurately the crystal Hamiltonian at each time step, they relaxed the constraint that the wave function be exactly in the ground-state. Then, the exact solution was replaced by a fictitious dynamics of the wave function about the exact ground-state. In the Car-Parrinello method, the solution of the Hamiltonian (Eq. 2.1) is replaced by the dynamical evolution of the following "extended" Lagrangian

$$\tilde{\mathcal{L}}_V = \frac{1}{2}\sum_i \mu\langle\dot{\varphi}_i|\dot{\varphi}_i\rangle + \frac{1}{2}\sum_I M_I\dot{R}_I^2 - E\left[\{\varphi_i\},\{R_I\}\right] + \sum_{i,j}\Lambda_{ij}\left(\langle\varphi_i|\varphi_j\rangle - \delta_{ij}\right). \tag{2.15}$$

where E is the DFT functional, expressed here in terms of the wave functions and also, parametrically, in terms of the positions of the nuclei, μ is a fictitious mass that can be used to control the time scale of the electronic dynamics, and Λ_{ij} are Lagrange multipliers that ensure the orthogonality of the wave functions. The equations of motion that can be obtained from the above Lagrangian are:

$$\mu\ddot{\varphi}_i = -\frac{\delta E}{\delta\varphi_i} + \sum_j \Lambda_{ij}\varphi_j \tag{2.16}$$

$$\ddot{R}_I = -\frac{1}{M_I}\frac{\partial E}{\partial R_I} \tag{2.17}$$

Equation 2.16 defines the dynamics of the wave functions, which will oscillate (by virtue of the second order time derivative) around the equilibrium condition

$$\frac{\delta E}{\delta\varphi_i} = \sum_j \Lambda_{ij}\varphi_j \tag{2.18}$$

Notice that equation 2.18 is the mathematical rephrasing of the DFT prescription of minimizing the DFT functional E with respect to variations of the (orthogonal) set of orbitals. Equation 2.17 instead coincides with Newton's equation under the influence of the first-principles interaction potential

$$V\left(R_1,\ldots,R_N\right) = \langle\varphi_0|H_{BO}\left(R_1,\ldots,R_N\right)|\varphi_0\rangle \tag{2.19}$$

with the only difference that the wave functions in 2.17 are not at the exact ground-state. The period of oscillation of the wave functions around the

ground-state, scales with $\mu^{\frac{1}{2}}$, which means that for a sufficiently small value of μ the oscillation can be made much faster that the typical time scales of the dynamics of the nuclei. In this limit, the effect of the fast oscillations averages out on the time scale of the dynamics of the nuclei, and the resulting net force on the nuclei is very similar to the force that would be calculated with the electrons in their ground-state. Further details on the Car-Parrinello method can be found in review papers [32, 33].

2.2.4 Variable cell

Thermodynamics imposes that in simulations, pressure - and not volume - should be the external "knob" that one should control in order to proceed with simulations in the same way as in experiments. Suppose for example that we are interested in the phase transformation of a material from phase A to phase B, with a large volume collapse (like in the case of the transition from graphite to diamond). Now, if we were to confine our collection of carbon atoms in a simulation box of fixed shape and volume, that fits initially the shape of the graphite crystal, then the direct transformation of the atomic positions from the graphite to the diamond-lattice would be strongly hindered by the energy cost required to fit the diamond lattice in the graphite box. This is so, because the atoms would need either to stretch or to compress some bonds, so that the new structure is able to fit in the old box, and in this way the system acquires elastic energy, and even surface energy if the transition to the new phase implies the creation of voids. Therefore, by proceeding in this way, density changes - a crucial driving force in most pressure-induced transitions - would not be allowed.

In order to overcome the limitations illustrated above, Parrinello and Rahman [34, 35] have extended the earlier idea, due to Andersen [36], of allowing the volume of the box to adjust according to the required pressure, and transformed the simulation box into a fully dynamical variable, driven by an appropriate equation of motion.

Considering a general simulation cell described by the matrix h_{ij}, we can see that the position of an atom inside the cell can be written as:

$$\mathbf{R_I} = \mathbf{hS_I} \tag{2.20}$$

where $\mathbf{S_I}$ is a vector representing the scaled position of atom $\mathbf{I}$, whose components vary between 0 and 1. In standard MD the cell $\mathbf{h}$ is kept fixed while the ionic degrees of freedom $\{\mathbf{R_I}\}$ (or equivalently $\{\mathbf{S_I}\}$) are allowed

to evolve. In the Parrinello-Rahman method instead, $\mathbf{h}$ and $\mathbf{S_I}$ are both independent degrees of freedom and their dynamics are obtained from the modified Lagrangian

$$\mathcal{L}_P = \frac{1}{2}\sum_{I=1}^{N} M_I |\mathbf{h}\dot{\mathbf{S}}_\mathbf{I}|^2 - V\left(\mathbf{hS_1}, \ldots, \mathbf{hS_N}\right) + \frac{1}{2} W \mathtt{Tr}(\dot{\mathbf{h}}^\mathbf{t}\dot{\mathbf{h}}) - P\Omega, \qquad (2.21)$$

where P is the pressure we want to impose, Ω is the cell volume ($\Omega = \mathrm{Det}(\mathbf{h})$), and W is the inertial mass of the cell, a fictitious parameter that controls the time scale of the cell dynamics.

The equations of motion that can be derived from the previous Lagrangian are:

$$\ddot{S}_I^\alpha = -\frac{1}{M_I}\frac{\partial V}{\partial R_I^\beta} h^{t\,-1}_{\beta\alpha} - G^{-1}_{\alpha\beta}\dot{G}_{\beta\gamma}\dot{S}_I^\gamma, \qquad (2.22)$$

$$\ddot{h}_{\alpha\beta} = \frac{1}{W}(\Pi_{\alpha\gamma} - P\delta_{\alpha\gamma})\Omega h^{t\,-1}_{\gamma\beta}, \qquad (2.23)$$

where Greek letters are cartesian indices, summations over repeated indices are assumed, and where

$$G_{\alpha\beta} = h_{\alpha\gamma}h_{\gamma\beta}. \qquad (2.24)$$

The stress tensor Π is defined as

$$\Pi_{\alpha\gamma} = \frac{1}{\Omega}\left(\sum_I M_I V_I^\alpha V_I^\gamma - \frac{\partial V}{\partial h_{\alpha\delta}} h^t_{\delta\gamma}\right), \qquad (2.25)$$

with

$$V_I^\alpha = h_{\alpha\gamma}\dot{S}_I^\gamma. \qquad (2.26)$$

The equations of motion for the atomic positions (Eq. 2.22) are modified with respect to the standard Newton's equations by the addition of a term that accounts for the variation of the metric tensor G, while a new equation of motion (Eq. 2.23) is introduced for the cell parameters. The dynamics of the cell in equation 2.23 is controlled by the imbalance between the imposed pressure and the instantaneously calculated value of the stress tensor (Eq. 2.25).

Although applied in a completely different context, it is easy to see the analogy between what has been discussed here for the variable cell and the ideas that underlie the Car-Parrinello MD approach discussed in the previous section, more details of this analogy are given in Ref. [29]. However, merging the constant-pressure (or equivalently: the variable-cell) method described here with the first principles Car-Parrinello method described in the previous section is not completely straightforward, and requires some care in the definition of how the wave functions change upon cell rescaling. By properly expressing the electronic wave-functions in scaled coordinates, it can be shown that it is possible to arrive at expressions for the equations of motion of atoms, electrons, and cell, which are completely analogous to the ones already derived in the last sections, the exact procedure required to do this has been described elsewhere [29, 37, 38, 39, 40].

2.3 The link between dynamic and electronic properties

2.3.1 Linear response

From the ground-state solution for the electronic Hamiltonian (equation 2.3) for every R, we are able to obtain the mentioned energy surface $E_0(R)$ which enters into the nuclear Schrödinger's equation (equation 2.2), thus determining the nuclear behavior.

Since the works of De Cicco and Johnson [41] and of Pick, Cohen and Martin [42], it is well known that the harmonic force-constants of crystals are determined by their static linear response, this establishes a connection between the dynamical matrices and the electronic properties of the material. Making use of the formalism just developed in previous sections, we can note that the equilibrium geometry of the system is given by the condition that the forces acting on individual nuclei vanish:

$$F_\alpha = -\frac{\partial E_0(R)}{\partial R_\alpha} = 0. \tag{2.27}$$

Whereas the vibrational frequencies ω are determined by the eigenvalues of the Hessian of the Born-Oppenheimer energy, scaled by the nuclear masses

$$det \left| \frac{1}{\sqrt{M_\alpha M_\beta}} \frac{\partial^2 E_0(R)}{\partial R_\alpha \partial R_\beta} - \omega^2 \right| = 0. \tag{2.28}$$

Then we have that: *the calculation of the equilibrium geometry and of the vibrational properties of a system thus amounts to computing the first and second derivatives of its Born-Oppenheimer energy surface.*

2.3.2 Force theorem

An extra advantage of the adiabatic approximation is that due to the assumption that the electrons equilibrate very fast after a nuclear movement, we can think of them as being always in a steady state, which is the fundamental condition for the Hellmann-Feynman force-theorem [43, 44] to be valid.

The force theorem states that the *first* derivative of the eigenvalues of a Hamiltonian, H_λ, that depends on a parameter λ is given by the expectation value of the derivative of the Hamiltonian, so it can be used in the following way

$$\frac{\partial E_\lambda}{\partial \lambda} = \left\langle \Psi_\lambda \left| \frac{\partial H_\lambda}{\partial \lambda} \right| \Psi_\lambda \right\rangle \tag{2.29}$$

where Ψ_λ is the eigenfunction of H_λ corresponding to the E_λ eigenvalue: $H_\lambda \Psi_\lambda = E_\lambda \Psi_\lambda$. Remembering now that, in the Born-Oppenheimer approximation, nuclear coordinates act as parameters in the electronic Hamiltonian, $H_{BO}(R)$, whose ground-state determines the energy surface $E_0(R)$ appearing in Schrödinger's equation for the nuclei; the force acting on the Ith nucleus will then be

$$F_\alpha = -\frac{\partial E_0(R)}{\partial R_\alpha} = \left\langle \varphi_0(r,R) \left| \frac{\partial H_{BO}(R)}{\partial R_\alpha} \right| \varphi_0(r,R) \right\rangle \tag{2.30}$$

where $\varphi_0(r,R)$ is the electronic ground-state wave function of the Born-Oppenheimer Hamiltonian[2] and $r \equiv \{r_i\}$ the set of all the electronic coordinates. This Hamiltonian depends on R via the electron-nucleus interaction that couples to the electronic degrees of freedom only through the electronic charge density. The Hellman-Feynman theorem states in this case that

[2] We will always assume, during the ab-initio calculations of this work, that our electrons are at T = 0 K, i.e. in their ground-state.

$$F_\alpha = \underbrace{\int n_R(r)\frac{\partial}{\partial R_\alpha}\overbrace{\left(\sum_{i,\alpha}\frac{Z_\alpha e^2}{|r_i - R_\alpha|}\right)}^{V_R(r)}dr}_{e^- - nucleus\ interaction} - \underbrace{\frac{\partial}{\partial R_\alpha}\overbrace{\left(\frac{e^2}{2}\sum_{\alpha\neq\beta}\frac{Z_\alpha Z_\beta}{R_{\alpha\beta}}\right)}^{E_N(R)}}_{completely\ nuclear\ part} \tag{2.31}$$

where $n_R(r)$ is the ground-state electron charge density corresponding to the nuclear configuration R and the completely-nuclear part is just a number which can be calculated exactly for each of those configurations. The Hessian of the Born-Oppenheimer energy surface appearing in equation 2.28 is thus obtained by differentiating the Hellmann-Feynman forces with respect to nuclear coordinates,

$$\frac{\partial^2 E_0(R)}{\partial R_\alpha \partial R_\beta} \equiv -\frac{\partial F_\alpha}{\partial R_\beta} = \int \frac{\partial n_R(r)}{\partial R_\beta}\frac{\partial V_R(r)}{\partial R_\alpha}dr + \int n_R(r)\frac{\partial^2 V_R(r)}{\partial R_\alpha \partial R_\beta}dr + \frac{\partial^2 E_N(R)}{\partial R_\alpha \partial R_\beta}. \tag{2.32}$$

The last equation states that the calculation of the Hessian of the Born-Oppenheimer energy surfaces requires the calculation of the ground-state electron charge density $n_R(r)$ as well as its *linear response* to a distortion of the nuclear geometry, $\partial n_R(r)/\partial R_\alpha$. The Hessian matrix is usually called the *matrix of the inter-atomic force constants* or simply the *dynamical matrix*. An important fact related with these matrices that will be used by our computer program is that, within the adiabatic approximation, the lattice distortion associated with a phonon can be seen simply as a static perturbation acting on the electrons, showing again the connection between the dynamical and electronic properties of the material, and making also easier the phonon calculations. These fundamental results, as already mentioned, were first stated in the late 1960s by De Cicco and Johnson in (1969) and by Pick, Cohen and Martin in (1970) and, within the DFT framework, have been exploited by the so-called Density Functional Perturbation Theory [17].

2.3.3 Density Functional Perturbation Theory (DFPT)

As I just mentioned, the DFPT framework can be used to find the phonon frequencies of the system. It is worth mentioning that there are basically two different approaches to this problem, that don't involve having to reproduce the actual dynamics of the system (which would have to cover some

picoseconds in order to give reliable results) one is the so-called frozen-phonon method [45], in which the main advantage is that it only requires calculation of forces as function of nuclear positions, the disadvantage being that we need to be very careful in the evaluation of numerical derivatives and repeat our DFT calculation for 3N atomic displacements (maybe less if we take also into account the different symmetries in the crystal). The second approach is the so-called response function method, in this method, the force constants are separated in two parts, namely: the electronic and ionic contributions

$$\tilde{C}_{s\alpha,s\prime\alpha\prime}(k) = \tilde{C}^{ele}_{s\alpha,s\prime\alpha\prime}(k) + \tilde{C}^{ion}_{s\alpha,s\prime\alpha\prime}(k), \tag{2.33}$$

the electronic term is expressed in terms of the linear response of the charge density n and the bare ionic potential V_{ion} with respect to atomic distortions:

$$\tilde{C}^{ele}_{s\alpha,s\prime\alpha\prime}(k) = \frac{1}{N_c}\left[\int\left\{\frac{\partial n(r)}{\partial u_{s,\alpha}(k)}\right\} * \frac{\partial V_{ion}(r)}{\partial u_{s,\alpha}(k)}dr + \int n(r)\frac{\partial^2 V_{ion}(r)}{\partial u^*_{s,\alpha}(k)\partial u^*_{s\prime,\alpha\prime}(k)}dr\right] \tag{2.34}$$

The ionic term is given by the second derivative of the Ewald's summation [15]. The advantage of this method is that we have to perform only one DFT calculation, but the calculation of the electronic response is time consuming [17].

2.4 Plane waves and pseudo-potentials

Even with such a big help coming from the simplification due to the Born-Oppenheimer approach (section 2.1.2) and from the power of the Hohenberg-Kohn theorem plus the Kohn Sham ansatz (Sections 2.1.5 and 2.1.6) the many-body problem is still very difficult to solve because, if we want to be precise, we should take into account the field of the bare nuclei and consider the motion of *all* the electrons inside this field. This would involve too many particles and would give place to extremely long computational times, basically because it is very difficult to find a nice type of function which fulfills the conditions of: 1^{st}- making the Kohn-Sham electronic density accurate everywhere and 2^{nd}- making the energy-minimization process easy for standard computer algorithms.

In order to get a further reduction in the computational effort required for the calculation, but still taking into account the physics of the problem, people have introduced periodic boundary conditions therefore imagining the

system as an infinite crystal. This opens the possibility of thinking the electronic density as a superposition of plane waves, where the size of the plane wave basis set to be used for each particular problem can be easily tuned by defining an energy cutoff such that $G^2_{max} \sim E_{cut}$, which then limits automatically the number of plane wave components that we are able to use. Then, the goal of this approach is to perform "fast" calculations by using the minimum possible amount of plane waves for constructing the electronic density together with very efficient algorithms that are available for solving such kind of problems, without compromising the accuracy. This method should work fine, at least for reproducing the density coming from outer (mainly delocalized) electrons, while for inner electrons, the electronic densities would be more accurately modeled if they were worked out through the superposition of atomic wave functions. This, is due to the fact that those electrons are much more localized and, in a plane-wave scheme, they would need a much larger basis set of wave functions to be represented accurately.

It is because of the complexity offered by this all-electron approach that, another well known and very commonly used approximation called the *valence approximation*, is implemented. It relies on considering that all the interesting physical properties of the atoms in a crystal, are mostly due to the valence electrons. Under this approximation we will take the core electrons on each atom as entities which are merged with the nucleus in an ion-like structure. Those *ions* can then be placed as the genuine building blocks of our system, representing the different kinds of atoms in our system. This in practice means that, after being conveniently modeled with a suitable basis set, these ions (or more precisely: their effective influence on the valence electrons) can be represented through an effective potential, and hence the so-called *pseudo-potentials* [46, 47, 48, 49] appear in this context. Among many other technicalities that will not be described here, there is the fact that, when constructing pseudo-potentials, we are free to decide how many electrons will be considered to be part of the core and how many of them will be on the valence region. Although this differentiation is quite standard nowadays, nonetheless the construction of pseudo-potentials still remains an art on its own due to many other factors.

For this work, I performed tests on pseudo-potentials that were either, available already on the Internet (at *www.pwscf.org*) or prepared by collaborators of our group. They corresponded to the two main kinds: Norm-Conserving (NC) and Ultra-Soft (US), and were prepared by using the PBE [50] formulation for the exchange-correlation part. A test of the pseudo-potentials can be done in many ways; here for example, all pseudo-potentials were studied

against the bulk properties of the materials that each one of them represented, one of such tests is described in detail in Appendix B. After checking the correctness of bulk ground-state structural properties, for example the lattice spacing, we proceeded to calculate also their band structures, in order to check if some unphysical features of the electronic energy levels (ghost states) were present [51].

2.5 The Quantum-Espresso package

To summarize this chapter, we have seen here that ab-initio methods based on Density-Functional Theory (DFT) are by now common and well established tools for studying structural and vibrational properties of materials on very realistic grounds. The plane-wave pseudo-potential method and the Local-Density Approximation (LDA) to DFT have provided a simple framework whose accuracy and predictive power have been convincingly demonstrated in a large variety of systems [52]. The calculation of reliable phonon spectra and other dynamical properties in real materials is well within the reach of DFT.

I proceed now with the description of the computer package used during this work. Quantum Espresso [53], is a modular tool which by the use of each module or subprogram, and also by means of different input modalities, takes the responsibility for individual parts of the full characterization of the system. It is in this way that, for example, the module *pw.x* is the subprogram responsible for getting the electronic ground-state energy for a given set of atoms, by finding iteratively the best possible ground-state electronic density $n_0(r)$ through the superposition of a limited basis set composed of a finite amount of plane waves. Then many other things can be done, even in a non-self-consistent way, for example: using the ground-state set of wave functions found after the minimization with *pw.x*, it is also possible (with the same subprogram) to calculate non self-consistently, the electronic energies for an arbitrary set of k-points inside the Brillouin zone of the system and then construct its band diagram. One can also use other subprograms, such as *ph.x*, which takes advantage of the previously optimized set of plane waves and uses it to calculate the phonon frequencies at any given set of k-points by using DFPT, and non self-consistent calculations allow for the construction of the phonon dispersion curves of the system along any direction in the reciprocal space.

Another very interesting thing that we can do is to optimize the system's

geometry. This is attained by using the so-called relaxation mode (available with the module *pw.x*) in which one gives arbitrary initial positions for the atoms as an input, and then the program tries to evolve the ionic positions, following the direction that minimizes the inter-atomic forces up to the point in which all the forces acting over each atom are very close to zero. This, as we will see, was particularly useful in Chapter 3 of this work, where there was an uncertainty about the position occupied by nitrogen inside the sub-lattices formed by platinum atoms in one case and osmium atoms in the other. It is worth noticing that the zero-force ionic configuration obtained in this way, is surely a local minima of the total energy of the system but, so far, no method exist that can guarantee the obtaining of the global minima for an arbitrary set of atoms [54], so, additional physical quantities apart from the ground-state energy, are needed to cross-check with experiments. Some recent work supervised by myself, that is not reported in this thesis, has been carried out by our group in an attempt to devise a reliable structure-predictor method for small systems, so far it has been only used for the case of mono-atomic oxygen [55], and many improvements are planed for the short term.

The *pw.x* program, in general, will not perform the self-consistent energy minimization over the entire set of k-points present in the Brillouin zone, instead, we are supposed to provide a mesh of k-points that we assume as "converged" this means, that if we were to increase the number of k-points to be considered along any reciprocal-space direction, the lowering of the ground-state energy due to this, wouldn't be noticeable. In the following chapters, such grid of k-points is reported for each one of our computer experiments. After setting these numbers, any standard code nowadays should be able to use the symmetries available on the system to sample an smaller zone (possibly by following the H. J. Monkhorst and J. D. Pack method [56]) so that the computational effort can be reduced as much as possible, without affecting the sampling of the reciprocal space. Among the most important parameters in the input files of Quantum Espresso, we have:

ibrav is the kind of Bravais lattice we are simulating, *ibrav=1* is for *sc*, *ibrav=2* is for *fcc*, etc.

celldm(i) i=1,2,3, are the lattice parameters of the crystal and are usually given in units of Bohr-radius, while i=4,5,6, are the cosines of the angles between each pair of lattice vectors.

ecutwfc is the energy cutoff, which limits the amount of plane waves that the program will use during the minimization procedure.

nat means *number of atoms* i.e. how many atoms we will have per unit cell. As an example, in the PtN case we used *nat = 2*, while for for PtN_2 pyrite we used *nat = 12*.

ntyp means *number of atomic species* i.e. how many different kinds of atoms are involved, for example *ntyp = 2*.

ATOMIC_SPECIES is the section where we have to put the symbol of the atoms, their corresponding masses (as written on the periodic table) and the name of the files containing the pseudo-potentials.

ATOMIC_POSITIONS is the section in which we are supposed to give the spatial distribution of the atoms. In this field, during a relaxation process, it can also be specified which atoms we want to keep fixed and which are free to move.

k_points is the number of points in the reciprocal space that the program is supposed to sample, i.e. the points in which the actual self consistent minimization of the energy will be performed.

Finally, for the molecular dynamics simulations, the program *fpmd.x* in its version 2.1.4 (named *cp.x* in later versions) has been used. The above input descriptions are also valid for the *fpmd.x*/*cp.x* modules, apart from the fact that here, only the Gamma point $\boldsymbol{k}$=(0,0,0) is used for the electronic energy minimization.

PART II

Chapter 3

Nitrides

Before the year 2004, no late transition-metal nitrides with high nitrogen content were known. There has been considerable interest in the synthesis of new nitrides because of their technological and fundamental importance [57, 58]. Owing to it having one of the strongest covalent bonds, nitrogen is very stable and inert under normal conditions. Yet nitrogen reacts with selected elements, forming compounds with a variety of intriguing properties. Some of the nitrides (mostly of group III and IV elements) produced by various methods are widely used as optoelectronic materials; for example, light-emitting diodes and semiconducting lasers.

Theoretical studies of nitrides are also numerous, covering the topics of optoelectronics [59, 60], physical and structural properties [59, 61, 62] and superconductivity [63], the latter adds to the fact that another important group of these materials are the transition-metal nitrides mostly known for their superconducting properties [64, 65, 66, 67, 68], most of the early transition metals form nitrides at high temperatures and at either ambient or high pressures (for example, ZrN, VN, MoN).

Although numerous metals react with nitrogen, there were no binary nitrides known of the noble metals. Platinum on the other hand, forms simple binary compounds with halogens (for example, PtF_4, PtI_2); oxides and chalcogenides (for example, PtO, PtS) but it was not known to form crystalline nitrides [69], in fact, previous to the work by Gregoryanz *et al.* [10], only reactions forming small molecules containing Pt and N in the gas phase were reported (diatomic PtN by sputtering [70] and PtN, PtN_2 and $(PtN)_2$ by laser ablation [71]).

Once the synthesis of bulk PtN_2 was reported [10], the possibility of finding more of these materials generated significant interest since it was sug-

gested that they could indeed constitute a new family of superhard materials [4]. Superhard materials are of huge technological relevance in applications ranging from cutting tools down to abrasives for all kinds of industrial applications. The presence of these materials in industry was, until not too long ago, limited only to the use of diamond powders of different qualities depending on the particular application. While diamond exhibits extreme hardness, its performance as a super-abrasive is limited by the fact that it is neither stable in the presence of oxygen at temperatures of relevance for industrial applications, nor a suitable abrasive for machining ferrous alloys. Natural and artificial diamond are too expensive or difficult to synthesize in the quantities required by a growing industry, hence many research efforts have been directed towards obtaining alternative superhard materials with characteristics better than those of diamond or c-BN (a very good super-abrasive with half the hardness of diamond) and that can be synthesized at milder P-T conditions with reproducible sizes, in order to make them suitable for high-speed cutting and polishing of ferrous alloys. In this context synthesis of PtN_2 marked a promising first step towards a new family of such materials since its bulk modulus, a quantity that in general seems to correlate well with strength and hardness, was reported to be higher than that of its parent metal (fcc-Pt).

OsN_2, on the other hand, doesn't have a bulk modulus larger than that of its parent metal Os [11]. However, it is also interesting for other reasons; for example, this nitride is the only one in the new family that exhibits a metallic character, making it difficult to characterize by vibrational spectroscopy. Here, I show that even which such difficulties it is possible to find its crystalline structure and conclude that this material, in the same way as PtN_2, is formed by N_2 units embedded in the parent metal sub-lattice. Such a metallic structure opens the possibility of the presence of high-frequency vibrational modes coming from the N_2 units, that can couple to the electrons at the Fermi level and hence, to obtaining a phonon mediated (BCS) superconductor with a high T_c. This T_c, as we will see, is not that large in the case of OsN_2, but still, the superconductivity is present and can lead to new discoveries in future members of this family.

3.1 PtN_2

3.1.1 Introduction

After the synthesis of this material, the x-ray diffraction data unambiguously showed that Pt atoms form a fcc sub-lattice so, in Ref. [10], the authors suggested zinc-blende (space group $F\overline{4}3m$) structure for the new compound, with Pt:N as 1:1. However, the conclusions of Ref. [10] were ambiguous because x-ray diffraction is unable to determine the positions of the nitrogen atoms due to the large Pt/N atomic mass ratio and also because the electron micro-probe technique used for measuring Pt:N enclosed many sources of error.

Subsequent theoretical studies offered a panoply of diverging opinions on the mechanical stability and bulk properties of various phases of platinum nitride, including strong confirmation of the suggested zinc-blende structure [72, 73], as well as the finding that this structure was not mechanically stable [74]. These studies proposed additional candidate structures for a platinum nitride compound, with Ref. [75] suggesting rocksalt PtN (rock salt was also suggested as an alternative in the original experimental paper), while Yu *et al.* [74, 76] showed PtN_2, with fluorite structure, to be mechanically stable and have a bulk modulus comparable or slightly higher than that of the pure platinum [74], which would then agree with experimental observations in this regard. In addition, later experimental results using x-ray photo-emission spectroscopy provided evidence for an even larger nitrogen content, perhaps as high as 1:2(Pt:N) [77]. Unfortunately, none of the proposed structures so far mentioned, was able to explain the multiple Raman active modes observed experimentally in Ref. [10].

In this section, I show that the compound synthesized in Ref. [10] is PtN_2 with the pyrite structure, since, according to our first-principles calculations, PtN_2 having this structure is fully consistent with x-ray, Raman and compressibility measurements reported on Ref. [10].

3.1.2 Methodology

Calculations [53] were performed within the density functional theory using a Perdew-Burke-Ernzerhoff exchange-correlation functional [50] and a plane wave basis set for the electronic wave functions with a kinetic energy cut-off of 60 Ry (80 Ry for converging the phonon calculations). An ultra-soft pseudo-potential description of the ion-electron interaction [78] was used,

with platinum's $4s$ and $4p$ semi-core states explicitly included in the valence. Brillouin zone integration was found to be converged with a uniform grid of $7\times7\times7$ points. Structural relaxations were limited to the nitrogen positions, with platinum atoms fixed on the fcc lattice at the experimental zero-pressure lattice spacing (4.8041 Å). A check of the pseudo-potentials used in this part, is shown and described in detail in Appendix B.

3.1.3 Results and discussion

Following the suggestion that was given by Gregoryanz *et al.* after analyzing the experimental evidences coming from the electron micro-probe measurements, regarding the 1:1(Pt:N) stoichiometry, we decided to simulate first the platinum mono-nitride compound.

Zinc-blende

The first thing we did, following the hints provided by Ref. [10], was to simulate a zinc-blende configuration (see Fig. 3.1) since this one not only agreed well with the stoichiometry predicted by the electron micro probe, but also with the space group obtained after the Rietveld refinement and the presence of some Raman spectra, which was not the case for the rocksalt structure.

From Table 3.1 we can see the values obtained through *Quantum Espresso* for some key quantities which can be compared with the experimental ones mentioned in section 4.1. The numerical disagreement specially for quantities such as the bulk modulus and the phonon frequencies at Γ, is manifest. Even worse, no more than one phonon frequency appeared in the simulation, while from the experimental data we knew that there were at least three Raman-active peaks. Also the comparison between the ground-state energy here and the one obtained at the end of *Appendix B* for $Pt + \frac{1}{2}N$ give us as result that this structure is 1.4 eV (0.103 Ry) higher in energy than platinum and nitrogen separately. Then it is clear that, at least from the point of view of our DFT simulation, the zinc-blende structure doesn't fulfill many of the requirements needed to be in agreement with the experimental results obtained.

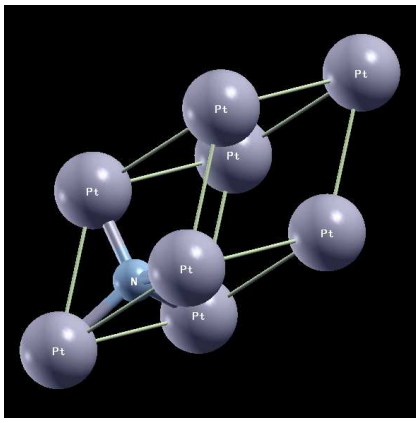

Figure 3.1: Zinc-blende structure for PtN.

Quantity	Calculated	Difference
Lattice parameter	4.69 Å	-0.11 Å
Bulk modulus K_0	251.4 GPa	-120.6 GPa
$K_0\prime$	2.12	-1.88
$HF phonon$ at Γ (cm^{-1})	528	-217
Energy	-72.421 Ry	0.103 Ry

Table 3.1: Ab-initio results for zinc-blende PtN. HF stands for high frequency.

Rocksalt

Due to the drawbacks presented by the zinc-blende structure it was decided to give a chance to the rocksalt configuration (showed in Fig. 3.2) expecting that maybe it could explain some of the observed experimental features better than the previous calculations with zinc-blende. The fact was that, as can be seen from the Table 3.2, only the bulk modulus improved with respect to the one calculated for the zinc-blende configuration. But from the bigger disagreement in the other aspects we can say that we didn't have yet the correct atomic configuration.

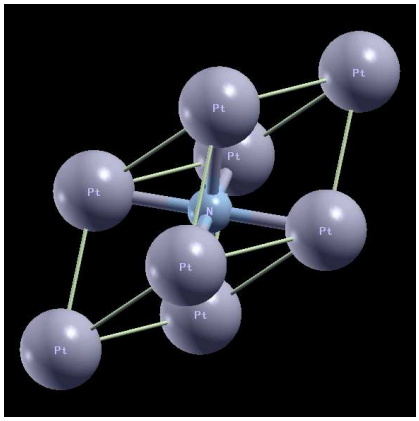

Figure 3.2: Rocksalt structure for PtN.

Quantity	Calculated	Difference
Lattice parameter	4.41 Å	-0.39 Å
Bulk modulus K_0	347 GPa	-25 GPa
$K_0\prime$	1.00	-3.00
Phonons at Γ (cm^{-1})	259	-486
Energy	-72.382 Ry	0.142Ry

Table 3.2: Ab-initio results for rocksalt PtN.

In order to find some other equilibrium atomic position but still conserving

the stoichiometry suggested by the experimental data, we proceeded by relaxing the structure departing from many different initial positions for the nitrogen in the unit cell, while letting fixed platinum in its *fcc* structure. The results were again consistent with the zinc-blende and rocksalt structures, i.e. by relaxation we couldn't obtain a different structure as result and hence, the results shown up to this point couldn't be improved due to the lack of new symmetric and stable configurations different to the two already studied. A comparison of the volume vs. pressure behavior for Pt, experimental PtN, and PtN in zinc-blende and rocksalt configurations, from their equations of state, is shown in the Fig. 3.3.

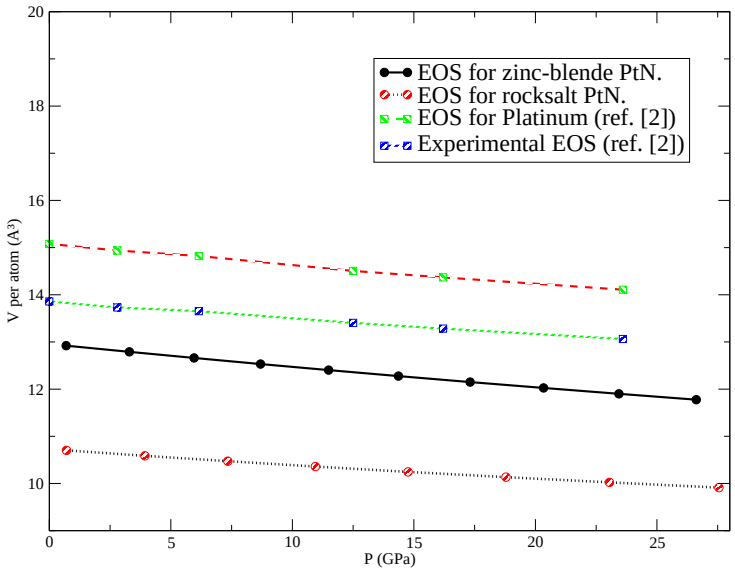

Figure 3.3: Volume Vs. Pressure for PtN.

PtN_2 stoichiometry

Then, our conclusion was that something could be wrong with the platinum mono-nitride assumption and other possibilities should be checked. Could the platinum di-nitride be the solution? Well, some important questions were: Would this PtN_2 be a suitable option energetically speaking? Was the lattice parameter going to be increased considerably making it incompatible with the results from X-ray diffraction? Would the bulk modulus and the phonon frequencies going to be improved by this change with respect to the mono-nitrides?.

In order to clarify this, the first thing we needed to do was to relax the system again from different random starting points but this time with two nitrogen atoms per unit cell, still keeping the platinum atoms fixed in their *fcc* positions. After these experiments, many configurations came out (shown in Figs. 3.4 - 3.7[7]) and then we proceeded to compare their energies (see Fig. 3.8) in order to select the best candidate and calculate for this, the interesting quantities we needed to compare.

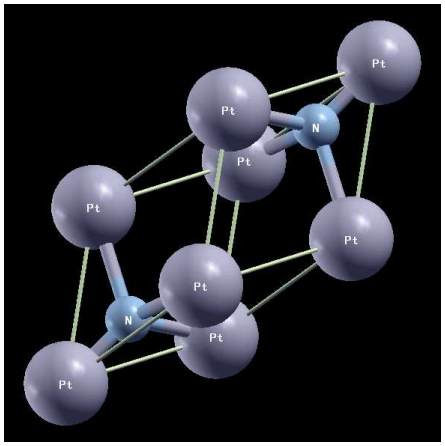

Figure 3.4: N in the zinc-blende and the "*anti-zinc-blende*" positions. This also coincides with the structure of Fluorite.

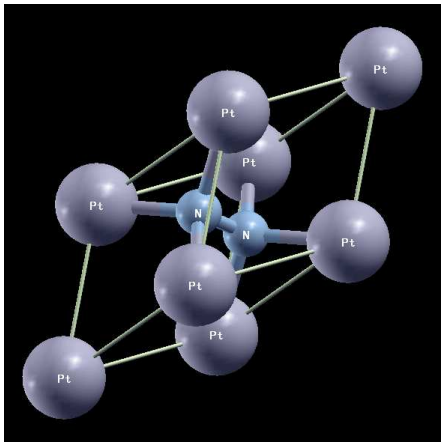

Figure 3.5: "N_2", in the rock-salt position.

As can be seen from the energy comparison in Fig. 3.8 the best configuration turned out to be the one corresponding to the Fig. 3.5 (solid line with rhombus) or equivalently the Fig. 3.9 (dashed line with circles). This one corresponds to a primitive *fcc* platinum sub-lattice with a nitrogen molecule in its center, i.e. with its center of mass occupying the rocksalt position. For this configuration we did the same calculations as before, finding this time a much better agreement with the experiments, even if still the numbers still don't coincide in a 100% with measurements. One remarkable fact is that the stiffness of the nitrogen molecule (now embedded in the platinum crystal) helped to increase the phonon frequencies if we compare them with the values reached previously with only one nitrogen per unit cell. Moreover, in the phonon spectra, at least three —some of them degenerate— phonon peaks

[7]Some others were symmetrically equivalent to the ones which are shown in these graphics.

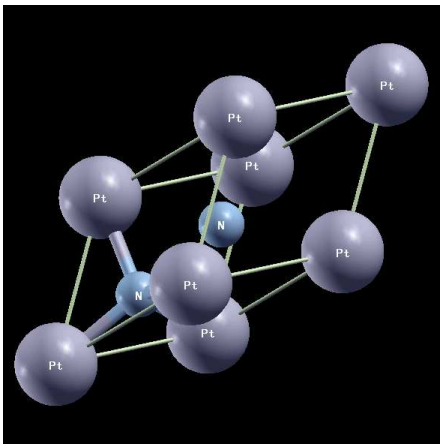

Figure 3.6: One N in the rock-salt and other in the zinc-blende position.

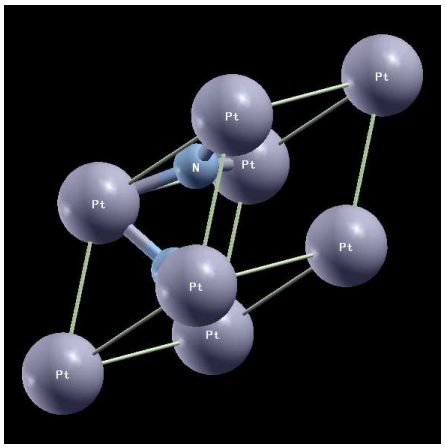

Figure 3.7: Not a very symmetric position, but also offered local equilibrium.

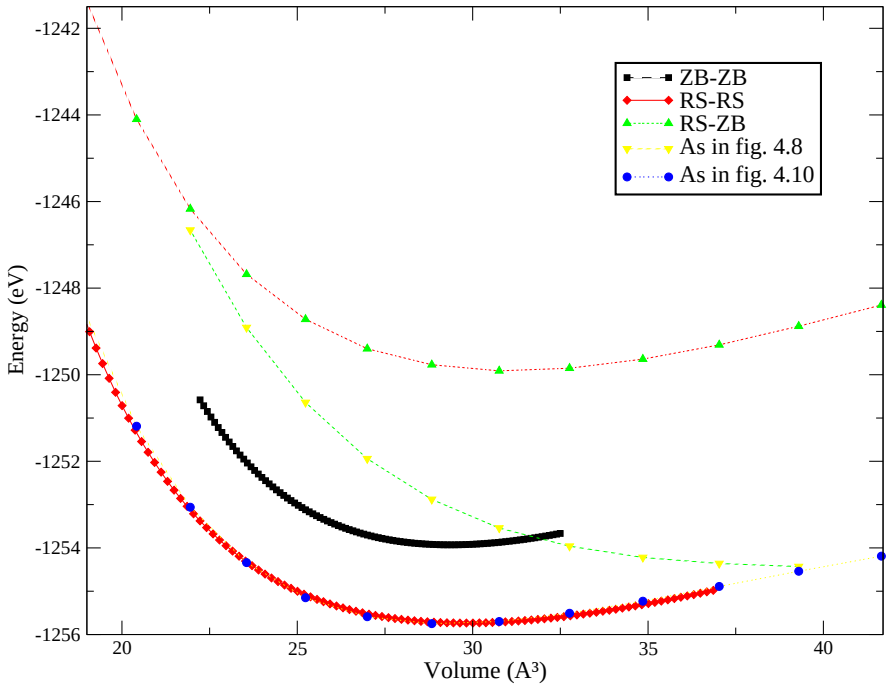

Figure 3.8: Energy comparison for the different configurations showed.

appeared in the region were the experimental spectra was taken[8], which is also in agreement with the observations.

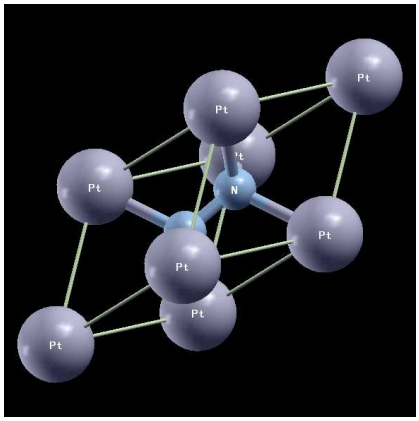

Figure 3.9: Same as in Fig. 3.5, with a different orientation.

Quantity	Calculated	Difference
Lattice parameter	4.88Å	0.08Å
Bulk modulus K_0	324.6 GPa	-47.4 GPa
$K_0\prime$	1.00	-3.00
Phonons at Γ (cm^{-1})	620	-125
Energy	–92.286 Ry	0.082 Ry

Table 3.3: Ab-initio results for "rock-salt" PtN_2.

In synthesis, this preliminary search [79] on the minimal unit cell containing one PtN_2 formula unit (i.e. with the rhombohedral primitive unit cell of the fcc lattice) showed that, a structure with an interstitial N_2 centered in the octahedral cavity of the Pt fcc lattice, gives an energy which is lower than that of the structures proposed by Ref. [10] all of which were based on atomic nitrogen with Pt:N as 1:1, and nitrogen centered either on the octahedral cavities (rock salt) or on the tetrahedral cavities (zinc blende). A single interstitial N_2, in the way it has been proposed so far, however, violates the cubic symmetry of the platinum sub-lattice and would lead to a sizable rhombohedral distortion, which is not observed experimentally. In this work, a deeper energy minimum is obtained by expanding our analysis to the cubic conventional cell of the fcc metal lattice. Arranging the nitrogen atoms on the eight fold sites of space group $P\overline{a}3$ (see Fig. 3.10(a)) minimizes the quadrupole interaction between the dinitrogen molecules, thus further reducing the energy, while preserving the observed cubic symmetry of the metal sub-lattice.

The resulting pyrite isostructure agrees with all experimental data; first of all, a Rietveld refinement of the observed diffraction pattern using $P\overline{a}3$ (Fig. 3.10(b)) is indistinguishable with experimental data as compared to

[8]There is an impossibility in these high pressure techniques to take phonon-spectra above 1300 cm^{-1} because of an interference coming from the diamond's phonon line

the originally proposed zinc-blende structure. In this structure at ambient pressure, platinum atoms are accommodated on the Wyckoff site 4a and nitrogen atoms are on the site 8c with x=0.415.

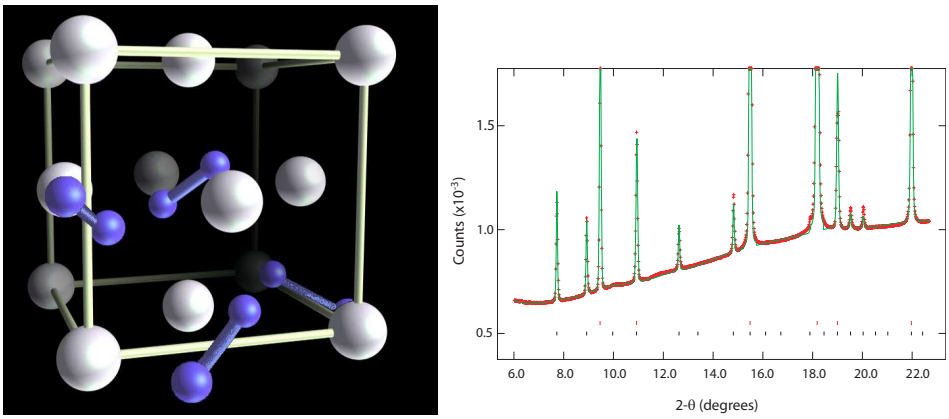

Figure 3.10: Left: Pyrite Structure of PtN_2, space group $Pa\bar{3}$. Platinum atoms (white) form a face-centered cubic lattice, dinitrogen (N_2) units (blue) occupy the octahedral cavities of the Pt lattice. The calculated N-N distance at ambient pressure is 1.42 Å. Right: Rietveld fit using the $Pa\bar{3}$ space-group. Red crosses: data at ambient pressure (λ=0.3738 Å); green line: Rietveld fit; black ticks: PtN_2 peaks; red ticks: Pt peaks. The most intense Pt peaks are cut-off.

PtN_2 pyrite is also found to have a considerably lower ground-state energy than that of any other proposed structures, rendering the existence of any of these phases of PtN or PtN_2, highly unlikely. Moreover, in contrast to the structures proposed previously, the pyrite phase shows not only mechanical stability, but good agreement with both bulk properties and experimentally observed Raman spectra. Our calculations (Table 3.4) show the pyrite structure to be 2 eV per stoichiometric unit lower in energy than the fluorite structure at ambient pressure. The comparison with 1:1 structures (zinc-blende and rocksalt) is based on their respective formation energies, and shows that pyrite has energy 0.3 eV (per Pt atom) lower than that of zinc-blende and 0.8 eV lower than that of rocksalt. The positive sign of the formation energies in our calculations reveal, however, that PtN_2 is unstable towards dissociation into its constituent elements, at least at zero pressure. This is corroborated by experimental evidence that, below 10 GPa, PtN_2 dissociates upon mild heating.

Moreover, as we will see in the next chapter, for this nitride the observed conditions of synthesis are well inside the region of thermodynamic stability

of the compound 3.19, which could be explained by a large kinetic barrier. In fact, the exact transition pressure is calculated to be around 17 GPa and then, it is not strange that PtN_2 can be quenched even to ambient conditions.

The PtN_2 pyrite structure is characterized by Pt in six-fold coordination with N, with a calculated Pt-N distance of 2.096 Å at zero pressure. Each nitrogen is four-fold coordinated to three Pt atoms and one N atom. The interstitial dinitrogen unit has a zero-pressure N-N bond length of 1.42 Å , much longer than the molecular triple bond, and consistent instead with a N-N single bond. The calculated energy versus unit-cell volume was fitted with the Birch-Murnaghan equation of state, giving an equilibrium lattice parameter that agrees with experiment to within 1% (Table 3.4). The bulk modulus (B) is shown to be considerably higher than that of both bulk platinum and fluorite PtN_2, again in good agreement with experimental results. The slight and systematic overestimation of the lattice parameters as well as the systematic underestimation of the calculated bulk moduli with respect to the experimental results, both for PtN_2 and for Pt, are a likely consequence of the choice of the PBE density functional.

	a	B, B'	B, B'	ΔE (eV)
Exp. [10]	**4.804**	373, **4.00**	354, 5.23	-
Pyr.(cal.)	4.848	305, **4.00**	285, 5.50	1.12
Fl.(cal.)	4.939	269, **4.00**	260, 4.73	3.15
ZB(cal.)	4.760	213, **4.00**	217, 3.62	1.40
RS(cal.)	4.471	251, **4.00**	242, 4.78	1.93
Pt exp. [80]	3.924	275, 4.78	277, 5.23	-
Pt cal.	3.966	242, 5.83	249, **5.23**	-

Table 3.4: Bulk modulus (in GPa), its pressure derivative (B'), and equilibrium lattice parameters (in Å), obtained from fitting calculated energies over a range of volumes with a second order Birch-Murnaghan equation of state. Bold values were fixed during the fitting to compare with experiments. Formation energies ΔE are relative to $Pt+N_2$ for PtN_2 compounds,$Pt+\frac{1}{2}N_2$ for PtN compounds.

In order to check the local mechanical stability of the pyrite structure we computed its elastic constants. For crystals with cubic symmetry, application of a single strain to the lattice vectors is sufficient to determine all three independent elastic constants [81]. These calculations –in addition to confirming the values of B calculated from the equations of state– also show

pyrite structure PtN_2 to be mechanically stable and to have a relatively high shear-modulus (Table 3.5), an important indicator for hardness in dielectrics [82]. The high G/B ratio (G being the shear modulus) or, equivalently, the low Poisson's ratio (ν) points to a high degree of covalency [4], suggesting that intercalation of the dinitrogen units into the Pt lattice induces a substantial change of the electronic structure from metallic, in bulk Pt, to covalent in PtN_2. Our elasticity calculations for zinc-blende PtN (Table 3.5) suggest that it is mechanically unstable, as claimed in [74], but our difference between c_{11} and c_{12} for that particular configuration is too small to allow us to make conclusive statements about stability within the approximations used. However, our calculations show conclusively that zinc-blende as well as rocksalt and fluorite structures are in poor agreement with the full set of bulk properties reported in Ref. [10] (Table 3.4).

	c_{11}	c_{12}	c_{44}	B	G	E	ν
Pyrite	696	83	136	288	221	528	.19
Fluorite	473	160	115	264	136	348	.28
Zinc-Blende	197	200	22	199	10	30	.48
Rock-Salt	266	221	36	236	30	86	.44

Table 3.5: Elastic constants and elastic moduli in GPa for a variety of proposed PtN and PtN_2 phases, calculated in the limit of infinitesimal strain ($E$is the Young's modulus, other quantities are defined in the text). Mechanical stability for cubic crystals is expressed in the following conditions on the elastic constants [83]: $c_{44} > 0$,$c_{11} > |c_{12}|$, and $B = \frac{c_{11}+2c_{12}}{3} > 0$.

The calculated zone-center vibrational modes of PtN_2 pyrite, as determined using density-functional perturbation theory [17], show good agreement with experimentally observed Raman spectra. Calculated and experimental Raman frequencies over a range of pressures are compared in Figure 3.11(a). Calculations show the existence of two almost degenerate modes giving rise to a Raman peak around 700 cm^{-1} (Fig. 3.11(a)) which was reported but not shown in [10] and originally attributed to a non-stoichiometry of the samples. The calculated Raman intensities [84] (Fig. 3.11(b)) show the presence of two intense peaks, in good agreement with the experimental results, and of three weak modes, two of which are seen in the experimental spectra. It is interesting to note that all Raman active phonon modes of PtN_2 pyrite, although calculated using the full cell, arise only from the displacements of the nitrogen atoms, and do not have Pt components. In fact their frequencies are in fair agreement with those predicted [85] and later observed [86] for single-bonded nitrogen in its polymeric phase.

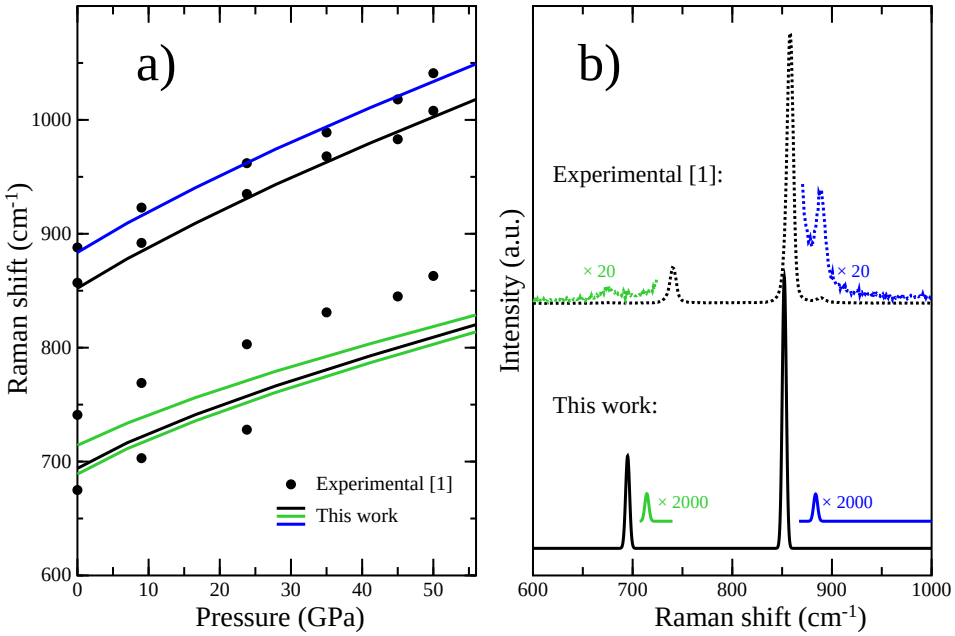

Figure 3.11: (a) Calculated and experimental (from Ref. 1) Raman frequencies as a function of pressure. An agreement within 5% in the frequency determination is typical for this kind of calculations. (b) Calculated and experimental Raman intensities. An additional calculated peak with intensity similar to the green peak at 710cm^{-1} is not shown as its frequency overlaps with the intense mode at 695 cm^{-1}.

Finally, the calculated electronic band structure of pyrite PtN_2 at zero pressure, reported in Figure 3.12, shows a clear insulating character. Band gaps are typically underestimated within density functional theory, so the calculated indirect band gap of about 1.5 eV could correspond to a true gap of 2-3 eV, which would make PtN_2 an interesting candidate for optical applications [57].The insulating character is consistent with the covalent nature of bonding revealed by the low Poisson's ratio discussed before in this section.

All the evidences presented so far strongly indicate that the compound under study has a $Pa\bar{3}$ structure with interstitial single-bonded N_2 units, hence making it desirable to find an explanation for how such structure can in effect be responsible for the hardness and insulating properties of this compound. Insertion of atomic nitrogen into transition metals is known to lead to an increase in directional bonding and therefore to an increase of mechanical strength.

Grossman *et al.* [87] have shown that such changes are more dramatic for

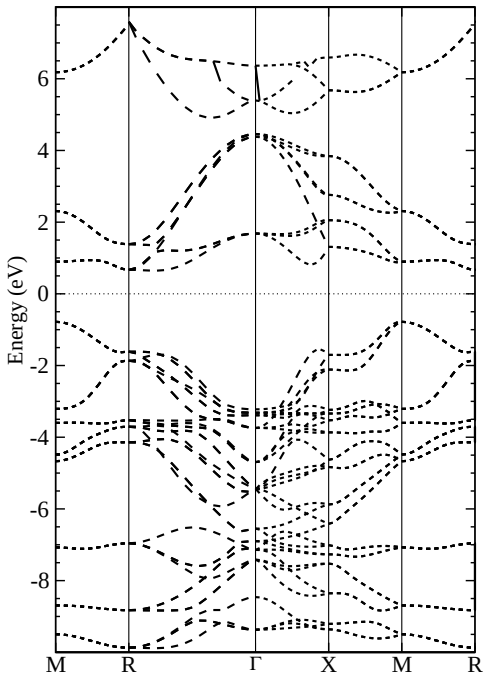

Figure 3.12: Electronic bands of Pyrite PtN_2 at ambient pressure along high symmetry directions. Filled states have negative energies.

early transition metals, due to the fact that the very-flat density distribution of the elemental phase is heavily altered by the insertion of interstitial nitrogen atoms. Late (heavier) transition metals have a more corrugated density distributions in their elemental metallic phases and, therefore, should not increase their hardness noticeably in these (1:1) nitride phases, this was shown in [87] for the rock salt phases. A histogram of the density distribution for pyrite PtN_2 (Fig. 3.13(left)) shows however, that insertion of dinitrogen in Pt causes a four-fold reduction of the histogram peak, which is qualitatively comparable to the reduction observed in Ref. [87] for light transition metals with single nitrogen and hence, compatible with an effective increase of its hardness. The use of the histogram is compulsory in this case since we cannot detect directly the appearance of a clear directionality coming from the Pt-N covalent-bonds. This is so, due to the fact that the electronic density belonging to the *d*-orbitals of Pt still remains quite delocalized in PtN_2, making it very difficult to define where these bonds lye by simple inspection of the charge-density (Electron-Localization-Function calculations were beyond the scope of this work) hence, it would be more precise to describe the appearance of covalency in this material as: "a clear reduction of the homogeneity on the interstitial charge-density distribution in the Pt sub-lattice with respect

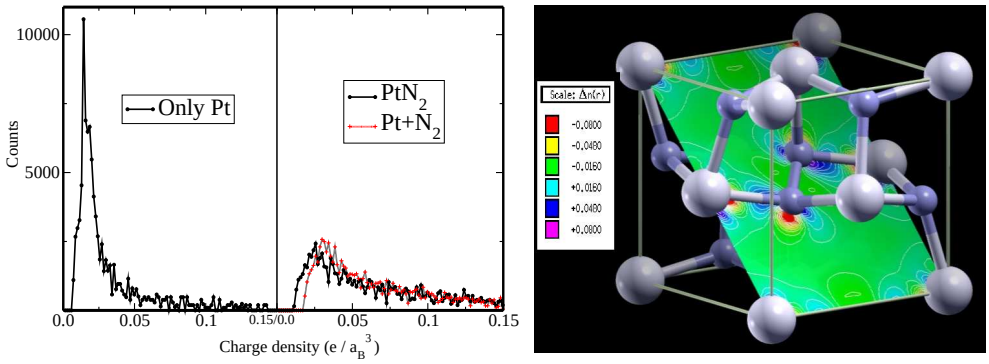

Figure 3.13: Left: Histogram of charge densities for bulk Pt (left), for PtN_2 (right, black), and for Pt+N_2 (right, red). Right: Cut of the charge density difference (compound − individual atoms) showing charge displacement.

to the one present in the pure metal". This observation indicates that, when it comes to late TMs, directional bonding due to dinitrogen interstitials is clearly stronger than the one that would be obtained by just inserting atomic nitrogen, which again is in agreement with the lack of similarities between the 1:1 (Pt:N) phases proposed for this compound and experiments.

Moreover, a comparison of the density histogram of PtN_2 with the one obtained by summing the individual densities of Pt and N_2; shows that, in the compound, the electronic charge-density access a minimum value that is lower than the one obtained from the sum. To do this, we simulated first a system of Pt without N_2 units and then one of N_2 without Pt atoms, maintaining the atoms always fixed in the positions that they occupy in PtN_2 at ambient pressure. The above observation is also clear from Figure 3.13(right), where a two-dimensional cut of such charge difference is shown. As a conclusion, we can say that, besides a noticeable re-hybridization of the Pt semi-core orbitals, charge-density difference and the histogram shown on Figure 3.13 demonstrate that, in the PtN_2 compound, charge flows from interstitial low-density regions to bonding regions of higher density, and this is again consistent with covalency. In this way, the presence of interstitial dinitrogen units is also crucial to explain the insulating character of pyrite PtN_2 since, all platinum-nitride structures proposed before this work, contain interstitial nitrogen in the atomic form and have been reported to be metallic.

3.1.4 Beyond PtN_2-pyrite

After having solved the structure of PtN_2, recently we started wondering which structures could be other high-pressure phases for this compound. PtN_2-Pyrite is made out of octahedral units (centered on the six-fold coordinated Pt atoms) and this type of local coordination is common to many other compounds at high pressure, the most well-known case being silica (SiO_2). Moreover, many of those compounds, having the same 1:2 stoichiometry, share with PtN_2 the property of counting pyrite as one of their high-pressure phases. It seems also that pyrite, in certain cases (e.g. silica, GeO_2, $NiAs_2$, $FeSe_2$, $CoTe_2$, NiP_2, etc.) offers among all structures made out of octahedral units, the best possible packing for the atoms [89, 90]. Hence, pyrite is commonly found in phase diagrams as one of the last stable octahedral phases for increasing pressure, remaining so up to very high pressures (predicted and recently observed above 205 GPa for silica and observed at 80 GPa for Germania).

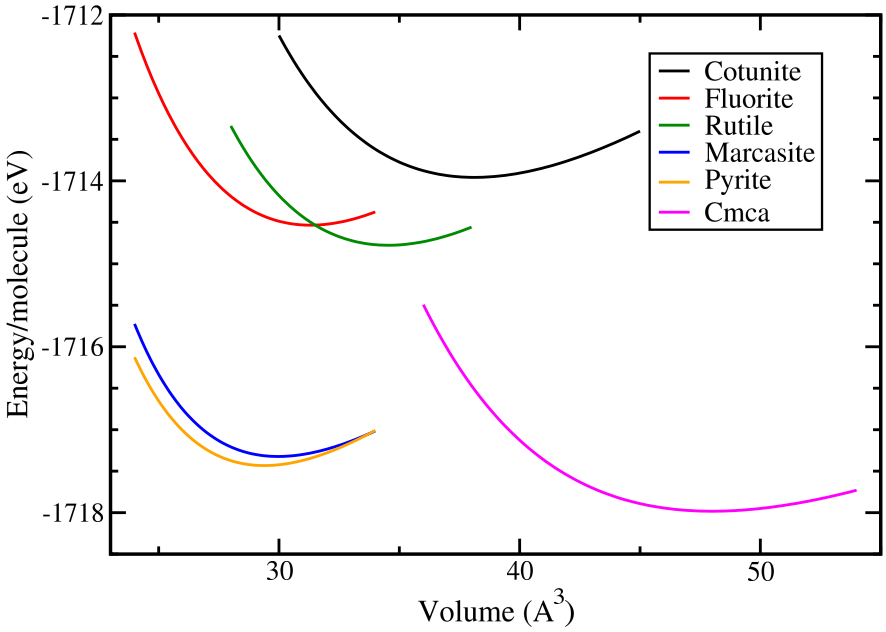

Figure 3.14: Equations of state for the different PtN_2 structure studied in this section.

In this work, that has been carried out in collaboration with Bachir Bouhafs thanks to a cooperation with the ICTP, we tested most of the commonly encountered octahedral configurations, and discovered from their EOS (some

EOS are shown in Fig. 3.14), that pyrite remains by far the most stable structure also for PtN_2, and compares closely to marcasite (Fig. 3.17) and to a high-symmetry version of columbite (Fig. 3.15) in regards to its total energy. Marcasite under no conditions becomes more favorable than pyrite and there is no thermodynamic transition point between these two structures neither above nor below the pressure conditions reported in experiments. A *Cmca* structure relaxed from columbite, instead, appears more stable at pressures lower than the pressure of formation for PtN_2-pyrite. At those low pressures, the system has been reported to dissociate easily towards its constituents. Even if this work is still in a very preliminary stage, we argue however that, when departing from pyrite, dissociation shouldn't be easier to reach than the *Cmca* phase for, in order to arrive at *Cmca*, only a small tilt of the dinitrogen units is needed, which points to a lower kinetic barrier for the transformation when compared against a complete dissociation. Finally, coming back to our comparison with silica and GeO_2, it is interesting to observe that, also for those materials, the transition from columbite (or α-PbO_2) to pyrite, has been observed. The latest results, show that some other new structures may, as in the case of *Cmca*, have energies lower than that of pyrite at larger volumes, which opens new possibilities for low pressure structures of PtN_2 that can be recovered by quenching pyrite.

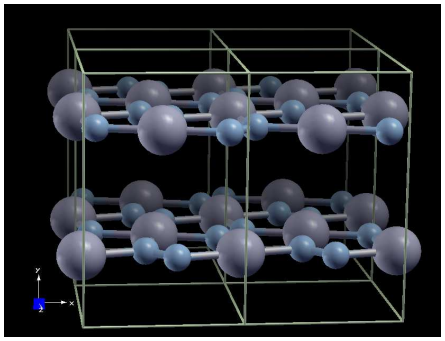

Figure 3.15: Layered view of the relaxed *Cmca*-PtN_2 structure.

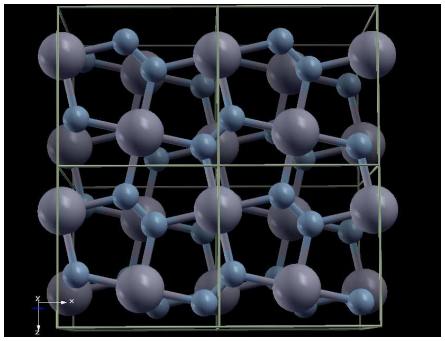

Figure 3.16: View of the a-b *Cmca* planes.

3.1.5 Conclusions

I proceed now to summarize this section; in Ref. [10] platinum nitride was observed as a result of the reaction of a molecular nitrogen fluid with Pt metal at high pressure and temperature (P $\sim$ 45 GPa and T $\sim$ 2000 K).

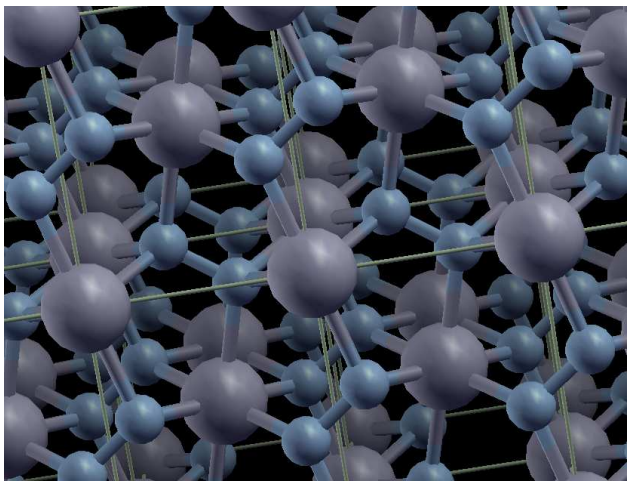

Figure 3.17: PtN_2 in the marcasite structure.

Here, the structure of this compound (PtN_2 pyrite) was resolved by using first-principles calculations, excellent agreement with all experimental data available was obtained and it was shown that PtN_2, having a pyrite structure, consists of interstitial single-bonded N_2 units incorporated in the octahedral cavities of an fcc Pt sub-lattice, which profoundly determine the observed insulating-covalent behavior of this material. This incorporation also implies a change of bonding for N_2 from triple to single, a transition that molecular nitrogen is known to undergo during amorphization at similar pressures [88]. We therefore argue that pressure-induced changes in the bonding character of pure nitrogen are key to understanding the synthesis of PtN_2. I have also shown that at pressures below the ones required for the synthesis of this new compound, other types of structure could become more stable than pyrite.

3.2 OsN_2

3.2.1 Introduction

After PtN_2, the family of late transition-metal nitrides was enlarged by the synthesis of the two new nitrides of Ir and Os [10, 11, 91]. As for Pt, these new compounds were obtained by subjecting the parent metal to extreme conditions of pressure and temperature in a nitrogen embedding medium, in a diamond-anvil cell. Interest in these compounds, as mentioned in the introduction, resided mainly in their large bulk modulus, which might suggest superhard mechanical properties. High-pressure x-ray diffraction experiments

on the three compounds give bulk moduli of 372 GPa (platinum nitride) [10], 432 GPa (iridium nitride), and 358 GPa (osmium nitride), respectively [11].

Despite intense experimental and theoretical efforts carried out by different groups after the discovery of the new family, the crystal structure of these compounds was only known in the case of platinum nitride by means of the studies described in the previous section [92, 93]. X-ray diffraction measurements were able to clarify the nature of the sub-lattice of the transition metal atoms for the two new nitrides, but due to the large atomic-number ratio between the parent metal and nitrogen, x-ray diffraction was, here again, unable to provide insight into the internal position of the nitrogen atoms, nor into the stoichiometry of the compound. The metal sub-lattice has been reported to be face-centered cubic in the case of Pt nitride [92], orthorhombic in Os nitride and rhombohedral in Ir nitride [11]. As already discussed, for the case of Pt, nitrogen atoms in pyrite PtN_2 pair up to form single-bonded dinitrogen units (N_2) which fill the octahedral holes of the fcc Pt sub-lattice. The situation of nitrogen inside Ir and Os nitrides instead, was not yet known. The similarity between the Raman spectra of PtN_2 and Ir nitride, particularly in the frequency region of the single-bonded N_2 stretching observed in PtN_2, suggests that Ir nitride could also be composed of dinitrogen units located in the interstitial holes of the rhombohedral Ir sub-lattice. The picture was however much less clear in the case of osmium nitride, where no Raman peaks were observed [11], presumably due to the metallic character of the compound.

In this section, the structural and mechanical data obtained from ab-initio calculations on OsN_2 structures are compared with the experimental data of Ref. [11], and conclude that the crystal structure of Os nitride is isostructural to that of marcasite, a known polymorph of FeS_2 structurally similar to pyrite. Therefore, it is observed that dinitrogen units similar to those found in PtN_2 are also present in OsN_2 .

3.2.2 Methodology

Calculations [53] were performed within density functional theory using a Perdew-Burke-Ernzerhoff exchange correlation functional [50] and a plane wave basis set for the electronic wave functions with a kinetic energy cutoff of 70 Ry. A pseudo-potential description of the ion-electron interaction [78] was used, with osmium's 5s and 5p semi-core electrons included in the valence. Brillouin zone integration was found to be converged with a uniform

grid of $9 \times 9 \times 9$ points (corresponding to 205 points in the irreducible zone of the marcasite structure).

3.2.3 Results and discussion

The marcasite structure has the space group *Pnnm*, with osmium atoms on the Wyckoff sites 2a [(0,0,0) and (1/2,1/2,1/2)] and nitrogen atoms on the site 4g [(x,y)], with two internal parameters x and y. Structural relaxations were thus performed by relaxing the nitrogen positions, while osmium atoms are fixed by symmetry. The calculated properties (equilibrium volume, lattice parameters, and bulk modulus) of OsN_2 marcasite are reported in Table 3.6 and agree very well with experiment. The calculated nitrogen internal parameters at 0 GPa are $x = 0.12751$, and $y = 0.40386$. A Rietveld refinement (Fig. 3.18) of the observed diffraction pattern using the*Pnnm* space group shows that the marcasite structure is fully consistent with the x-ray data.

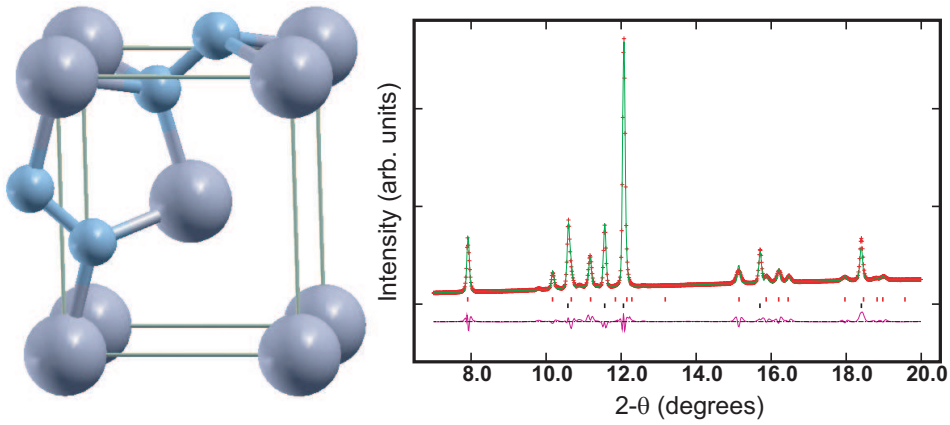

Figure 3.18: Marcasite structure of OsN_2, space group *Pnnm*. Osmium atoms (gray) form an orthorhombic lattice, dinitrogen (N_2) units (light-blue) occupy the cavities of the Os lattice. The calculated N-N distance at ambient pressure is 1.417 Å. The Rietveld fit using the *Pnnm* space-group is in excellent agreement with experiments, red crosses: data at ambient pressure (λ=0.4237 Å); green line: Rietveld fit; black ticks: OsN_2 peaks; red ticks: Os peaks. The most intense Os peaks are cut-off.

The theoretical formation energy of marcasite OsN_2, calculated as a difference between the ab-initio total energies of OsN_2 and those of Os metal and molecular N_2 in the ϵ structure at zero pressure, is found to be positive (1.15 eV), indicating that the compound is in principle thermodynamically unstable towards decomposition into its constituent elements, at zero pressure. It

	a	b	c	B, B'	ΔE (eV)
Exp. [11]	**2.714**	**4.910**	**4.102**	**358,4.67**	-
Mar. (cal.)	4.13	4.93	2.70	359, 4.28	1.15
Pyr. (cal.)	4.85			339, 3.85	2.15
Os exp.[96]	3.03			411, 4.0	-
Os cal.	3.05			411, 4.3	-

Table 3.6: Equilibrium lattice parameters (in Å), zero-pressure bulk modulus (in GPa) and its pressure derivative (B') obtained from fitting calculated energies over a range of volumes with a second order Birch-Murnaghan equation of state. Formation energies ΔE are relative to Os+N_2.

is interesting to remark that the formation energy of PtN_2 was also found to be positive, but larger than the one found here for OsN_2 [92]. This indicates a lower propensity to dissociate back into the constituent elements in the case of OsN_2, with respect to PtN_2, which is consistent with the experimental observation that much larger quantities of OsN_2 than PtN_2 have been found in the samples recovered at ambient conditions. From the calculated energies as a function of volume, at T = 0 K, we extracted the pressure dependence of the enthalpies shown in Figure 3.19.

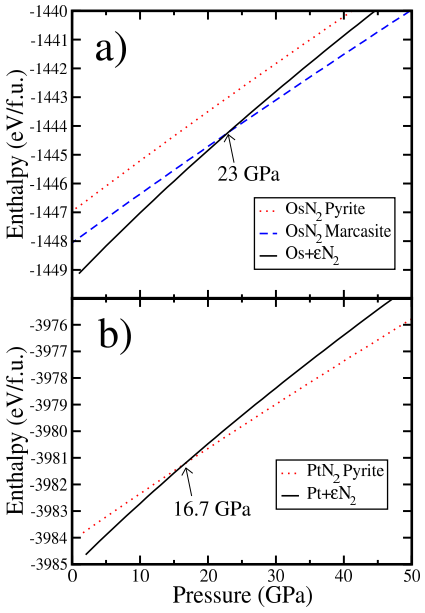

Figure 3.19: (a) Enthalpy versus pressure for OsN_2 pyrite, OsN_2 marcasite, and their constituents, at $T = 0$ K. (b) Same as in (a), for PtN_2 pyrite.

Upon application of pressure, the formation energy of OsN_2 marcasite decreases and eventually vanishes at 23 GPa (Fig. 3.19(a)) above which the compound becomes more stable than its constituents, at least at low temperature. This is consistent with the experimental finding that the compound can be synthesized only when pressure approaches 50 GPa. We also notice that the enthalpy of a hypothetical OsN_2 compound with the pyrite structure is significantly higher than that of OsN_2 marcasite, at all calculated pressures (up to 200 GPa). A more appropriate comparison of the theoretical predictions with the reported conditions for the synthesis of the compound (50 GPa, 2000 K) would require a calculation of its finite-temperature Gibbs free energy of formation, which is beyond the scope of this work. We remark however that at the conditions of synthesis, nitrogen is likely to be in the liquid state.

An extrapolation of the melting curve of nitrogen measured up to 18 GPa [94], in fact, gives 1500-1750 K for the melting temperature at 50 GPa [11], which is below the reaction temperature used in the experiment. Assuming that differences between the vibrational contributions to the free energy are negligible for the solid phases and using for the excess free energy of the liquid the empirical expression derived by Kroll based on thermochemical data [95], we obtain that, at 50 GPa the reaction temperature should be of 2100 K, in good agreement with the experimental value. We thus conclude that the synthesis of the compound is likely to occur at, or close to the thermodynamic boundary.

In an attempt to rationalize the experimental observation that the synthesis conditions of the three nitrides are nearly identical [11], in Figure 3.19(b) the enthalpy of formation for pyrite PtN_2 is reported. Interestingly, even though the calculated zero-temperature transition pressure is slightly lower than the one found for OsN_2, the zero-temperature formation energy of PtN_2 at 50 GPa is very similar to that of OsN_2 (~ -1.3eV). Under the assumption discussed above that finite-temperature corrections to the free energy can be approximated by simply considering the excess free energy of liquid nitrogen, then it appears that the thermodynamical boundaries for the high-temperature synthesis of OsN_2 and PtN_2 are likely to be very close, in agreement with the experimental findings.

I finally comment on the electronic structure of OsN_2 marcasite. Our band structure calculations (Fig. 3.20) show that, contrary to PtN_2, which is known to be an insulator [92], OsN_2 marcasite has a metallic character, which is in agreement with the experimentally observed absence of first-order Raman

peaks for this compound. Os belongs, like Pt, to the last row of the transition metal series, and has two electrons less than Pt so, an insulating character would be compatible with electron counting arguments. In order to understand why OsN_2 is a metal it is interesting to consider a hypothetical OsN_2 compound with the pyrite structure. In a simplified picture in which the density of electronic states (DOS) only depends on the crystal structure, and not on the electron filling, the electronic structure of this hypothetical pyrite-OsN_2 can be approximatively obtained from that of real pyrite-PtN_2 by removing 8 electrons from its band structure (the unit cell of PtN_2 pyrite contains 4 formula units), which corresponds to a Fermi level whose position would be the one indicated by the red line in Figure 3.21(c). This would imply a metallic character also for this hypothetical compound. The actual ab-initio calculation of the DOS of OsN_2 pyrite (Fig. 3.21(b)) confirms that the reasoning is correct, the gap at a filling of 80 electrons/cell (8 electrons above the OsN_2 Fermi level) is still present, and the Fermi level lies in a region of finite density of states.

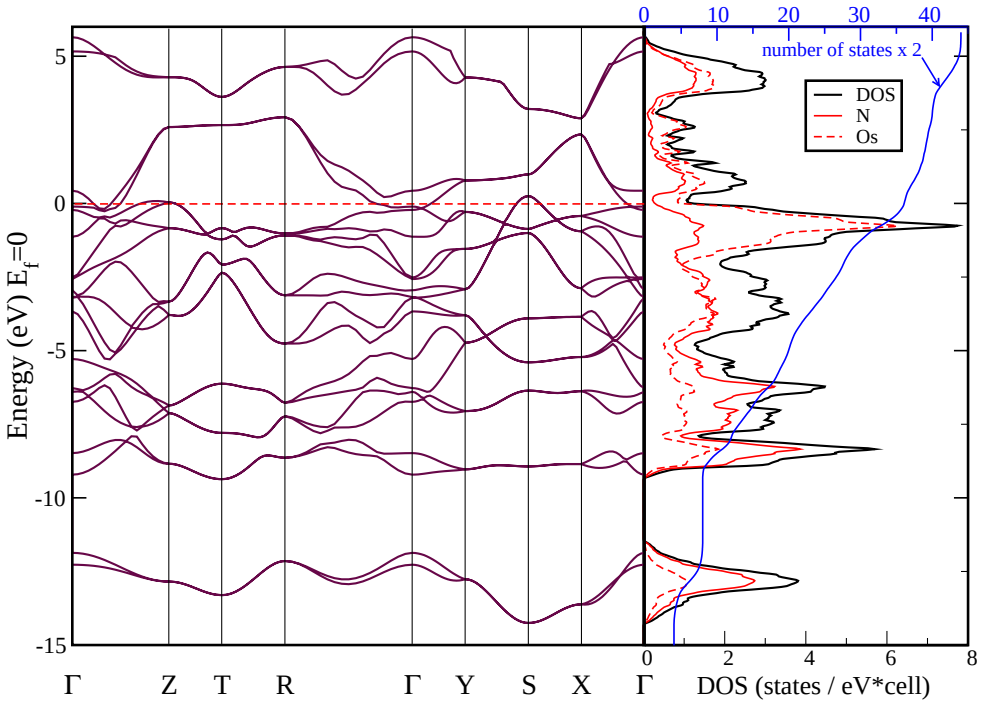

Figure 3.20: Electronic bands of marcasite OsN_2 at ambient pressure along high symmetry lines together with the corresponding density of states and its projection onto the constituent atoms. The Fermi energy is set to zero.

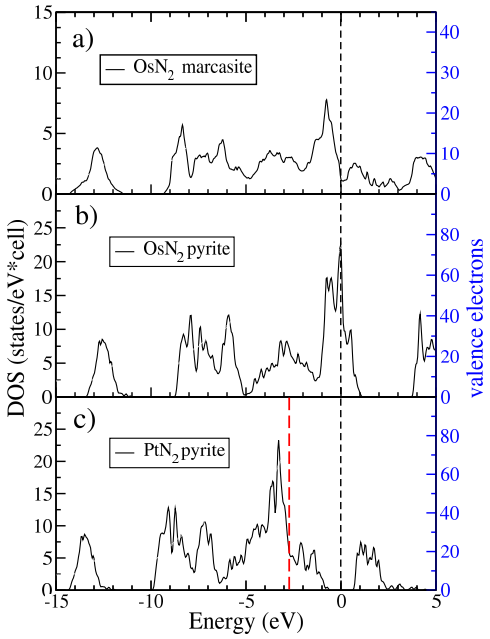

Figure 3.21: Density of electronic states and its integral for (a) OsN_2 marcasite; (b) OsN_2 pyrite; (c) PtN_2 pyrite. The Fermi energy is set to zero.

However the OsN_2 pyrite DOS has a very high density of states at the Fermi level, which is typically associated with an instability of the electronic structure, leading either to magnetism, or to structural distortions. The marcasite structure, with its simple structural connection to pyrite, can be seen as a way for the system to avoid the predicted electronic instability found in the pyrite structure. OsN_2 marcasite (Fig. 3.21(a)) shows in fact a much lower density of states at the Fermi level, which explains its lower energy with respect to OsN_2 pyrite.

3.2.4 Superconductivity in OsN_2

Introduction

Metallic compounds containing light elements such as H, Li, and B have attracted considerable attention recently due to their potential superconducting properties [97, 98, 99]. Within the weak-coupling BCS theory, high frequency phonons due to the presence of atoms with light masses ensure a large pre-factor in the BCS formula for the superconducting critical temperature T_c. Thus, even a moderate electron-phonon coupling can yield a sizable T_c [100, 101]. The discovery of superconductivity in MgB_2 [102],

B-doped diamond [103], B-doped silicon [104], and calcium and ytterbium graphite intercalated compounds [105] confirms this picture and also extends it by showing that strong covalent bonds between light atoms can provide a sizable contribution to the electronic density of states at the Fermi level, under appropriate "doping" conditions. In MgB_2 the Fermi level crosses the covalent σ bonds formed by boron atoms. Such states are partially empty as a consequence of the lowering of the π bands, caused by the Mg^{2+} attractive potential felt by the B-π electrons [102, 101]. In B-doped diamond [103], substitutional boron atoms provide hole-doping to the C-C sp^3 covalent bonds. The strong C-C bonding allows the structure to remain stable even at high doping. In electron-doped graphite intercalated compounds, the Fermi level crosses the graphitic C-π band and the intercalated band.

nitrogen follows boron and carbon in the first row of the periodic table and is characterized, in its elemental form, by a strong triple bond in the low pressure molecular phases, and by covalent single bonds in the non-molecular phase stable at pressures exceeding a megabar [106]. As a consequence, molecular phases are insulating, and the non-molecular phase is semiconducting [107]. In analogy with the boron and carbon-based superconducting compounds described above, search for superconductivity in nitrogen-based systems requires the identification of compounds where covalent bonds between nitrogen atoms persist in a stable form in the presence of doping species and of a resulting metallic state.

So far, only OsN_2 fulfills the above criteria. Covalently-bonded di-nitrogen (N_2) units are preserved in the marcasite-like crystal structure of OsN_2 [108] (see Fig. 3.22(a)), which makes this compound an obvious candidate to investigate superconductivity in nitrogen-rich systems.

In this section, I'll describe our studies on the superconducting properties of OsN_2 in the framework of a phonon mediated pairing mechanism. We performed *ab-initio* calculations of the Fermi surface, electronic bands, phonon dispersions, and electron-phonon couplings in OsN_2, and demonstrate that the high-frequency modes originating from the covalently-bonded N_2 units are strongly coupled to the electronic states at the Fermi level and give rise to a T_c of about 1 K. We also show that within this framework, the superconducting temperature can be greatly increased by hole-doping.

Methodology

Here, once again, calculations were performed with the Quantum Espresso package [53] employing density functional theory and the Perdew-Burke-

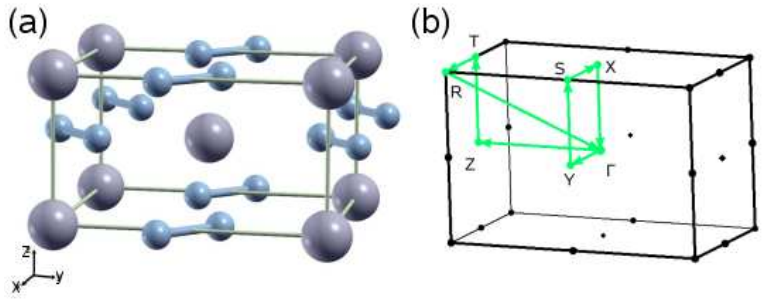

Figure 3.22: (a) Crystal structure of OsN_2 (isostructural to marcasite). The space group is *Pnnm*, with osmium atoms (gray) in the Wyckoff sites $2a$ and nitrogen atoms (blue) in the $4g$ sites [108]. (b) Brillouin zone showing the high-symmetry directions used in Figs. 3.23 and 3.24.

Ernzerhoff exchange-correlation functional [50]. An ultra-soft pseudo-potential description of the ion-electron interaction [78], with Os 5s and 5p semi-core electrons included in the valence, was used together with a plane-wave basis set for the electronic wave functions and the charge density, with energy cut-offs of 40 and 480 Ry respectively. The dynamical matrices and the electron-phonon coupling constants λ were calculated using density functional perturbation theory (DFPT) in the linear response regime [53, 17]. The electronic Brillouin zone (BZ) integration in the phonon calculation was sampled with a $20 \times 16 \times 30$ uniform k-point mesh. The electron-phonon coupling was found to be converged with a finer grid of $26 \times 22 \times 40$ k-points and a Gaussian smearing of 0.006 Ry. The dynamical matrix was computed on a 2^3 mesh of phonon wave vectors q. The phonons dispersion was then obtained on a finer 8^3 q-mesh by Fourier interpolation of the real space inter-atomic force constants. In this way, λ is calculated over a 8^3 q-point mesh.

Results and discussion

In the energy range shown in Figure 3.23, the total electronic density of states (DOS) is essentially determined by Os $5d$ and N $2p$ orbitals (Fig. 3.23(b)). At the Fermi level the N $2p$ orbitals contribute with about 20% of the total DOS. The projection on the atomic orbitals also shows that 92% of the nitrogen contribution at E_F is due to N $p_{x,y}$ states and the remaining 8% to N p_z states. The N $p_{x,y}$ orbitals lie in the plane containing the N-N units, and are thus directly involved in the formation of the N-N covalent bond in OsN_2. Integrating the DOS in a window of energy close to E_F (between E_F and 1 eV below E_F) we found an antibonding character for the electronic states on

the N-N units. This is consistent with the considerable weakening of the N-N bond in OsN_2 with respect to the molecular triple bond, and is confirmed by the large reduction of the N-N stretching frequency from 2300 cm^{-1} in the molecular state to 500-800 cm^{-1} in the compound. A non-negligible coupling of the electronic states close to E_F with the N-N stretching vibrational modes can thus be anticipated based on simple band-structure considerations. It is interesting to remark that the presence of the Os sublattice is crucial to the presence of a finite nitrogen component in the DOS at E_F. Indeed, a band structure calculation for a pure nitrogen system obtained by removing the Os atoms from the crystal structure of OsN_2 letting everything else unchanged, gives an insulating solid; indicating that the nitrogen component at E_F arises from the coupling of the N-N units with the transition metal sublattice, through re-hybridization and/or charge transfer.

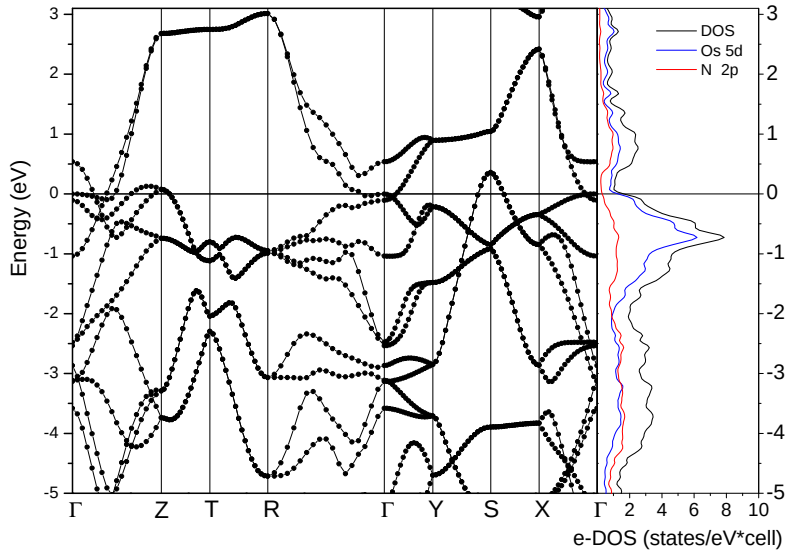

Figure 3.23: Left panel: A more detailed view around the Fermi energy of the electronic bands of marcasite OsN_2 at ambient pressure along the high symmetry lines shown in Figure 3.22(b). Right panel: electronic density of states and its projection onto the Os $5d$ (blue) and N $2p$ (red) orbitals. The Fermi energy is set to zero.

Due to the presence of stiff N-N bonds, the calculated phonons of OsN_2, shown in Figure 3.24, can be divided into three main groups: a low-frequency group (up to 200 cm^{-1}) involving mostly the Os sub-lattice, an intermediate group corresponding to the librational modes of the N-N units (between 250 and 600 cm^{-1}), and a high-frequency manifold corresponding to rotation and

stretching of the N-N units (above 600 cm^{-1}). The eighteen phonons modes of the marcasite structure belong to eight irreducible representations. Four of these representations (B_{1g}, B_{2g}, B_{3g}, and A_g) are associated with nitrogen displacements only, with osmium atoms at rest, and are highlighted with symbols in Figure 3.24. Representations B_{2g} and B_{3g} have one mode each and involve di-nitrogen vibrations along the $\hat{z}$ axis, while representations, A_g and B_{1g}, have two modes and involve vibrations along the $\hat{x}$ and $\hat{y}$ directions. In B_{2g} and A_g both dinitrogen units oscillate in-phase while in B_3g and B_{1g} the N-N units vibrate in counter-phase. As we can see from Figure 3.24, the nitrogen light mass and the covalent N-N bond ensures a high frequency for these modes, with A_g and B_{1g} modes ranging between 640 and 825 cm^{-1}. Raman peaks in this frequency range have been observed experimentally also in PtN_2 and IrN_2 and have already been associated with the stretching of the N-N units [10, 11, 92, 91]. As a confirmation of the planar (xy) nature of bonding in N-N, we note that the xy-polarized phonons in the A_g and B_{1g} representations are higher in frequency with respect to z-polarized modes.

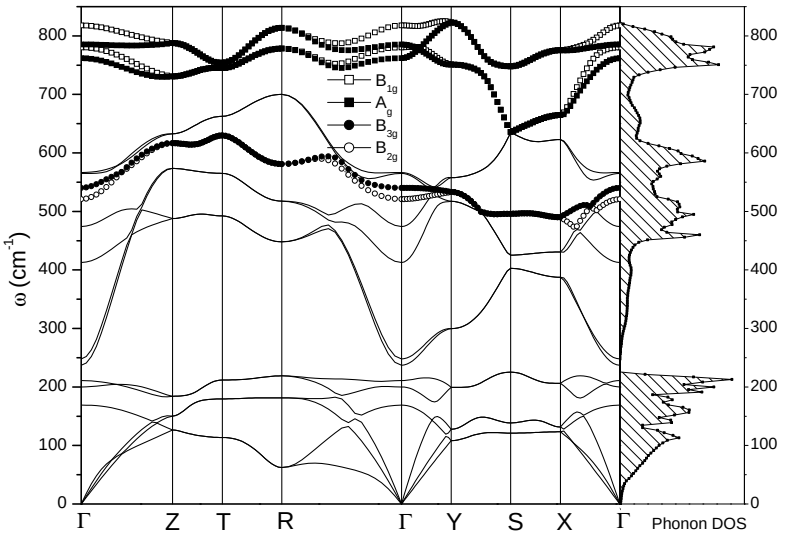

Figure 3.24: Phonon dispersions along high-symmetry directions of the Brillouin zone and corresponding phonon density of states (right panel).

Within DFPT [17] the electron-phonon interaction for a phonon mode ν with momentum $\mathbf{q}$ can be calculated as

$$\lambda_{\mathbf{q}\nu} = \frac{4}{\omega_{\mathbf{q}\nu} N(E_F) N_k} \sum_{\mathbf{k},n,m} |g^{\nu}_{\mathbf{k}n,\mathbf{k}+\mathbf{q}m}|^2 \delta(\epsilon_{\mathbf{k}n}) \delta(\epsilon_{\mathbf{k}+\mathbf{q}m})$$

where the sum is over the Brillouin Zone. The matrix element is $g^{\nu}_{\mathbf{k}n,\mathbf{k}+\mathbf{q}m} = \langle \mathbf{k}n|\delta V/\delta u_{\mathbf{q}\nu}|\mathbf{k}+\mathbf{q}m\rangle/\sqrt{2\omega_{\mathbf{q}\nu}}$, where $u_{\mathbf{q}\nu}$ is the amplitude of the displacement of the phonon and V is the Kohn-Sham potential. The electron-phonon coupling is calculated as a BZ average over the phonon wave vectors $\lambda = \sum_{\mathbf{q}\nu} \lambda_{\mathbf{q}\nu}/N_q$. The Eliashberg spectral function $\alpha^2F(\omega)$ is defined as

$$\alpha^2F(\omega) = \frac{1}{2N_q}\sum_{\mathbf{q}\nu} \lambda_{\mathbf{q}\nu}\omega_{\mathbf{q}\nu}\delta(\omega - \omega_{\mathbf{q}\nu}) \tag{3.1}$$

and allows to compute $\lambda(\omega) = 2\int_0^{\omega} d\omega' \alpha^2F(\omega')/\omega'$.

Figure 3.25(a) shows the Eliashberg spectral function $\alpha^2F(\omega)$ calculated from Eq. 3.1. Three separate contributions to the electron-phonon interaction can be clearly distinguished and attributed to the low frequency, the intermediate frequency, and the high frequency phonons, respectively. Two high-frequency peaks are particularly strong and well resolved, and are associated with the contribution of the two A_g phonons, while the contribution of the B_{2g} and B_{3g} phonons accounts for most of the electron-phonon interaction in the intermediate frequency range from 500 to 600 cm^{-1}. The integral $\lambda(\omega)$, represented by a dashed line in Figure 3.25 (a), shows that the low frequency phonons, that involve mostly displacements of the osmium atoms, account for a contribution of $\lambda = 0.17$. The high frequency phonons associated with the stretching of the covalently bonded N-N units contribute with an equivalent amount, which brings the total λ for OsN_2 to 0.37. More insight about the nature of the electron-phonon interaction that leads to such a large contribution to λ from N-N bonds can be obtained by analyzing the changes of the Fermi surface (FS) that arise upon distorting the lattice along the relevant phonon modes. In particular, we concentrate on the A_g modes that show the highest $\alpha^2F(\omega)$ values and dominate the high frequency contributions. In Figure 3.25(b,c) we compare the FS of the undistorted OsN_2 with that of a distorted OsN_2 crystal obtained by changing by 4% the distance between nitrogen atoms in the N-N units along the xy-polarized A_g mode. The most relevant change in the FS is the migration of electrons from the bands that contain the hole pockets at Z to the bands that contain the electron pockets near Γ. Interband electron transfer is generally associated with a large electron-phonon coupling, which is consistent with our finding of a large contribution of the A_g modes to λ.

The superconducting critical temperature can be estimated using the McMillan formula [109]:

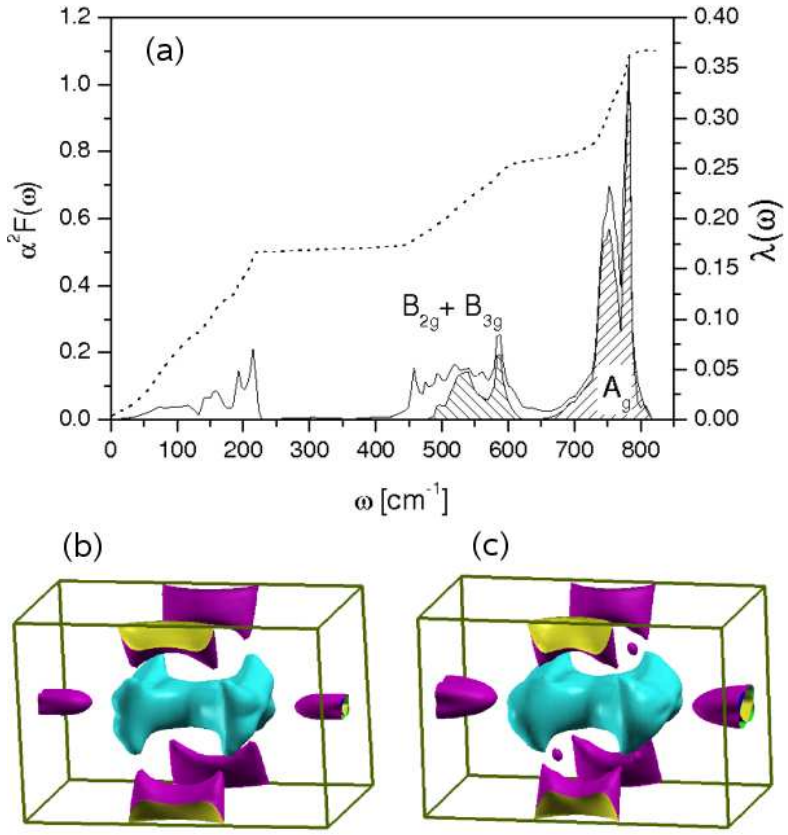

Figure 3.25: (a) Eliashberg function $\alpha^2F(\omega)$ (continuous line) and integrated coupling $\lambda(\omega)$ (dashed line) of OsN_2. The shaded regions are the B_{2g}, B_{3g}, and A_g contributions to α^2F. (b) Calculated Fermi surface of OsN_2. The Fermi surface consists of three electron pockets located close to the zone center, only one of which is visible (green pocket), and of four hole pockets, two of them centered at Z and two at the S point. (c) Fermi surface upon distortion of the lattice along a A_g phonon.

$$T_c = \frac{\langle \omega_{\ln} \rangle}{1.2} \exp\left(-\frac{1.04(1+\lambda)}{\lambda - \mu^*(1+0.62\lambda)} \right) \tag{3.2}$$

where the parameter μ^* is the screened Coulomb pseudo-potential and $\langle \omega_{\ln} \rangle$ = 280 K is the logarithmically averaged phonon frequency. For OsN_2 we obtain $T_c \approx 1$ K, assuming μ^*=0.1. We thus conclude that the insertion of nitrogen enhances the superconducting properties of osmium by raising T_c from 0.65 K in the elemental metal up to 1 K in OsN_2.

A careful examination of the electronic DOS of OsN_2 (Fig. 3.23) suggests that hole-doping could further enhance T_c. Hole-doping in OsN_2 would, in fact, lower the Fermi level towards a region of higher electronic DOS and would, at the same time, stiffen the N-N bonds by partially emptying the anti-bonding states below E_F. The reported synthesis of several nitrides from different transition metals (Pt, Ir, Os, Pd) suggests that the synthesis of transition metal nitride *alloys*, i.e. of compounds with N-N units inserted in a matrix of mixed metal composition is not impossible. Alloys with different composition may allow a tuning of the electronic DOS, as already observed for pure transition-metal alloys [110].

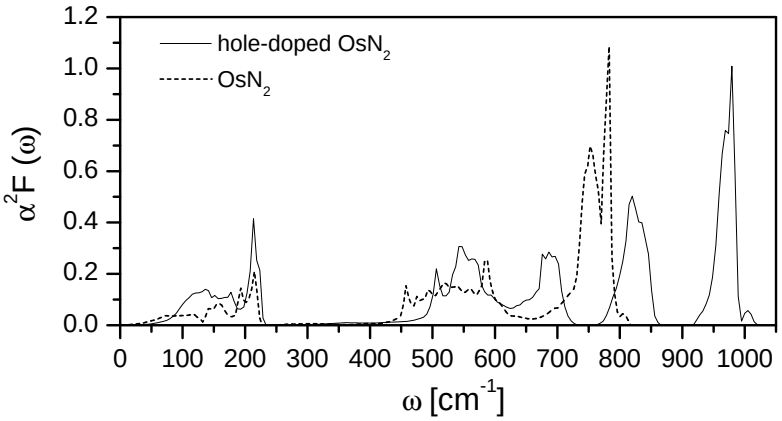

Figure 3.26: Eliashberg function $\alpha^2 F(\omega)$ of hole-doped OsN_2 (continuous line) and un-doped OsN_2 (dashed line).

In order to explore the consequences of hole doping, we carried out *ab-initio* calculations of OsN_2 with a hole doping of 0.5 holes/unit cell, corresponding, e.g., to a hypothetical alloy with $Os_{0.75}Re_{0.25}N_2$ composition. As expected the DOS at E_F increases about 2.4 times with respect to the undoped case. The electron-phonon coupling matrix elements remains approximately the same in the doped and undoped cases, but the phonon frequencies associated

to the N-N modes increase by about 200 cm^{-1} (Fig. 3.26), which confirms the strong coupling of these modes with the electronic states close to the Fermi level. The frequency increase causes an increase of $\langle\omega_{\ln}\rangle$ to 310 K. The total electron-phonon coupling parameter, λ, increases to 0.49, leading to a superconducting critical temperature of $\simeq$ 4 K for doped OsN_2.

3.2.5 Conclusions

As a conclusion for the last two sections; here I have shown that the OsN_2 compound, recovered from DAC experiments to ambient conditions, has the marcasite structure and is a superconductor. I have also shown that its superconducting properties are connected with a strong coupling between the stretching modes of the covalently bonded N_2 units with the electronic states at the Fermi level, similarly to what has been observed in a number of boron and carbon-based compounds, including MgB_2. We predict an enhancement of the superconducting temperature by doping OsN_2 with holes, which we believe can be achieved experimentally by synthesizing the nitride starting from a hole-doped Os alloy. Hopefully this work will stimulate the experimental search for new members of the dinitride family with metallic character and potential superconducting properties.

Chapter 4

CO_2

Carbon, silicon, and germanium, although isoelectronic and close in their solid-state behavior in several ways, differ markedly when fully oxidized. While silicon and germanium are bulk, extended compounds, carbon dioxide forms a very stable molecule at ambient conditions. Carbon dioxide is one of the most abundant volatile materials in Earth's atmosphere as well as on other planets in the solar system, and its presence has tremendous implications on the viability of life as we know it. Its study bears great importance for planetary sciences, because of the enormous amounts of CO_2 that are found as clathrates on Mars and other planets, and because of its presence under a wide range of pressures in the atmospheres of giant planets. Also, from a non-geological point of view and letting aside environmental aspects, CO_2 crystals (i.e. CO_2 in the "dry ice" molecular phase $Pa3$, that sublimes directly into the vapor phase under ambient conditions) are relevant technologically since they are widely used for cooling, mainly due to the fact that this phase constitutes an inexpensive, nontoxic, and nonflammable compound. However, the properties of CO_2 at high pressures are not clearly understood in what concerns the transition boundaries between its stable and metastable, molecular and non-molecular, phases on its phase diagram, and the structures linked to them (Fig. 4.1) [111, 112].

The search for new allotropic or polymorphic phases of known compounds is a fascinating area which can lead to materials that exhibit unusual properties and that are also often attractive from the fundamental point of view. On the other hand, extreme conditions of pressure and temperature, make possible the synthesis of many of those new materials, and also open the door to understanding the nature of chemical bonding, intermolecular interactions, and collective behavior of these new condensed phases. The outstanding capacity that extreme conditions exhibit to favor the synthesis of new phases and

compounds is explained by the fact that at high pressures, multiple bonds such as the double bonds that characterize molecular CO_2, become unstable because of the rapid increase of electron kinetic energies induced by the volume reduction which, finally, overtakes the locally attractive electrostatic potential energies for valence electrons. These transitions, often occur systematically among similar elements, and in principle can be also enhanced with catalytic elements, providing an unparalleled and so far little explored opportunity for devising and synthesizing novel materials.

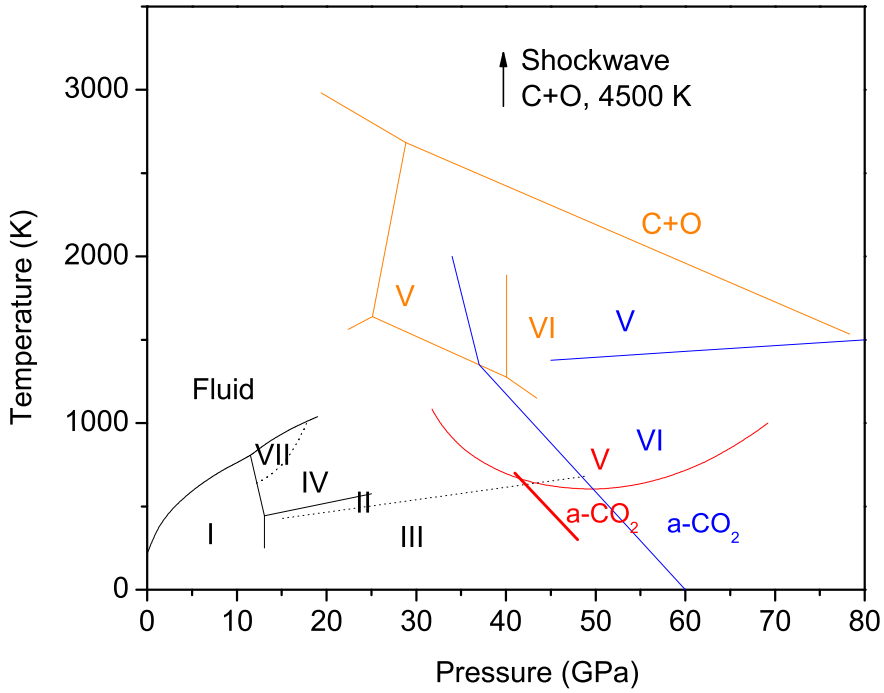

Figure 4.1: Thermodynamic and kinetic phase diagram of solid phases of CO_2, taken from Ref. [112], here: continuous lines represent phase boundaries delimiting CO_2-I, II, III, IV, and VII; dotted line, kinetic transformation boundary between phases II and III, and also between phases IV and VII; red lines, kinetic transformation boundary from molecular to non-molecular CO_2; orange and blue lines, approximate kinetic transformation boundaries from molecular CO_2 to the extended covalent phases V and VI, and to dissociation.

The condensed region in the thermodynamic and kinetic phase diagram of

CO_2 seems to consist so far of five molecular crystalline phases: phase I (or "dry ice") which is a *true* molecular phase, phase II (stable above 12 GPa), phase III (only metastable, seen above 12 GPa), phase IV (stable above 8 GPa but only at high temperatures), and phase VII (stable around 1000 K at pressures located between the melting line and 10 GPa) [113], one polymeric phase found experimentally above 50 GPa and 600 K (phase V, whose crystal structure remains unknown), one amorphous phase metastable above 50GPa but at lower temperatures than those of phase V (has been given the name of "carbonia" by its discoverers [13], and is studied in this work) and, finally, there is a recent report of a new crystalline phase (phase VI) obtained at around 60 GPa and 600 K which has been described as consisting of CO_6 octahedra [14]. To some of these phases, some outstanding properties have been associated, as for example: the increase of the strength of CO_2 with pressure in phase III, and the non-linear optic and superhard properties of the polymeric phase V [12, 114]. CO_2 at ambient pressure is interesting by itself, given its large quadrupole moment (-4.3×10^{-26} esu cm^2) [115], and has been used often as a model for understanding the role of quadrupolar interactions in condensed matter.

Pressure-induced changes often occur in systematic ways, providing new routes for designing and synthesizing novel materials with advanced optical and mechanical properties. The structures of the N_2 polymer, diamond, and β-C_3N_4 at high pressures, for example, can be viewed as being similar to the assemblages of heavier elements in each periodic group (P, Si, and $\beta-Si_3N_4$, respectively) at low pressures. High-pressure structures for CO_2 haven't escaped similar comparisons with their possible counterparts, already present in SiO_2 and GeO_2 phases.

To summarize, in contrast with silica, the stability of the CO_2 molecule is so overwhelming that non-molecular solid state forms appear only at high pressures and are still poorly characterized. This is in agreement with the fact that, historically, many simple molecular solids made of the first and second row elements such as CO_2, N_2, H_2O, CH_4, etc. have been often considered as inert at relatively low pressures, and, in fact, high stabilities of these molecules have also been very often assumed even at very high pressure and temperature, as they are found to be major detonation products of energetic molecules. However, since new chemistry can exist under extreme conditions, the idea that the two double carbon-oxygen bonds could be alternatively distributed by forming just single bonds, hence doubling the number of bonds, or even up to six bonds having then similarities with the polymorphs of SiO_2, has been put forward many times. Because of all the considerations exposed

above, the study of the high pressure behavior of CO_2 is crucial for understanding planetary evolution, fundamental physics of molecular crystals, and also for finding possible future technological applications.

In the first part of this chapter I address the important issue of CO_2 amorphization induced by pressure. Pressure-induced amorphization has been previously observed for several compounds, water [116] and silica [117] being the most studied examples. Such a phase, was experimentally attained for CO_2 by M. Santoro *et al.* in 2006 [13] and at that time, its structure was reported to be compatible with a mixture of the two types of coordination (tetrahedral and octahedral) found also in silica. I report here that, instead, carbonia [13], and possibly also the novel phase VI [14], contain a sizable amount of semi-reacted carbon in three-fold coordination.

The second part of the chapter addresses the problem of the recoverability of extended CO_2 phases. Carbonia, and also phase VI, have been observed to be recoverable down to 20 GPa. This is the point in which molecular CO_2 starts being again more favorable than tetrahedrally coordinated phases. The extended phase then breaks and gives place usually to dry ice. I show, that doping with a transition-metal could be the solution for bringing the amorphous, and probably also other extended CO_2 phases, down to ambient conditions.

Even if we will not provide the final answer to all the questions raised by the recent experimental findings, computer simulations with their almost unlimited access to hypothetical structures, offer invaluable help in establishing the nature of properties measured under compression. For example, in section 4.1, we will discuss the properties of the amorphous phase also based on analogies with a series of hypothetical crystals with a range of different local geometrical arrangements. In the second part of this chapter (section 4.2), pressure-induced changes on a molecular CO_2 system doped with a titanium impurity are studied starting from two different molecular configurations, namely, the CO_2's II and III molecular phases. This was done in order to assess the role of the starting configuration as well as other conditions associated to the experimental set-up and the sample's history. This gains special relevance for CO_2, because boundaries between high-pressure phases of CO_2 are blurred, up to the point in which even different metastable molecular phases are easily accessible as starting points before compression.

4.1 Amorphous phase

4.1.1 Introduction

The carbon-oxygen double bond in CO_2 is one of the strongest molecular bonds in nature at ambient conditions, but it undergoes important reorganization and weakening under pressure. In the half-megabar (50 GPa) pressure range, solid molecular CO_2 transforms into extended, single-bonded phases presumably similar to the ambient-pressure phases of silica (SiO_2) and germania (GeO_2) [118, 112]. Vibrational spectra and diffraction patterns of CO_2-V, the first reported non-molecular crystalline phase of CO_2, suggest structural similarities between CO_2-V and two tetrahedral phases of silica: cristobalite and trydimite [112, 12, 114, 119, 120, 121, 122, 123, 124, 111]. Ab-initio calculations find a β-cristobalite-like crystal with $I\overline{4}2d$ space group as the most stable phase of CO_2 at 50 GPa, among a number of silica-like isomorphs [122, 123]. The analogy with silica has been recently extended to include a second crystalline form (phase VI) [14], and an amorphous, non-molecular form of CO_2 (a-CO_2 or carbonia) [13], which will be the topic of this section. Similarities between the infrared (IR), Raman and x-ray diffraction data of a-CO_2 with those of other group IV dioxide glasses were taken as evidence that carbonia is structurally similar to SiO_2 and GeO_2 glasses at high pressure, and thus characterized by a mixed tetrahedral and octahedral coordination for carbon. In particular, IR spectra for carbonia at 50 GPa match those of octahedral silica glass at similar pressures [13], once frequencies are rescaled to account for the atomic mass difference between Si and C. Moreover, the x-ray structure factor of carbonia was found to be similar to that calculated for a hypothetical high-pressure silica-like CO_2 glass obtained by replacing Si with C in a theoretical sample of compressed SiO_2 glass scaled to match the CO_2 volume [13]. Octahedral coordination has also been proposed to characterize phase VI, which, according to diffraction data, may be isostructural to stishovite [14]. However this picture is not supported by first-principle total-energy calculations [119, 120, 122, 123], which predicted a transition pressure from four- to six-fold coordination at around 400 GPa [120]. First-principle molecular dynamics simulations up to 120 GPa and at two different temperatures (1000 K and 2000 K) also do not yield any evidence of octahedral coordination [119].

In this section, I show that we can resolve this controversy by combining: first-principles constant pressure molecular dynamics, density-functional perturbation theory and novel experimental IR spectra, of a-CO_2. The final conclusion being that the new a-CO_2 is not SiO_2-like, and instead contains

a sizable amount of carbon in three-fold coordination, with the remaining carbons in four-fold (tetrahedral) coordination.

4.1.2 Methodology

Calculations were performed with the Quantum Espresso package [53] employing density functional theory and the Perdew-Burke-Ernzerhoff exchange-correlation functional [50]. A norm-conserving pseudo-potential description of the ion-electron interaction was used together with a plane-wave basis set for the electronic wave functions and a kinetic energy cut-off of 80 Ry. Brillouin-zone integration was found to be converged with a uniform grid of $2 \times 2 \times 2$ points for the 24-atom super-cell and $7 \times 7 \times 7$ points for smaller samples. Structural optimizations were performed on lattice parameters and atomic coordinates, at a pressure of 60 GPa, unless otherwise stated. Phonon frequencies and IR/Raman intensities were calculated using density-functional perturbation theory [17].

The simulated sample used for comparison with the experimental data on carbonia was generated starting from an amorphous structure obtained in a previous ab-initio molecular dynamics simulation [119]. The static structure factor calculated for this sample shows reasonable agreement with the experimental data on a-CO_2 [13], the sample didn't contain any homo-polar bond but contained a small number of unsaturated bonds, indicating incomplete polymerization. In order to improve the quality of the simulated sample, it was quenched to zero pressure and 0 K, annealed for 5 ps at 200 K [31], and finally brought to 60 GPa at 0 K. All bonds were saturated by the annealing process and the structure factor was essentially unaffected, demonstrating that the sample is locally-stable even at zero pressure. A phonon calculation on the resulting amorphous structure yielded only non-imaginary frequencies and hence, it further confirms that the sample stays mechanically stable also at 60 GPa. The simulated sample contains 60% of the carbon atoms in four-fold coordination, whereas the remaining 40% are three-fold coordinated (Fig. 4.2(a)), a coordination state not yet observed in significant quantities in other group IV dioxide solids.

For the experimental studies carried out by our collaborators at the European Laboratory for Non-linear Spectroscopy (LENS) in Florence, pressurized CO_2 (6 bar, purity $\geq$ 99.99%) was cryo-loaded, in the liquid phase, in a diamond anvil cell equipped with type IIa diamonds. The sample diameter and thickness were typically equal to 100-150 μm and 25-40 μm, respectively. The

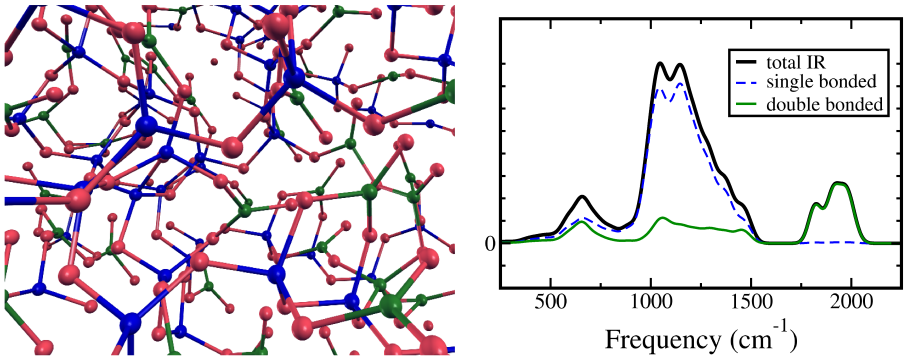

Figure 4.2: Simulated structure and IR spectrum of carbonia. a) Annealed non molecular a-CO_2 simulated sample at 60 GPa, showing four-fold coordinated carbon atoms (blue), three-fold coordinated (green) and oxygen (red). b) Theoretical IR absorbance (black) and its local projection on atoms linked exclusively by single bonds (dashed blue) and on atoms with a double bond (carbonyl sites, in green).

local pressure was measured by the R1 ruby fluorescence band shift [125]. Several pressure-temperature scans of the phase diagram were performed up to 53 GPa and 710 K, by means of uniform resistive heating of the cell. In particular, two isothermal pressure scans were performed at temperatures equal to 473 and 633 K, respectively, in the pressure range of 20-52 GPa, in order to monitor the formation of a-CO_2 from the molecular solid phase II, which occurred for pressures above 40 GPa. Temperatures were measured by a J-type thermocouple, placed 1 mm away from the diamonds. Details of our IR spectroscopy apparatus are reported elsewhere [126, 127]. The range of high temperatures investigated was the most challenging point of the experiment, since the hot sample region produces a huge thermal-radiation background which affects the signal-to-noise ration of the in situ IR spectra.

4.1.3 Results and discussion

At the onset of the transformation the amount of a-CO_2 increased upon increasing pressure, as shown by the strong, non-molecular IR absorption band between 800 and 1500 cm^{-1} (Fig. 4.3(a)). The pressure rise was stopped when about 10% of the sample had transformed (at about 52 GPa), in order to avoid saturation of the IR absorption. Comparison with the data reported in Ref. [13] and with data along the two isotherms shows that the shape of the infrared bands depends on the sample history (see Fig. 4.3(b)), as expected in the formation of amorphous, metastable materials. A previously unno-

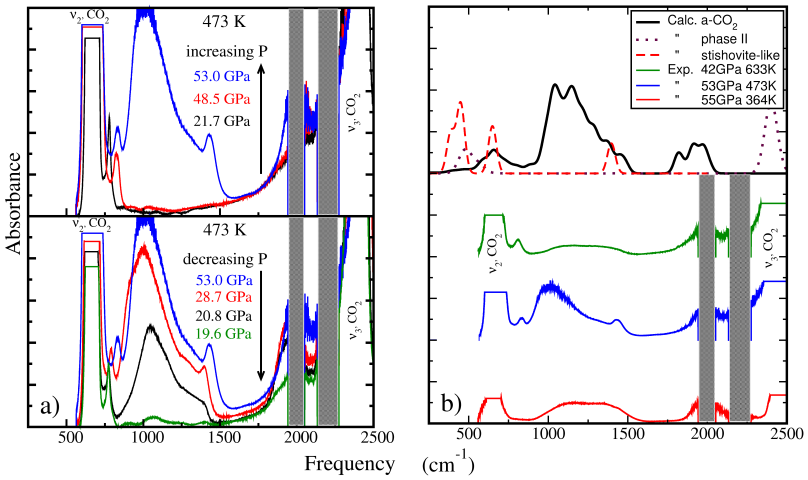

Figure 4.3: IR spectra. a) Experimental IR spectra along the 473 K isotherm showing the onset of carbonylic signatures around 2000 cm^{-1}. Grey areas mark regions dominated by diamond absorption. b) Calculated (up) and experimental (lower three) spectra. All calculations were done at 60 GPa. Experimental samples were obtained through different P-T paths, the lowest in temperature (red curve) has already been reported in [13].

ticed peak can be clearly distinguished in the experimental spectra on the two sides of the diamond absorption band, slightly below 2000 cm^{-1}, whose frequency differs clearly from the frequency of the molecular stretching mode (above 2400 cm^{-1}). The intensity of the new peak changes concomitantly with changes in the other a-CO_2 signatures at 800-1500 cm^{-1} (Fig. 4.3(a)), demonstrating that this feature belongs to the vibrational spectrum of the new phase. The IR spectrum calculated at 60 GPa (Figs. 4.2(b), 4.3(b)) shows remarkable agreement with the experimental data. Projecting the displacement components of the calculated modes on the different atoms (Fig. 4.2(b)) shows that the broad peak around 2000 cm^{-1} is completely localized on the carbonyl (C=O) units of the three-fold coordinated carbon atoms. The main peak between 800 and 1500 cm^{-1} is primarily localized on tetrahedral units, and can therefore be interpreted as the analogue of the peak centered at 1050 cm^{-1} in the IR spectrum of SiO_2 glass at ambient conditions [128]. To summarize, diffraction patterns and IR spectra on carbonia point clearly to a local structure consisting of a mixture of four-fold and three-fold coordinated carbon atoms, in similar proportions.

Even though mixed three- and four-fold coordination explains the experimental data, we performed an extensive theoretical search for octahedral

structures that might also be compatible with the experimental results. We started by considering the octahedral structure proposed in Ref. [14]. In order to achieve this, we used a super-cell with 4 CO_2 units and fixed its volume and lattice parameters to the experimental values, then, we mimicked disorder by placing the four carbon atoms in positions chosen randomly among the equivalent possibilities given by Figure 5(b) in Ref. [14]. Structural relaxation led the structure to decompose back into molecular phase II. Similar results were obtained starting from stishovite, α-PbO_2 and $CaCl_2$-like structures. Starting atomic internal parameters for these phases were taken from their silica counterparts [129] and lattice parameters were scaled to match CO_2 volumes. By symmetry constraints, we managed to stabilize a metastable stishovite-like octahedral structure at 60 GPa and were able to calculate its IR spectrum (Fig. 4.3(b)), which we take as representative of CO_2 octahedral structures. The position, shape and distribution of the peaks is completely different from the observed spectra in carbonia. Calculated frequencies do not exceed 1500 cm^{-1} and thus fail to reproduce the high frequency modes at $\sim$ 2000 cm^{-1}. It is interesting to remark that a strong peak around 2000 cm^{-1}, i.e. at a position coinciding with the carbonia C=O modes, is also reported in the Raman spectra of phase VI [14] (Fig. 4.4(a)).

Hence, theoretical evidence suggests that at least up to 60 GPa, octahedral coordination for carbon is not likely to be stable nor to be able to explain the observed vibrational spectra of carbonia and phase VI in what regards the IR/Raman active modes close to 2000 cm^{-1}. In fact, the Raman spectrum of phase VI [14] can be interpreted as composed of narrow crystalline peaks emerging from broad amorphous components similar to those reported for carbonia. This suggests the possibility that crystalline counterparts of carbonia, i.e. phases with mixed three-/four-fold coordination could exist, even if in a metastable form, and that phase VI might be one of them. In order to clarify this issue, and provide a theoretical framework for the interpretation of the observed vibrational spectra of carbonia, IR and Raman spectra were calculated for $I\overline{4}2d$ β-cristobalite and for three hypothetical model crystals containing pure three-fold coordinated (poly-carbonyl) and mixed, three- and four-fold coordination of the carbon atoms (Fig. 4.5). The two mixed structures (mix-a and mix-b) were chosen as representative of different relative amounts of three-fold and four-fold coordination, and different arrangements of the different carbon species. In mix-a, tetrahedral and carbonyl units are arranged in a periodic alternate fashion, in mix-b instead, each carbonyl group is separated by a pair of tetrahedral units. Table 4.1 reports the relative percentages of single- and double-bonded oxygen atoms present in these samples.

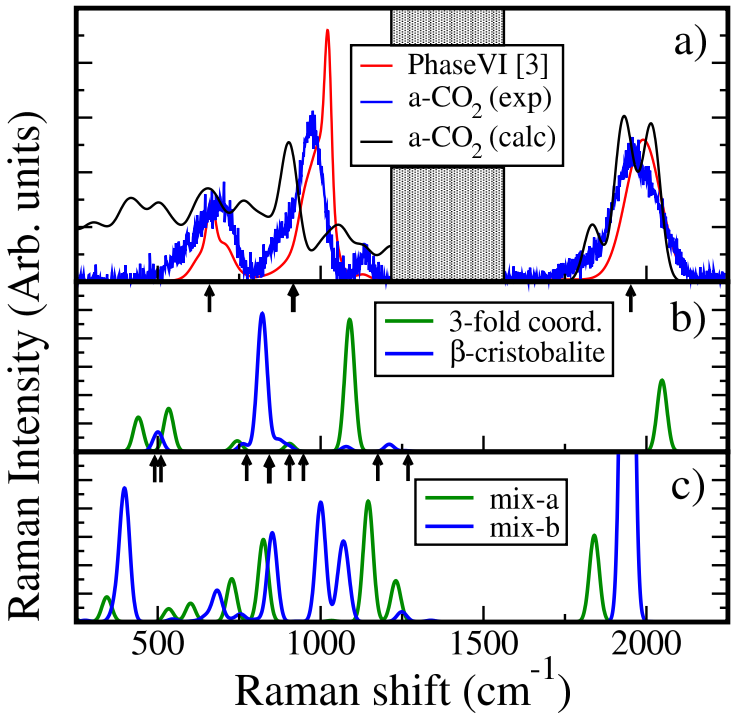

Figure 4.4: Raman spectra. a) Spectra from experiments on a-CO_2 at 76 GPa [13], phase VI at 62.5 GPa [14] and calculated for the simulated amorphous sample. Arrows indicate interpolated positions of the peaks of carbonia at 60 GPa, based on measurements at 43 GPa and 76 GPa. Grey area marks the region dominated by diamond absorption. b) Spectra calculated for the three- and four-fold coordinated crystals described in the text. Arrows mark the position of peaks in phase V. c) Spectra calculated for the mixed coordination crystalline structures shown in Figure 4.5. All calculated spectra were obtained at 60 GPa.

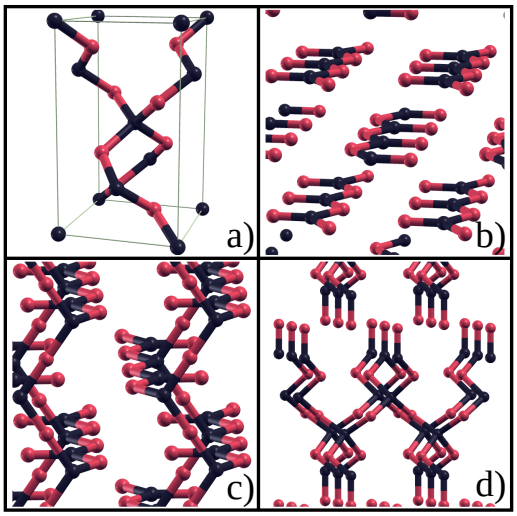

Figure 4.5: Hypothetical structures. a) CO_2 β-cristobalite (100% four-fold coordinated structure), b) planar chains with three-fold coordinated carbon atoms (100% three-fold coordinated structure), c) layered structure (mix-a) containing single tetrahedral units placed between three-fold coordinated carbon atoms along the layers, d) layered structure (mix-b) with two interconected tetrahedral units placed between carbonyl units.

In Figure 4.4, we compare the Raman spectra reported for carbonia and phase VI, with those calculated for the four theoretical structures, as well as for the simulated carbonia sample. We remark that our calculated β-cristobalite Raman spectrum matches perfectly (arrows in Fig. 4.4(b)) the observed spectrum for phase V at 60 GPa [12, 114, 111]. As expected, the peak around 2000 cm^{-1} only appears in structures containing carbonyl (C=O) units. Therefore, carbonia and phase VI must contain sizable amounts of carbon in three-fold coordination. On the other hand, the series of lower frequency peaks between 600 to 1200 cm^{-1}, which, similarly to the IR spectral decomposition (Fig. 4.2(b)), are related to tetrahedral carbon-coordination, display a large variation among the four candidates. The main peaks in carbonia and phase VI (Fig. 4.4(a)) lie at a frequency 13% and 24% higher than the main peak of β-cristobalite, respectively (Table 4.1), whereas the hypothetical structures containing three-fold coordinated carbon appear to give a much better agreement (Figs. 4.4(b), 4.4(c)). Table 4.1 shows that, in general, the position of the main Raman peak correlates well with the relative amount of oxygen double-bonded to carbon, indicating that while the origin of this peak can be traced to the tetrahedral units, its precise frequency, instead, depends strongly on the coordination of their local environment. This also serves

	mix-a	poly-carbonyl	mix-b	amor-phous	β - crist-obalite
Freq.[1] (cm^{-1})	1150	1090	1010-1060	900	820
C3=O (%)	50	50	25	22.9	0
C3-O-C4 (%)	25	0	50	29.2	0
C4-O-C4 (%)	25	0	25	39.6	100
C3-O-C3 (%)	0	50	0	8.3	0

Table 4.1: Dependence of the main (non-carbonylic) Raman peak on the oxygen coordination inside the hypothetical samples. C3 and C4 stand for 3- and 4-fold coordinated carbon sites respectively. Pressure of the samples is 60 GPa.

to justify the small frequency difference observed between the most intense band of carbonia (interpolated arrows in Figure 4.4(a)) and the amorphous shoulder seen in the spectra of phase VI. Similar dependence extends to the frequency position of the theoretical IR peaks (not reported), which accounts for the shape variation of the measured IR spectra of carbonia (Fig. 4.3(b)) upon their history and P-T conditions.

Based on our findings, we speculate on the thermodynamics and kinetics of formation of carbonia. Figure 4.6 reports calculated enthalpies for poly-carbonyl and β-cristobalite CO_2 with respect to molecular phase II. Maximum enthalpy differences between these phases are about 1.4 eV/CO_2 at ambient pressure, but drop to 0.4 eV/CO_2 at 20 GPa, indicating that phases with three different carbon coordinations (two-, three- and four-fold coordination) become energetically accessible when extended phases form. Carbonia starts to appear in experiments at around 48 GPa, much higher than the theoretical transition pressure of the molecular phase to β-cristobalite CO_2 but close to the crossing point between the molecular phase and the three-fold coordinated phase (Fig. 4.6). The formation of the crystalline four-fold coordinated phase V is only observed experimentally well within its thermodynamic range of stability [111], which is consistent with a large kinetic barrier. We infer that carbonia is a metastable form of CO_2, reached kinetically from the collapse of the molecular phase and we speculate that states with three-fold coordination are an intermediate, long-lived step along the transformation of CO_2 into thermodynamically stable tetrahedral phases [130]. We also argue that disorder and three-fold coordination may be intimately connected in CO_2. Disorder in silica glass is in fact known to be linked to the flexibility of the tetrahedral SiO_2 network, which permits a large variety of competing configurations and topologies with similar energies. As shown in Ref. [122], CO_2 tetrahedral phases lack such bond flexibility, since

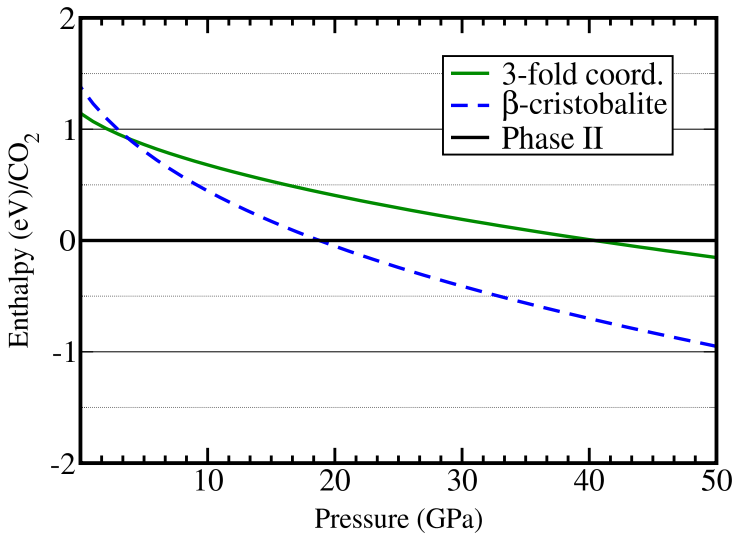

Figure 4.6: Enthalpy curves. Enthalpy difference per CO_2 unit for the β-cristobalite phase (Fig. 4.5(a)) and the three-fold coordinated poly-carbonyl (Fig. 4.5(b)), with respect to the molecular phase II of CO_2.

the reorientation of the internal tetrahedral subunits implies variation of the very stiff C-O-C angle. Three-fold coordination can thus be seen as a mechanism to increase the flexibility of the network and generate a large number of quasi-degenerate configurations, ultimately leading to disorder.

4.1.4 Conclusions

In this section I have shown that the local atomic structure of a-CO_2 is qualitatively different from that of other group IV amorphous oxides, as it contains mixed three- and four-fold coordination of the carbon atoms in similar proportions. Mixed coordination and disorder are made possible by the quasi-degeneracy of three different coordination states for carbon in CO_2 at high pressure. We speculate that CO_2-VI may be the crystalline counterpart of carbonia, but its crystal structure remains to be determined. Because carbonia is likely to be an intermediate, metastable state of the transformation into crystalline superhard phases like phase V, our findings hopefully will help improving strategies to facilitate the synthesis of such phases.

4.2 Catalysis of extended CO_2 phases

4.2.1 Introduction

Given the fact that the amorphous phase obtained from CP-MD in the last section results from a very quick shockwave-like simulation, it is quite probable that its structure is not representing the best possible arrangement that those atoms could have in such a phase in terms of ground-state energy or enthalpy. This consideration remains true even after taking into account the fact that the sample was quenched to ambient pressure and it self-healed its own defects. Still, as we have seen in the previous section, this sample shares many similarities with the properties observed for the real amorphous phase in experiments. More similarities appear if we consider its equation of state (shown in Fig. 4.7) which clearly shows a thermodynamic transition point, when coming from phase II, at pressures above 40 GPa. Such a transition pressure is at least 20 GPa higher than the one calculated for a prototypical tetrahedral silica-like structure (β-cristobalite) shown in the previous section, but coincides fairly well with the observation that the amorphous phase is obtained experimentally at pressures around 48 GPa [13]. Experimental evidence then, seems to indicate that for the molecular CO_2 system it is much easier to overcome the kinetic barrier to arrive into a phase containing (semi-reacted) three-fold coordinated carbon mixed with four-fold, than to a phase completely made out of (fully-reacted) four-fold coordinated carbon atoms, even if the last one is much lower in enthalpy. Given the existing expectations, regarding the applications that would become possible once having such extended phases, it would then be desirable to devise a method that lowers the transition pressures of formation of extended CO_2 phases, and that also permits us to attempt its recovery to ambient conditions, even if it is only in a metastable state.

DFT can also be used as a tool to design stable or metastable new materials based on existing molecular species. In this chapter, the ab-initio MD technique is used to investigate the changes induced by pressure on a CO_2 molecular sample under the presence of an impurity, which will act as a catalytic element to help the transition. With this approach we intend also to tackle the problem of the recoverability of the final phase. The chosen transition-metal impurity, titanium, was selected for the reason that it can form stable compounds with different coordination numbers, and also, because many of these compounds are available commercially. Then, our aim is to simulate the introduction of some molecule containing Ti inside a molecular CO_2 sample in a low-coordination state, and then check if after applying

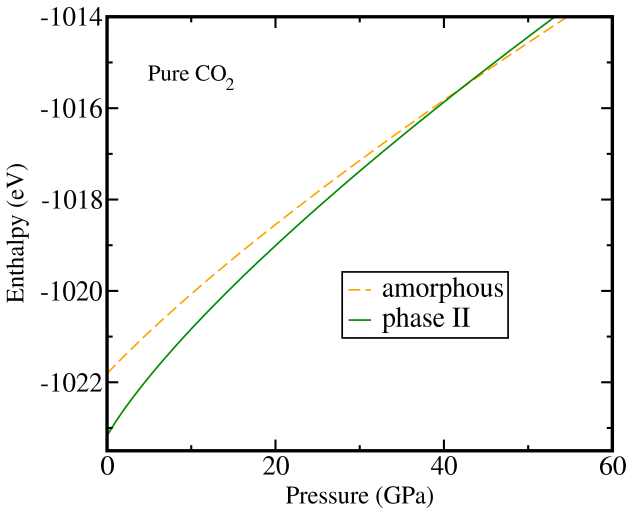

Figure 4.7: Enthalpy difference per CO_2 unit, for the amorphous phase with respect to the molecular phase II.

pressure its coordination changes to a higher value; which would then imply the activation of new bonds on nearby CO_2 molecules and hence the start of a polymerization process (see diagram in Fig. 4.8). Additional to this, titanium could also help avoiding the possible formation of the C_2O_4 rings (Fig. 4.9) predicted theoretically to occur under compression [130], and help stabilizing the new phase, since it is known that transition metals, acting as activation centers in polymerization processes, usually help the continuous growth of polymeric chains.

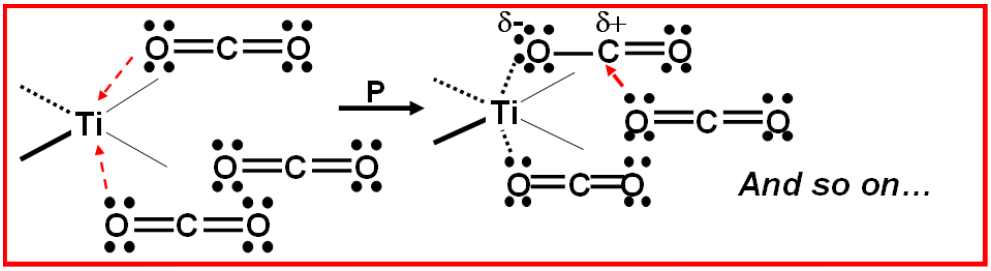

Figure 4.8: Diagram showing the reaction path proposed for the catalysis of the CO_2 polymer.

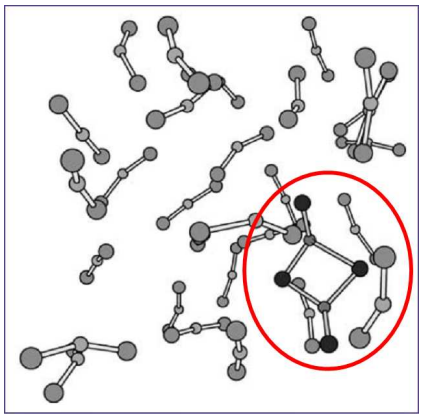

Figure 4.9: Carbonyl units found in Ref. [130] at very high temperatures. Such structures do not contain any dangling bonds and can hinder polymerization.

4.2.2 Methodology

First of all, I will provide some details regarding the way I set the system for the use of the ab-initio MD code (described in section 2.5). A prototypical input file for this code is included in Appendix C. This input tells the code, exactly what our system is and under which conditions we want it to be simulated. The first thing we should notice is that our input file lacks the information related to the set of k-points in which we want the self-consistent minimization to be carried out (see section 2.5) this is so, because our MD code only allows simulations to be performed at the Gamma point $\boldsymbol{k}$=(0,0,0). A second restriction, inherent to our code, is the fact that we are only allowed to use norm-conserving pseudo-potentials; this restriction affects the choice of the cut-off that we are going to use for our plane-wave basis set which, for norm-conserving pseudo-potentials, has to be much higher than the one we usually would require for an ultra-soft pseudo-potential (see: **ecutwfc = 90 Ry**, in the example shown in Appendix C).

The Gamma-only k-point sampling, carries the inconveniece of offering an incomplete sampling of the reciprocal space, especially if the simulation cell is too small. In order to relieve a bit the inaccuracies derived from this problem, one usually simulates a super-cell containing many primitive cells inside it, so that, the volume to be repeated periodically gets larger and the reciprocal lattice is more densely sampled.

In our case a primitive cell for our CO_2 starting phase, phase II, is composed of two molecules with three atoms each. Our first approach was then, to

construct a 3x3x3 super-cell of exclusively carbon dioxide without titanium, which then contained 162 atoms. This number of atoms is considered big for the processing standards of the computers available nowadays, then, we were constrained to the use of the parallel version of the *Quantum Espresso* code on an IBM-sp5 cluster of computers, since the performance of our codes scale very well with the number of processors. A typical run on this computer, delivered one simulation step every 10 seconds while using 64 processors in parallel (these are 8 nodes on a sp5 cluster like the one available at CINECA). In the input example, we can see that every 10 steps (**iprint = 10**) we asked the code to write the positions, velocities, and cell-vectors of our system (among some other relevant quantities) to a set of files, in this way, the sampling rate of the observable quantities in our simulation was one every: 10 steps x 8 a.u./step x 0.024189 fs/a.u $\approx$ 2 femtoseconds, this is a good sampling rate for the movement of the ions in terms of the intrinsic frequencies of our system, that we could need if we wanted to calculate dynamical averages later on. The parameter **dt = 8.0d0**, given in atomic units of time, is the time step that we used for the electronic-dynamics integration, and it was chosen after doing some tests in which we varied its value over a certain range (that typically goes from 1 a.u. up to a maximum of 12 a.u.). In such test, we check if the Lagrangian energy of our system remains conserved during a short simulation ($\sim$ 100 steps). We observed that no major change occurred to the conserved energy even by using a time step dt = 14, but for better accuracy, also given the fact that our simulations were going to be long, we decided for 8 a.u. The behavior of our conserved energy along the longest CP-MD simulation that we did, even if it is just a technical aspect, is shown for the sake of completeness in Figure 4.10. Other input parameters in the &CONTROL section of the input file are briefly described in Appendix C.

Finally, among all the parameters present in the input file, the electronic mass "**emass**" is probably, for Car-Parrinello molecular dynamics simulations, the most subtle one. The electronic mass controls the dynamics of the electronic degrees of freedom in the Lagrangian dynamics, i.e. the dynamics that in CP is associated to the Kohn-Sham electronic wave functions. Such a dynamics should be much faster than the ionic dynamics. However, even if 'fast' means 'accurate', in practice we prefer to have a compromise that allows us to utilize the biggest possible time-step for the integration of the electronic motion, in order to access longer simulation times with the same computational effort. This makes the emass choice an important one, and, as for dt, it has to be tested against the approximate conservation of the fictitious kinetic energy of the Kohn-Sham orbitals' energy. If emass is too big, we will be able to use also large values for dt and cover a lot of time with our simulation,

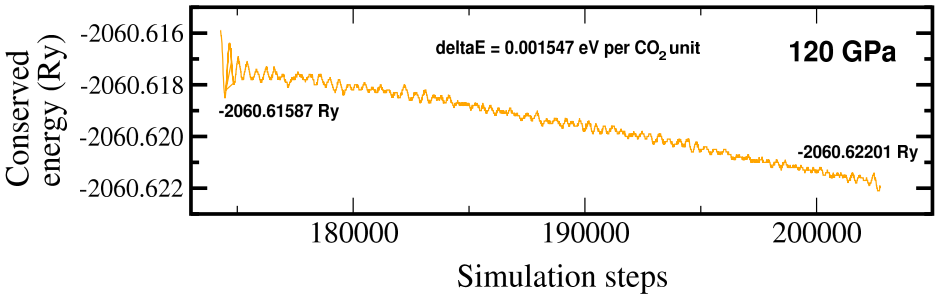

Figure 4.10: Detail showing the behavior of the conserved Lagrangian energy as a function of the simulated time at the pressure for which we did our longest run (120 GPa); the difference in conserved energy between the beginning and the end is lower than any expected contribution to the energy coming from thermal effects, and the run was so long with respect to the others, that we can say that the example shown in the figure was our worst case.

however, by doing this we are making the electronic dynamics comparable in its frequency spectrum to the ionic one. Such similarity of frequencies would allow the transfer of energy from the ions to the electrons and can produce unphysical heating effects on the electrons and cooling of the ions; which reflects on a non-conservation of the ionic-energy, and takes the electronic Kohn-Sham wave functions too far away from their ground-state values. Once we find the highest possible value for dt and emass that guarantee ionic energy conservation and good integration of the electronic degrees of freedom, we can proceed to start our simulation. But still, as reported by Tangney and Scandolo [30], some tuning will be needed at a certain point of the simulation, in order to account for the fact that the sole presence of an electronic mass generates, in most systems, some dragging forces that slow down the ions, that take their motion far from their real dynamics and affect the calculation of observables that have a dependence on correlations with respect to time. The recipe in this case is to rescale the ionic masses to appropriately chosen lower values, restoring in this way the normal dynamic behavior of the ionic motion [30].

4.2.3 Simulation protocol

Some preliminary simulations were performed starting from phase III on a CO_2 sample formed by 48 atoms, with an inserted titanium atom that was

four-fold coordinated to two oxalate units (C_2O_4) constructed by using four neighboring CO_2 molecules, and finally compressing. The decision of using this phase as the starting point, was taken at a time in which it wasn't very clear which phase was the actual starting molecular CO_2 phase in compression experiments at very high pressures. Now we know that phase III, although only metastable, can be easily obtained starting from dry ice above 12 GPa and in a wide range of temperatures, and it is found in the same range of pressures in which the stable phase II is stable (Fig. 4.1). This makes it clear that the two molecular phases II and III can be used experimentally as starting points to form new non-molecular compounds. It was for this reason, that after some frustrating experiences with the more stable phase II, we decided to continue our test simulations in phase III even to higher pressures.

The details on how we did the set-up of the system are completely analogous to the ones that I am describing later for the definitive simulation in the next paragraphs. The importance of this preliminary test, resides in the fact that it shows that the mechanism proposed in Figure 4.8 indeed holds, and that the pressure at which it occurs is much lower than the one needed for polymerizing the same kind of system without an impurity [119]. The original test was done just up to a pressure of 24 GPa where second neighbors clearly started to join the polymer. But, as I mentioned before, recently it was decided to extend this study up to a completely polymerized stage, due to difficulties that we encountered starting from phase II, the evolution of such a complete polymerization process is shown for reference in Figure 4.11 and makes evident that much lower temperatures and pressures are needed in order to achieve the full polymerized state, when starting from phase III. The final conclusion being that we obtained and recovered to ambient conditions, a polymer consisting of 50% of three-fold coordinated carbon atoms (carbonylic or semi-reacted sites) and 50% of four-fold coordinated tetrahedral (fully reacted carbon) sites, with an energy difference between its molecular-starting and quenched-final conditions of the order of 0.5 eV per CO_2 molecule. Such a short, preliminary run, supported our conjecture that the polymerization can indeed be catalyzed by the impurity, and led us to setting up a more realistic simulation with a more careful choice of the parameters.

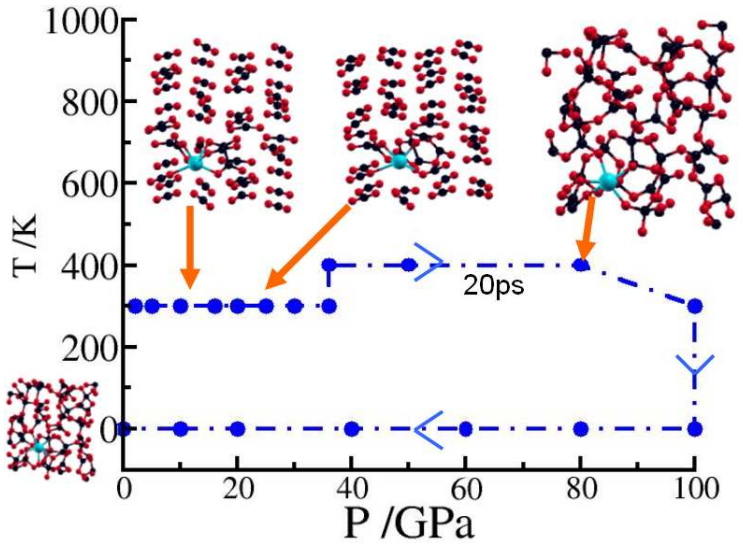

Figure 4.11: Compression and recovery P-T path for CO_2, starting from the molecular phase III.

Before starting our main simulation, we had a look in the literature available at the time (early 2004) in order to get an idea about which one could be the most probable starting molecular phase for a real CO_2 polymerization. There was a confusion around this regarding the fact that, at the pressures of interest for such experiments, the only stable phase was the molecular phase II while it was also very clear that a second molecular phase (phase III) was also commonly used in experiments and present at those pressure conditions, then, there was no agreement on the exact place to locate the kinetic transition boundary between the two. We then concluded that it was much safer to start our simulation from the phase II of CO_2, since it was the only one to be completely stable and the most likely to be attainable at any range of initial conditions in real experiments. A sample of pure CO_2 was created in this phase, and its internal coordinates together with the shape of the cell were relaxed in a volume equal to the one that this phase CO_2 should have at zero pressure. From the observed mismatch between the internal pressure thus obtained and the one we knew from the EOS for this phase at that volume (i.e. 0 GPa) we were able to establish the magnitude of the so-called Pulay stress [137]. In our work, the Pulay stress was 4.75 GPa. An alternative method for calculating the Pulay stress, which we didn't use here, consists of repeating the calculation for the super-cell with a much higher energy cut-off and calculating the difference between the two stresses thus obtained, that would clarify the dependence of the pressure inside the

system with the cut-off.

After relaxing the ionic and cell degrees of freedom for our 162-atom super-cell, we proceeded with the insertion of one $Ti(C_2O_4)_2$ (titanium di-oxalate) molecule (Fig. 4.12). This, was done by extracting four neighboring CO_2 molecules from the phase II super-cell, letting a hole where our $Ti(C_2O_4)_2$ molecule can fit, then the molecule was inserted and its atomic positions allowed to relax, while keeping the CO_2 matrix frozen. After having done this, we let both the inserted molecule and the CO_2 phase II, to relax until all the ions inside the super-cell reached their equilibrium positions at T = 0 K. The next step is to mimic thermal disorder by displacing randomly the ions by very small distances from their equilibrium positions from which, by MD and using the so-called thermostats, we will reach the desired conditions of pressure and temperature.

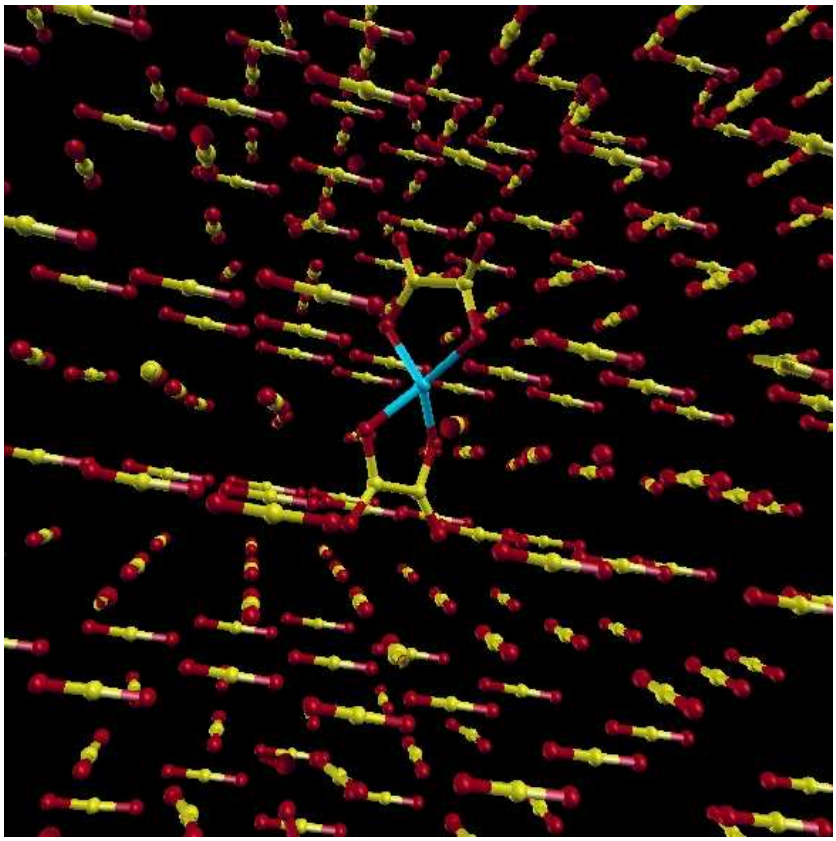

Figure 4.12: Original set-up, showing a single $Ti(C_2O_4)_2$ molecule embedded in a bulk sample of molecular CO_2 in phase II.

4.2.4 Results and discussion

The first P-T condition that we targeted corresponded to ambient pressure and temperature. After having done this, we gave the system 2 picoseconds to become stable while steadily increasing the pressure until we got a very well thermalized system at 4 GPa. Then we proceeded to rescale the ionic masses as described in Ref. [30] in order to account for the dragging due to the electrons on the atoms that was mentioned before. What we did after that, has been schematized in Figure 4.13. First of all, we tried to repeat the P-T conditions used for the phase III test, by following those conditions we arrived at the point (A) in Figure 4.13 where again we noticed that at pressures below 10 GPa, the reaction predicted by the left part of Figure 4.8 also occurred for phase II (see Fig. 4.14).

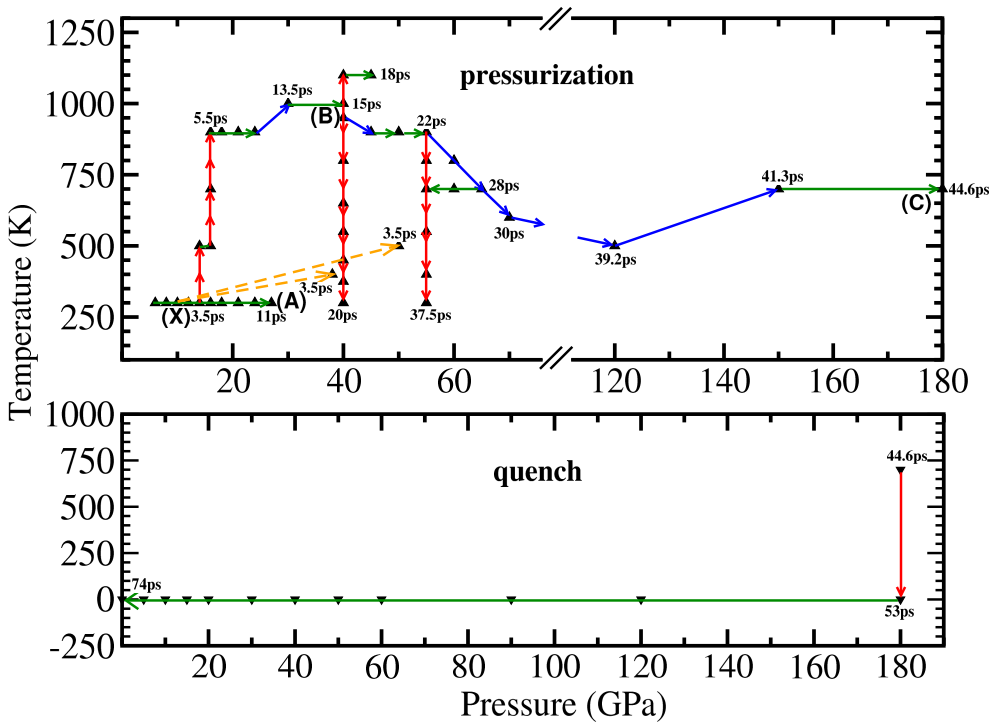

Figure 4.13: P-T path for compression and quenching of CO_2+Ti starting from phase II. Arrows: red are isobaric simulations, green represent isotherms, dashed-orange are shock-wave simulations and blue represent simultaneous P-T changes.

By going to higher pressures while maintaining a constant temperature we arrived at the (A) point (24 GPa, 300 K) for which, in the case of phase

III, the second nearest neighbors of the Ti were already starting to join the polymer, but for phase II nothing was happening. We therefore decided to perform a fast shock-wave compression from the (X) point in which the first step of the polymerization reaction was fulfilled (8 GPa at 300 K, Fig. 4.14) bringing it to 38 GPa and 400 K in 3.5 picoseconds. What we obtained from this trial was a sample in which the di-oxalate plus the two neighboring molecules already linked in (A), were rearranged in a way that didn't let any dangling bond on the carbon atoms to continue polymerizing, while the rest of the system continued to be molecular. This is a good place to remark that, in absolutely none of our calculations, we observed the predicted isolated carbonyl units predicted by Ref. [130], which confirms that the temperatures needed to arrive to those configurations within the time scales of a typical ab-initio MD run, are very large. The fact of not being able to see any independent, parallel initiation of a polymerization process not linked to our transition-metal impurity, also means that under the conditions of pressure that we simulated a pure CO_2 sample would remain most probably in its molecular state. We finally corroborated this assumption by simulating a system of the same size without titanium up to 55 GPa and 900 K, and found that the system remains molecular.

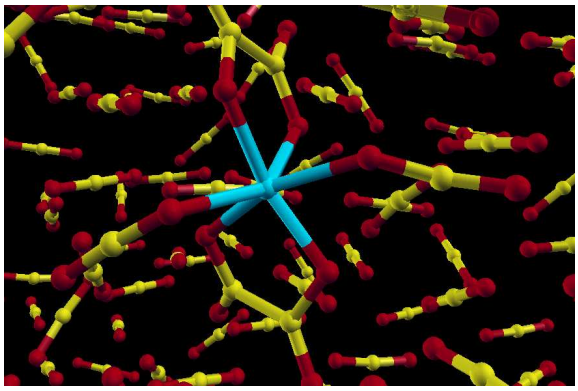

Figure 4.14: First step in the polymerization process, observed at 8 GPa and 400 K. It shows that the predicted change in the coordination of the Ti atom indeed occurs, and this leads to the creation of dangling bonds in the attached CO_2 molecules.

Simultaneously, after reaching point (A) it was decided to go back to a lower pressure (14 GPa) and start heating the system slowly to allow more time for the normal reorientation of the molecules. Here, after having reached a temperature of 1000 K the sample was again compressed up to 24 GPa but still no polymerization took place. The conclusion then was, that phase II

is much more difficult to reorient than phase III and this observation may imply that phase II is, indeed, much more stable (also due to kinetic barriers) than phase III.

Then, it was again decided to continue heating and compressing phase II until we arrived at the (B) point (40 GPa, 400 K) where we observed the 2^{nd} neighbor inclusion into the polymer-seed, that was also observed but at half this pressure when starting from phase III. At this point, it was not clear which kind of role the temperature was playing, so, we branched our simulation towards higher and lower temperatures, at the same pressure, without observing any substantial change apart from the fact that, due probably to a spurious artifact introduced by the Nosé thermostat when we increased the temperature from 900 K to 1000 K, the polymer seed dissolved and went back to a previous stage at those higher temperatures. Then, we continued our simulation towards higher pressures while decreasing a little the temperature until, starting at 55 GPa, a noticeable increase in the size of the polymer was observed. At this pressure we also quenched the sample to 300 K and noticed no structural changes. Here again we decided to perform a shock-wave test to reach these conditions starting from the same sample already discussed at 8 GPa and 300 K. We found that the CO_2 units originally attached at point (X) to the $Ti(C_2O_4)_2$ molecule and a few more this time, decided to form a stable configuration with no dangling bonds available, the rest of the sample was still molecular.

The behavior of the enthalpy for simulations going up to the (C) point (180 GPa, 700 K) is shown in Figure 4.15. We observed, that a bit below 80 GPa the molecular character of the sample was drastically changed, as can be seen from corresponding changes in enthalpy and the detailed study of the carbon coordination shown in Figure 4.16.

In Figure 4.16, we can see that to each strong change in coordinations (left) corresponds a noticeable decrease in the enthalpy (right), which in the first case can be related to a noticeable collapse in the volume. Here we distinguish two regimes, one that starts at 55 GPa and ends around 80 GPa in which the polymerization process helps the reduction of the total volume of the cell by absorbing the isolated carbon molecules, leading to an evident change in enthalpy; and other regime, going from 90 up to 120 GPa in which the system becomes more compact, but this time by preferring four-fold coordinated carbon atoms at the expense of the three-fold coordinated ones, which leads towards a phase that is predominantly tetrahedral. In the range from 55 to 80 GPa the volume reduction was of the order of 20%, while in the range

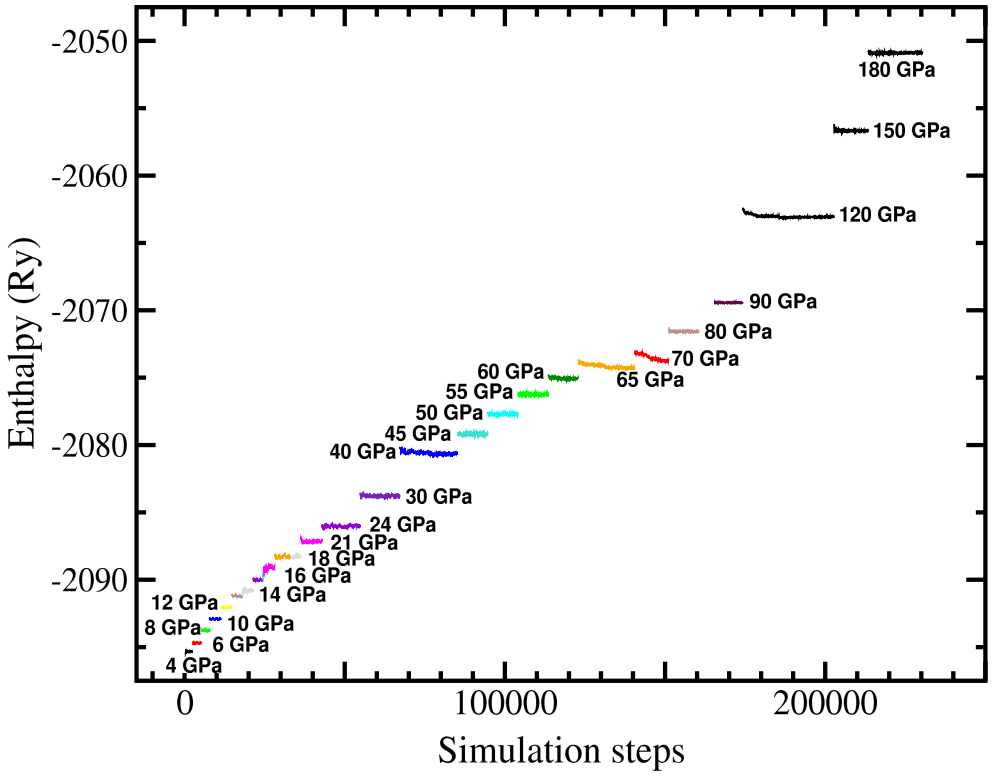

Figure 4.15: Enthalpy curves along the main simulated path. When chemical reactions take place there is a substantial reduction in the total energy and volume occupied by the system and the enthalpy decreases.

from 90 to 120 GPa the reduction was only of the order of 8.5% but there was a major gain in terms of energy. The volume changes reported above also include the normal decrease in volume due to compression itself.

The three-fold vs. four-fold coordination ratio found in our simulations of Ti+CO_2 equals that for carbonia (40% and 60% respectively) at 110 GPa and 600 K when starting from phase II, and at 80 GPa and 400 K when starting from phase III. However, in order to polymerize a pure CO_2 sample up to such a coordination ratio, the authors in Ref. [119] reported as formation conditions, pressures above 100 GPa at 2000 K starting from phase III. Hence, after having demonstrated in the previous chapter that the phase found by Ref. [119] in simulations, is indeed the one that has been observed in experiments starting from 48 GPa, we can now speculate that the onset of our polymeric transition, predicted to be around 60 GPa starting from phase II and below 40 GPa starting from phase III, may be highly overestimated as well. Incidentally, as it has been already suggested here, and also based on observations from recent studies made on pure CO_2 by our group in collaboration with R. Martonak and E. Tosatti using meta-dynamics [138], on the time scales of a typical CP-MD run it is much easier to observe transitions towards extended phases when we depart from phase III than when we start from phase II, meaning that the transition from phase II involves a larger kinetic barrier.

In previous sections of this work we have shown also that the energy difference per CO_2 molecule between the molecular phase II and mixed or tetrahedral extended phases is not lower than 1.2 eV per molecule (see Fig. 4.7), while the same energy difference if we include titanium becomes 0.68 eV with respect to the molecular phase II and 0.5 eV with respect to phase III, this points to a relevant increase of the chances of making this new material recoverable.

Between 50 and 80 GPa, the polymer grows freely (limited only by the difficulty, inherent to our short-time ab-initio dynamics, to overcome even small kinetic barriers linked to slow translational or rotational modes) until some branches start touching the polymer's images belonging to nearby cells. After this occurs, it gets harder and harder to make the molecules that are not yet attached to follow the trend. An extreme example of this problem is what we actually saw during our simulations when at 80 GPa, two molecules remained still isolated (Fig. 4.17) inside one of the cavities that are commonly found in many places of this structure, as well as in carbonia, and that may arrive to have sizes of 6 Å in diameter. This doesn't affect the overall result, that the real full polymerization takes place at 60 GPa, however, in

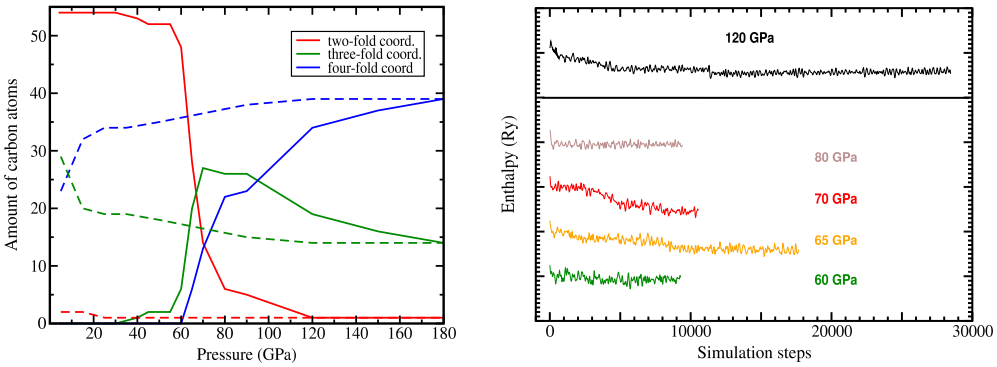

Figure 4.16: Left: Trend of the carbon coordination vs. pressure. The total number of carbon atoms is 54. Dashed lines indicate the behavior during quenching. Right: Detail of the enthalpy behavior in the portions of the simulation where the structure changes more drastically

order to obtain a fully-polymerized sample that later can be quenched and then used to compare its energy against its molecular counterpart, we need to overcome this problem. This can be done in principle by increasing the pressure. However, even by increasing P up to 120 GPa we noticed that in the vicinity of our isolated molecules there were no clearly exposed dangling bonds coming from the polymer. The observation that this was not so easy to achieve also renders clear the idea that in general, it is easy to form C-O single bonds in the initial stages of the polymerization, but once the polymer starts to grow, transformation of the residual C=O double bonds requires large concerted rearrangements that cannot take place in the ab initio MD time scales. The final result at 120 GPa, was a polymer that still looked like the original, but with the previously isolated CO_2 molecules now arranged either in a "Polymer—O—C—O—Polymer" or in a "Polymer—O—C—O" fashion, which then leaves two and one dangling bonds in the carbon atoms respectively, and makes these units look like a linear CO_2 molecule. Even by going up to 180 GPa, it was by no means possible to eliminate completely from our sample the units containing dangling bonds, and one of them remained looking like a molecular CO_2 unit until the end, as can be seen from the counting of coordinations in Figure 4.16.

We still have that even with such an undesirable final situation, mostly related to the limitations intrinsic to our technique, we got, after quenching to zero pressure, a difference in energy of only 0.65 eV per molecule with respect to the starting configuration, which is remarkable because it is one half the energy difference between pure CO_2 in phase II and the non-molecular amor-

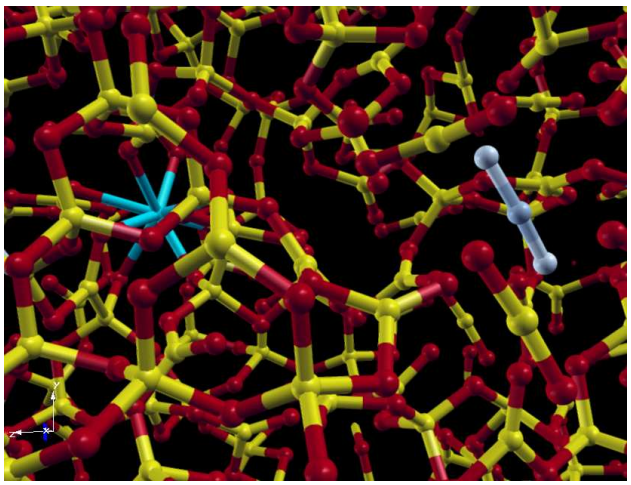

Figure 4.17: The amorphous sample obtained in our simulations, offers a substantial reduction in volume with respect to any molecular counterpart. However, it is clear from this picture that the sample is permeated by large holes that, in our very small simulation box, act as cavities where single molecules remain stored without suffering to much the effects due to the external pressure.

phous phase (it can be seen clearly in Figure 4.7). More accurate studies using larger samples, can then only change our results towards better and more promising energy differences.

4.2.5 Conclusions

Our simulations show that, during compression, CO_2 molecules that are located in the polymeric path, initiated from the Ti atom, help the growing of the polymeric phase by easily linking to the polymer in a process that starts at pressures around 60 GPa in our MD simulations. In the other hand, CO_2 molecules which are not in the vicinity of the titanium-dioxalate molecule or of any dangling bond generated by this molecule on neighboring CO_2 molecules, do not polymerize under the application of pressure. The fact that when titanium is present the energy of the extended recovered phase is closer to the molecular staring phase than in the pure system, implies that the material obtained by this process has better chances of being recovered to ambient conditions. The study also shows that, under the reasonable assumption that the transition pressures measured in our simulations, are overestimated with respect to the experimental ones, it can be concluded that the pressures required experimentally in order to obtain a CO_2 polymer

catalyzed by a transition-metal seed, are much lower than the pressures at which current extended forms of CO_2 are obtained, and that in any case, it is more convenient to start from phase III as the precursor molecular phase. The increase in the amount of three-fold coordinated carbon units with decreasing pressure during quenching, suggests that the recovered material may not be as hard as expected. However, such a material could still bear outstanding characteristics useful for technological applications. For example, in this work numerous empty spaces as large as 6 Å in diameter, inside the recovered amorphous structure with and without titanium, have been identified. This material then could be used to store small molecules, opening possibilities to new applications such as hydrogen storage, which then adds to the many possibilities already suggested in previous years for these materials.

Chapter 5

Conclusions

In this work ab-initio calculations have been used in close interplay with experimental measurements, to explain and predict properties of new materials that can be synthesized at high pressures. It has been shown, that computer simulations with ab-initio accuracy are a perfect tool for testing new structures, and for measuring properties on them that can be directly compared to experiments.

Following these ideas, we were able to solve the crystal structure of the novel PtN_2 and OsN_2 compounds. Following our findings now it is accepted and understood by the high-pressure community, that these compounds together with IrN_2 and others that continue to appear, are part of a new family of materials, which have the common property of containing covalently bonded nitrogen forming single-bonded dinitrogen units in their interior. Such a common feature, suggested the possibility of having phonon-mediated superconductivity in metallic materials of this family, such as OsN_2. In fact, the superconducting T_C of OsN_2 was calculated and it was observed that a sizable contribution to the electron-phonon interaction term λ comes from high-frequency N-N modes.

We also calculated that at the conditions where the new TM-nitride phases are synthesized, the entropic contribution coming from the liquid N_2 environment cannot counterbalance the difference in energy between the new phases and their constituents, and it is for this reason that the reaction takes place at pressures above the calculated enthalpy crossing between the different phases. This observation opens the possibility to find new metastable phases that, due to kinetic barriers, cannot be reached directly from their parent metals and liquid N_2 at low pressures but that could be accessed through the quenching of the high-pressure dinitride phases.

In a completely different direction, but following the same spirit of the studies on nitrogen, the high-pressure phases of the CO_2 molecule have also been carried on in collaboration with experimentalists. The aim in this case was to perform the characterization of existing and prediction of new CO_2 extended phases. Non-molecular CO_2, in contrast with what is observed for the TM-nitrides, hasn't yet been recovered to ambient conditions from any of the known high-pressure extended phases.

The first thing we noticed during our studies on this subject, is that non-molecular CO_2 phases don not behave the same as silica and germania. Indeed, they are not only much more difficult to obtain, but also differ strongly from the point of view of their local coordination with respect to the situation observed in polymorphs of SiO_2. Amorphous carbonia for example, contains three-fold coordinated carbon atoms (carbonyls) that appear earlier during the transition to the amorphous than any four-fold coordinated (tetrahedral) site, and remain still present inside the sample as a metastable form in sizable amounts even after tetrahedral sites have been formed. Enthalpy calculations show that CO_2 in four-fold coordination for the carbons, is more stable than structures containing two- or three-fold coordination at pressures above 20 GPa. Then, a huge kinetic barrier appears to be the explanation to the frustrated mixed-state that is observed in carbonia.

By doping molecular CO_2 with titanium, we observed a lowering in the kinetic barrier of the transition towards non-molecular phases. Moreover, after recovery the CO_2 polymeric samples containing titanium, they exhibited a lower energy difference with respect to the starting point, than the energy difference obtained for the case of pure CO_2.

Finally, based on our results I have provided at the end of each section of my thesis work some hints that regard the perspectives for the future that this work has opened which, among others, include: the possibility of synthesizing new superhard materials containing dinitrogen, new high-T_C BCS superconductors from metallic nitrides of TM alloys, and materials that can be used as alternative to clathrates for hydrogen storage, all of this can and still has, to be checked experimentally. It is due to conclusions like the ones reported along this chapter, that I can now see clearly the importance of continuing such a fruitful interplay between theory and experiment in high pressure research which, I hope, will continue to be present and in an increasingly strong way, in the years to come.

Appendix A

Some useful conversion tables

PRESSURE:

╲ TO / FROM ╲	GPa	bar	atm	a.u.
GPa	1	$1x10^{4}$	9869.2	$34.014x10^{-6}$
bar	$1x10^{-4}$	1	0.9872	$3.4014x10^{-9}$
atm	$1.013x10^{-4}$	1.013	1	$3.45x10^{-9}$
a.u.	29400	$2.94x10^{8}$	$2.90x10^{8}$	1

LENGTH:

╲ TO / FROM ╲	meters	Å	a.u.
meters	1	$1x10^{10}$	$18.9x10^{9}$
Å	$1x10^{-10}$	1	1.89
a.u.	$5.29x10^{-11}$	0.529	1

FREQUENCY:

╲ TO / FROM ╲	THz	cm^{-1}
THz	1	33.36
cm^{-1}	0.02998	1

ENERGY:

╲ TO FROM ╲	Ry	eV	a.u.
Ry	1	13.606	0.5
eV	0.0735	1	0.03675
a.u.	2	27.2114	1

1 THz x h = 4.13565 meV
k_B x 300 K = 25.852 meV

Appendix B

Pseudo-potential tests on platinum and nitrogen

In this appendix, I will explain how we tested the platinum and nitrogen pseudo-potentials by simulating the platinum crystal and the nitrogen N_2 molecule separately. This should allow us to see if the pseudo-potentials downloaded from Internet are working fine, by comparing some calculated dynamical properties of these two systems with the ones given in the literature. This step is also important because it will give us an idea about the ground-state energies for these elements when they are isolated. In Chapter 3, we used these results to determine which of the various proposed structures for the platinum Nitride is more effective in lowering the energy of the entire system.

From some exploratory earlier runs of the *Quantum Espresso* program — for platinum-nitride in the zinc-blende configuration — we decided to fix, in all the input files used in this test, the cut-off energy to ecut = 25 Ry, and the k-point mesh to 10 x 10 x 10. These values are the optimum ones because from the mentioned runs we concluded that increasing them would represent an increase in the computational effort without manifest improvements in the accuracy (see section 2.5 for details on what they mean).

B.1 Platinum crystal

Platinum conforms an *fcc* crystalline structure[4] with a lattice constant $a_0 = 3.92$Å at ambient pressure, this characteristic is shown in the Fig. B.1 where

[4]Predicted to remain stable over a wide pressure range [131, 132].

all the platinum atoms in the conventional unit cell can be seen. However, this representation would be a bit dense and confusing if we were trying to visualize the possible positions for some nitrogen atoms inside this structure (as we will do in the next chapter); so, we will make use of the primitive unit cell representation (Fig. B.2), in order to avoid such difficulties.

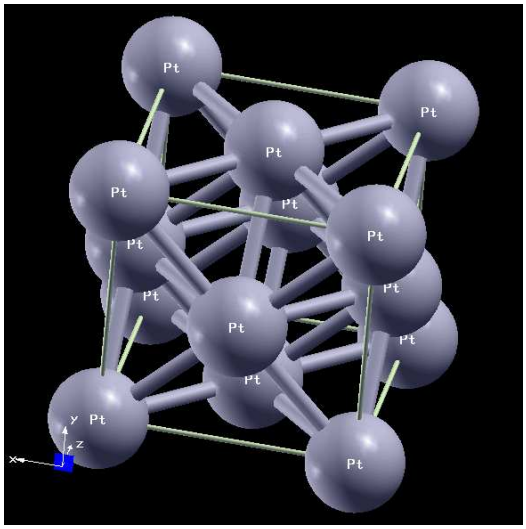

Figure B.1: Platinum's conventional cell.

From our calculations we extracted the results shown in Table B.1 which are compared with experimental or previously simulated data from refs. [133, 134, 135, 136]. This Table, from our point of view, shows a good agreement because even if there are some differences, these are still within the expected accuracy of the method.

As mentioned before, one important parameter we are interested in, is the internal energy of the system, that for platinum turned out to be -52.695 Ry (or -716.96 eV). Now we will proceed similarly with the nitrogen molecule.

B.2 Nitrogen molecule

Nitrogen at ambient conditions conforms a diatomic gas, N_2, which is very stable and it is very difficult to break in order to make compounds with

[5]For further comparisons it is relevant to put also the calculated values in cm^{-1} units: 129.6 and 193.6 cm^{-1} respectively.

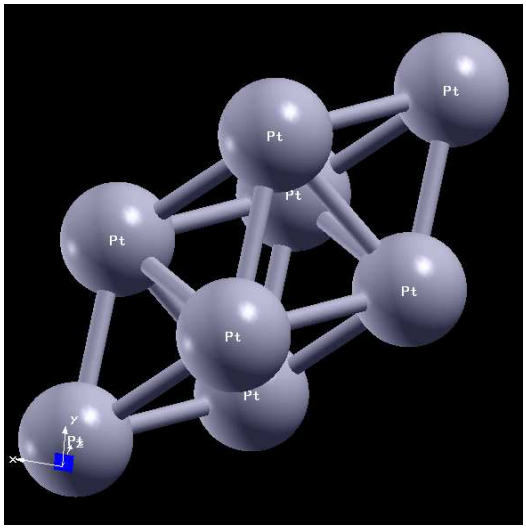

Figure B.2: Platinum's primitive cell.

Quantity	*This work*	Other source
Lattice spacing (Å)	3.910	3.9217
Bulk modulus	301.8	278
First bulk's derivative with respect to pressure.	5.14	5.61
Phonon frequency[5] at X	3.88THz* - 5.80THz	3.85THz* - 5.7THz

Table B.1: Test for *fcc* platinum. *(*) degenerated phonon mode.*

other elements. It is for this reason that it is commonly used as neutral, environmental medium in many experimental setups.

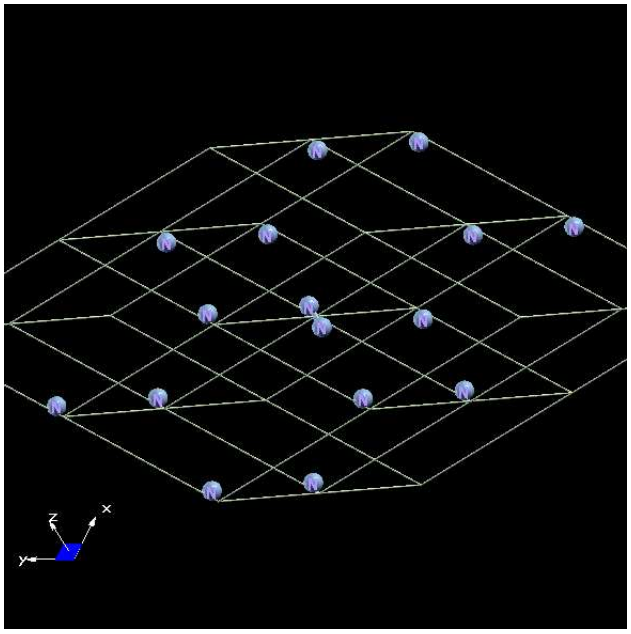

Figure B.3: N_2 in the gas state modeled as a periodic crystal, done in order to allow our plane-waves approach.

We would like to model the N_2 molecules in their gaseous state, since this is the way in which it is used as pressure transmission media in experiments. However, as mentioned in *chapter 2*, our plane-waves approach can be accurately used only when considering an infinite crystal. For that reason we have to cheat a bit by shaping our molecular gas into a crystal (see Fig. B.3) or if you prefer; by giving to our crystal enough size to make our low density of particles act as if they were in a gas. So, we had to form a basis for the crystal by putting each N-N pair with a small distance between them and very far from the other pairs, in our case this was obtained just by defining our crystalline lattice spacing to be equal to 20 Å) and we also decided to use here an *fcc* lattice in order to make our system as much homogeneous and isotropic in average, as possible. After doing this, we can say that every N_2 molecule was almost independent from its neighbors (actually: from its images, in this case).

Then we proceeded with a relaxation process in which the system was supposed to go to an equilibrium position and from which we extracted finally

Quantity	*This work*	Other source[6]
Atomic separation	1.105 Å	1.104 Å
Vibrational frequency	Not available.	2738.8 cm^{-1}

Table B.2: Test with only molecular nitrogen.

the inter-atomic separation for this molecule. In Table B.2 some characteristics of this molecule are shown. The small inter-atomic separation and the very high vibrational frequency, are a proof of the stiffness of the bond which is a well known result also from experiments. As for platinum, here we also obtained the binding energy of the N_2 molecule which is -39.657 Ry (or -539.57 eV).

After these two tests, we concluded that the local density approach and the pseudo-potentials used seemed to be working fine. Then we proceeded using this technique on the platinum-nitride compound, hoping that at least we will be able to access the main features of its possible structures. For that purpose, we will have to keep in mind the energies just obtained and more specifically the following two combinations:

$$Pt + \frac{1}{2}N_2 \longmapsto -72.524Ry \ ,$$

and

$$Pt + N_2 \longmapsto -92.3520Ry \ .$$

[6]These ones are values obtained by MNDO, which can be found at *http://www.cachesoftware.com/mopac/Mopac2002manual/node619.html*

Appendix C

Input-file example for fpmd.x

```
&CONTROL
TITLE = 'CO2_II+Ti',
calculation = 'vc-relax',
restart_mode = 'restart',
ndr = 66,
ndw = 50,
nstep = 40000,
iprint = 10,
isave = 500,
tstress = .TRUE.,
tprnfor = .TRUE.,
dt = 8.0d0,
max_seconds = 85000,
forc_conv_thr = 5.0d-4,
etot_conv_thr = 1.0d-7,
ekin_conv_thr = 1.0d-6,
outdir = './',
PREFIX = 'CO2_Ti'
/
&SYSTEM
ibrav = 14,
celldm(1) = 8.032068251343,
celldm(2) = 1.000000000000,
celldm(3) = 1.100000000000,
celldm(4) = 0.0d0,
celldm(5) = 0.0d0,
celldm(6) = 0.0d0,
nat = 7,
ntyp = 3,
nbnd = 22,
```

```
nelec = 44,
ecutwfc = 90.0d0,
xc_type = 'PBE'
/
&ELECTRONS
emass = 350.0d0,
emass_cutoff = 2.5d0,
orthogonalization = 'ortho',
electron_dynamics = 'verlet',
electron_temperature = 'not_controlled'
/
&IONS
ion_dynamics = 'verlet',
ion_temperature = 'nose',
tempw = 500,
fnosep = 40
/
&CELL
cell_dynamics = 'pr',
press = 115.25d0
/
ATOMIC_SPECIES
Ti 39.8523d0 Ti_MT_PBE_SEMIfpmd.UPF
C 10.2506d0 C_MT_PBE.UPF
O 10.7300d0 O_MT_PBE.UPF
ATOMIC_POSITIONS (bohr)
Ti 0.00108088 0.000294366 -2.00214744 1 1 1
C -0.000666802 1.48782 3.07586 1 1 1
C -0.00067318 -1.48835 3.07558 1 1 1
O 0.000592676 2.41494 0.59712 1 1 1
O 0.000592142 -2.41484 0.59658 1 1 1
O 2.42268 0.000132846 -4.599 1 1 1
O -2.4221 0.000112256 -4.5977 1 1 1
```

Some parameters not yet explained in the &CONTROL and &SYSTEM sections of the input file, include:

TITLE: Just the title; **calculation:** the kind of calculation that we are going to perform; **restart_mode:** you can define here if it the calculation starts 'from_scratch' or if is a 'restart'; **ndr:** number that identifies the file from which we are going to read the wave functions (only has sense if " restart_mode = 'restart' "); **ndw:** number that identifies the file to which we are going to write the information necessary for future restarts; **nstep:** number of simulation steps that we want to perform (total steps, not iprint steps); **isave:** here we declare how

often (measured on number of steps) we are going to save information to the file identified by ndw; saving very often also means a considerable slow down of the code's performance; **tstress & tprnfor:** are used for defining if we want the stress and forces to be printed to the output file; **max_seconds:** this tells the program for how long (in real wall-clock time) we want our code to run before it is stopped in a soft way (soft way means: saving everything) it is useful when our maximum computer time is limited by a queue system, normal in parallel environments; the entries finishing with **conv_thr** are thresholds that we define particularly in the minimization process that tell the program, how accurate we want our forces and energies coming from DFT to be; **outdir:** is the working directory were the pseudo-potentials and restart files can be found; **PREFIX:** is used to define the initial part of the name for all files containing statistical information regarding our system.

The only two entries from the &SYSTEM section of the input that haven't been commented so far are: **nbnd** and **nelec**. The second defines the first, since nbnd is just the number of bands necessary to place our valence electrons, and nelec is precisely the total number of valence electrons present on our system as stated inside the pseudo-potential files. for our particular case, the pseudo-potentials were elaborated letting 4 valence electrons for carbon, 6 for oxygen and 12 for titanium.

Bibliography

[1] R. M. Hazen, *The Diamond Makers*, Cambridge, University Press, (1999)

[2] R.J. Hemley and N.W. Ashcroft, *Physics Today* **August**, 26 (1998)

[3] V. V. Struzhkin, M. I. Eremets, W. Gan, H. Mao, and R. J. Hemley, *Science* **298**, 1213 (2002) K. Shimizu, H. Ishikawa, D. Takao, T. Yagi, and K. Amaya, *Nature* **419**, 597 (2002)

[4] V. V. Brazhkin, A. G. Lyapin, and R. J. Hemley, *Phil. Mag. A* **82**, 231 (2002)

[5] C. Cavazzoni, G. L. Chiarotti, S. Scandolo, E. Tosatti, M. Bernasconi, and M. Parrinello, *Science* **283**, 44 (1999)

[6] V. Iota, C. S. Yoo, H. Cynn, *Science* **283**, 1510 (1999)

[7] A. Chatterjee, A. K. Singh, and A.Jayaraman, *Phys. Rev. B* **6**, 2285 (1972)

[8] A. Svane, G. Santi, Z. Szotek, W. M. Ternmerman, P. Strange, M. Horne, G. Vaitheeswaran, V. Kandiana, L. Petit, and H Winter, *Phys. Stat. Sol. B - BASIC RESEARCH* **241** (14), 3185 (2004)

[9] S. Scandolo, M. Bernasconi, G.L. Chiarotti, P. Focher, E. Tosatti, *Phys. Rev. Lett.* **74**, 4015 (1995)

[10] E. Gregoryanz, C. Sanloup, M. Somayazulu, J. Badro, G. Fiquet, H.-k. Mao, and R. J. Hemley, *Nat. Mater.* **3**, 294 (2004)

[11] A. F. Young, C. Sanloup, E. Gregoryanz, S. Scandolo, R. J. Hemley, and H.-k. Mao, *Phys. Rev. Lett.* **96**, 155501 (2006)

[12] V. Iota, C.-S. Yoo, and H. Cynn, *Science* **283**, 1510 (1999)

[13] M. Santoro *et al.*, *Nature* **441**, 857 (2006)

[14] V. Iota *et al.*, *Nat. Mater.* **6**, 34 (2007)

[15] R. M. Martin, *Electronic structure: basic theory and practical methods*, Cambridge, University Press, (2004)

[16] , M.P. Allen & D.J. Tildesley *Computer simulation of liquids*, Oxford Clarendon Press, (1987)

[17] S. Baroni, S. de Gironcoli, A. Dal Corso, and P. Giannozzi, *Rev. Mod. Phys.* **73**, 515 (2001)

[18] M. C. Payne, M. P. Teter, D. C. Allan, T. A. Arias, and J. D. Joannopoulos, *Revs. Mod. Phys.* **64**, 1045 (1992)

[19] M. Born and J. R. Oppenheimer, *Ann. Phys.*, Leipzig, **84**, 457 (1927)

[20] P. Hohenberg and W. Kohn, *Phys. Rev.*, **136**, B864 (1964)

[21] N. D. Mermin, *Phys. Rev.*, **137**, A1441 (1965)

[22] W. Kohn and L. J. Sham, *Phys. Rev.*, **140**, A1133 (1965)

[23] R. G Parr and W. Yang, *Density Functional Theory of Atoms and Molecules*, Oxford University Press, N.Y, (1989)

[24] R. M. Dreizler and E. K. U. Gross, *Density Functional Theory*, Springer, Berlin, (1990)

[25] D. M. Ceperley and B. J. Alder, *Phys. Rev. Lett.* **45**, 566 (1980)

[26] J. P. Perdew and A. Zunger, *Phys. Rev. B* **23**, 5048 (1981)

[27] D. C. Langreth and M.J. Mehl, *Phys. Rev. B* **28**, 1809 (1983)

[28] D. R. Hamann, *Phys. Rev. Lett.* **76**, 660 (1996)

[29] S. Scandolo, *Proc. of the International School of Physics "E. Fermi" on High Pressure Phenomena*, Course CXLVII, IOS, Amsterdam, 195 (2002)

[30] P. Tangney and S. Scandolo, *J. Chem. Phys.* **116**, 14 (2002)

[31] R. Car and M. Parrinello, *Phys. Rev. Lett.* **55**, 2471 (1985)

[32] D. K. Remler and P. A. Madden, *Mol. Phys.* **70**, 921 (1990)

[33] R. Car and M. Parrinello, *Simple Molecular systems at Very High Density*, Plenum Press, New York, 455 (1989)

[34] M. Parrinello and A. Rahman, *Phys. Rev. Lett.* **45**, 1196 (1980)

[35] M. Parrinello and A. Rahman, *J. Appl. Phys.* **52**, 7182 (1981)

[36] H. C. Andersen, *J. Chem. Phys.* **72**, 2384 (1980)

[37] P. Focher, G.L. Chiarotti, M. Bernasconi, E. Tosatti and M. Parrinello, *Europhys. Lett.* **36**, 345 (1994)

[38] P. Focher and G.L. Chiarotti, *Progress in Computational Physics of Matter*, World Scientific, Singapore, 1 (1995)

[39] M. Bernasconi, G.L. Chiarotti, P. Focher, S. Scandolo, E. Tosatti and M. Parrinello, *J. Phys. Chem. Solids* **56**, 501 (1995)

[40] O. H. Nielsen, R. M. Martin, *Phys. Rev. B* **32**, 3780 (1985)

[41] P. D. De Cicco and F. A. Johnson, *Proc. R. Soc. London Ser.*, **A 310**, 111 (1969)

[42] M. H. Cohen, R. Pick, and R. M. Martin, *Phys. Rev. B*, **1**, 910 (1970)

[43] H. Hellman, *Deuticke*, Leipzig, (1937)

[44] R. P. Feynman, *Phys. Rev.* **56**, 340 (1939)

[45] K. Kunc *et al.*, *Phys. Rev. Lett.* **48**, 406 (1982)

[46] D. R. Hamann, J. B. Bachelet, and M. Schlüter, *Phys. Rev. B* **26**, 4199 (1982)

[47] M. Schlüter, D. R.Hamann, and C. Chiang, *Phys. Rev. Lett* **43**, 1494 (1979)

[48] U. Von Barth and R. Car, *unpublished*

[49] G. B. Bachelet and N. E Christensen, *Phys. Rev. B*, **31**, 879 (1985)

[50] J. P. Perdew, K. Burke, and M. Ernzerhof, *Phys. Rev. Lett.* **77,** 3865 (1996)

[51] X. Gonze, P. Käckell, and M. Scheffler, *Phys. Rev. B* **41**, 12264 (1990)

[52] W. E. Pickett, *Comput. Phys. Rep* **9**, 115 (1989)

[53] `http://www.quantum-espresso.org`

[54] J. Maddox, *Nature* **335**, 201 (1988)

[55] Mulindwa Lister, *Crystal structure search and optimization using ab-initio methods*, Diploma thesis, ICTP, (2007)

[56] H. J. Monkhorst and J. D. Pack, *Phys. Rev. B* **13**, 5188 (1976)

[57] P. F. McMillan, *Nat. Mater.* **1**, 19 (2003)

[58] G. Miehe, A. Zerr, and R. Boehler, *Nature*, **400**, 340 (1999)

[59] L. Ouyang, P. Rulis, I. Tanaka, W. Ching, S. Mo, and M. Yoshiya, *J. Am. Ceram. Soc*, **85**, 78 (2002)

[60] S. K. Deb, G. Wolf, J. Dong, O. F. Sankey, and P. F. MacMillan, *Phys. Rev. B*, **61**, 11979 (2000)

[61] P. Kroll, *Phys. Rev. Lett.*, **90**, 125501 (2003)

[62] L. Ouyang, I. Tanaka, W. Y. Ching, S. Mo, and M. Yoshiya, *Phys. Rev. B*, **61**, 10609 (2000)

[63] B. M. Klein, D. A. Papaconstantopoulos, W. E. Pickett, and L. L. Boyer, *Phys. Rev. B*, **31**, 752 (1985)

[64] R. E. Gold, N. Pessal, and W. A. Reichardt, *J. Phys. Chem. Solids*, **29**, 19 (1968)

[65] H. Pierson, *Handbook of Refractory Carbides and Nitrides: Properties, Characteristics and Applications*' Noyes Publications, Westwood, N.J., (1996)

[66] W. Fuller, A. S. Edelstein, H. L. Luo, S. A. Wolf, and C. Y. Huang, *Phys. Rev. B*, **29**, 1443 (1984)

[67] G. Rubino, K. E. Grey, J. Zasadzinsky, R. Vaglio, and M. Russo, *Phys. Rev. B*, **32**, 2929 (1985)

[68] D. B. Dove, R. W. Nywening, T. Takamori, K. K. Shih, and M. E. Re, *j. Appl. Phys*, **68**, 2192 (1990)

[69] N. Greenwood and A. Earnshaw, *Chemistry of the Elements*, Butterworth-Heinemann, (1997)

[70] E. J. Friedman-Hill and R. W. Field, *j. Chem. Phys.*, **100**, 6141 (1994)

[71] W. D. Bare, A. Cintra, X. Wang, and L. Andrews, *j. Chem. Phys. A*, **105**, 7799 (2001)

[72] B. R.Sahu and L. Kleinman, *Phys. Rev. B* **71**, 041101 (2005)

[73] J. Uddin and G. E. Scuseria, *Phys. Rev. B* **72**, 035101 (2005)

[74] R. Yu and X. F. Zhang, *Appl. Phys. Lett.* **86**, 121913 (2005)

[75] S. Patil, private communications

[76] R. Yu and X. F. Zhang, *Phys. Rev. B* **72**, 054103 (2005)

[77] J. Crowhurst *et al.*, *Proc. Joint 20th AIRAPT 43rd EHPRG Int. Conf. on High Pressure and Technology*, FZK, Karlsruhe, (2005)

[78] D. Vanderbilt, *Phys. Rev. B* **41**, 7892 (1990)

[79] J. A. Montoya, Diploma Thesis, ICTP, Trieste - Italy (2004), available online at `http://eprints.ictp.it`

[80] A. Dewaele, P. Loubeyre, and M. Mezouar, *Phys. Rev. B* **70**, 094112 (2004)

[81] B. B. Karki *et al.*, *Amer. Mineral.* **82**, 51 (1997)

[82] J. M. Leger *et al.*, *Appl. Phys. Lett.* **79**, 2169 (2001)

[83] J. F. Nye, *Physical Properties of Crystals* Oxford University Press, Oxford, (1985)

[84] M. Lazzeri and F. Mauri, *Phys. Rev. Lett.* **90**, 036401 (2003)

[85] T. W. Barbee III, *Phys. Rev. B* **48** 9327 (1993)

[86] M. I. Eremets *et al.*, *Nat. Mater.* **3**, 558 (2004)

[87] J. Grossman *et al.*, *Phys. Rev. B* **60**, 6343–6347 (1999)

[88] E. Gregoryanz, A. Goncharov, R. J. Hemley, and H.-k. Mao, *Phys. Rev. B* **64**, 052103 (2001)

[89] V. P. Prakapenka, G. Shen, L. S. Dubrovinsky, M. L. Rivers, and S. R. Sutton, *J. Phys. Chem. Solids* **65**, 1537 (2004)

[90] H. Takizawa, T. Yamashita, K. Uheda, and T. Endo, *Phys. stat. sol.* **223**, 35 (2001)

[91] J. C. Crowhurst, A. F. Goncharov, B. Sadigh, C. L. Evans, P. G. Morrall, J. L. Ferreira, and A. J. Nelson, *Science* **311**, 1275 (2006)

[92] A. F. Young, J. A. Montoya, C. Sanloup, M. Lazzeri, E. Gregoryanz, and S. Scandolo, *Phys. Rev. B* **73**, 153102 (2006)

[93] R. Yu, Q. Zhan, and X.F. Zhang, *Appl. Phys. Lett.* **88**, 051913 (2006)

[94] D. A. Young, C.-S. Zha, R. Boehler, J. Yen, M. Nicol, A. S. Zinn, D. Schiferl, S. Kinkead, R. C. Hanson, and D. A. Pinnick, *Phys. Rev. B* **35**, R5353 (1987)

[95] P. Kroll, *J. Phys.:Condens. Matter* **16**, S1235 (2004)

[96] F. Occelli, D. L. Farber, J. Badro, C. M. Aracne, D. M. Teter, M. Hanfland, B. Canny, and B. Couzinet, *Phys. Rev. Lett.* **93**, 155501 (2004)

[97] E. Babaev, A. Sudbø, and N. W. Ashcroft, *Nature* **431**, 666 (2004)

[98] K. Shimizu, H. Ishikawa, D. Takao, T. Yagi, and K. Amaya, *Nature* **419**, 597 (2002)

[99] M. I. Eremets, V. V. Struzhkin, H.-k. Mao, and R. J. Hemley, *Science* **293**, 272 (2001)

[100] C. F. Richardson and N. W. Ashcroft, *Phys. Rev. Lett.* **78**, 118 (1997)

[101] J. Kortus, I. I. Mazin, K. D. Belashchenko, V. P. Antropov, and L. L. Boyer, *Phys. Rev. Lett.* **86**, 4656 (2001)

[102] J. Nagamatsu, N. Nakagawa, T. Muranaka, Y. Zenitani, and J. Akimitsu, *Nature* **410**, 63 (2001)

[103] E. A. Ekimov, V. A. Sidorov, E. D. Bauer, N. N. Mel'nik, N. J. Curro, J. D. Thompson, and S. M. Stishov, *Nature* **428**, 542 (2004)

[104] E. Bustarret, C. Marcenat, P. Achatz, J. Kačmarčik, F. Lévy, A. Huxley, L. Ortéga, E. Bourgeois, X. Blase, D. Débarre, and J. Boulmer, *Nature* **444**, 465 (2006)

[105] T. E. Weller, M. Ellerby, S. S. Saxena, R. P. Smith, and N. T. Skipper, *Nat. Phys.* **1**, 39 (2005)

[106] M. I. Eremets, A. G. Gavriliuk, I. A. Trojan, D. A. Dzivenko, and R. Boehler, *Nat. Mater.* **3**, 558 (2004)

[107] M. I. Eremets, R. J. Hemley, H.-k. Mao, and E. Gregoryanz, *Nature* **411**, 170 (2001)

[108] J. A. Montoya, A. D. Hernandez, C. Sanloup, E. Gregoryanz, and S. Scandolo, *Appl. Phys. Lett.* **90**, 011909 (2007)

[109] McMillan, *Phys. Rev.* **167**, 331 (1968)

[110] C. W. Chu, W. L. McMillan, and H. L. Luo, *Phys. Rev. B* **3**, 3757 (1971)

[111] M. Santoro *et al.*, *J. Chem. Phys.* **121**, 2780 (2004)

[112] M. Santoro and F. A. Gorelli, *Chem. Soc. Rev.* **35**, 918 (2006)

[113] V. Giordano and F. Datchi, *Europhys. Lett.* **77**, 46002 (2007)

[114] C.-S. Yoo *et al.*, *Phys. Rev. Lett.* **83**, 5527 (1999)

[115] M. R. Battaglia, *Mol. Phys.* **43**, 1015 (1981)

[116] O. Mishima, L. D. Calvert, and E. Whalley, *Nature* **310**, 393 (1984)

[117] R. J. Hemley, A. P. Jephcoat, H.-k. Mao, L. C. Ming, and M. H. Mangh-nani, *Nature* **334**, 52 (1988)

[118] P. F. McMillan, *Nature* **441**, 823 (2006)

[119] S. Serra *et al.*, *Science* **284**, 788 (1999)

[120] B. Holm *et al.*, *Phys. Rev. Lett.* **85**, 1258 (2000)

[121] J. Dong, J. K. Tomfohr, and O. F. Sankey, *Science* **287**, 11a (2000)

[122] J. Dong, J. K. Tomfohr, and O. F. Sankey, *Phys. Rev. B* **61**, 5967 (2000)

[123] J. Dong *et al.*, *Phys. Rev. B* **62**, 14685 (2000)

[124] O. Tschauner, H.-k. Mao, and R. J. Hemley, *Phys. Rev. Lett.* **87**, 075701 (2001)

[125] H.-k. Mao *et al.*, *J. Appl. Phys.* **49**, 3276 (1978)

[126] R. Bini *et al.*, *Rev. Sci. Instrum.* **68**, 3154 (1997)

[127] F. A. Gorelli *et al.*, *Phys. Rev. Lett.* **83**, 4093 (1999)

[128] Q. Williams *et al.*, *J. Geophys. Res.* **98**, 22,157 (1993)

[129] D. M. Teter *et al.*, *Phys. Rev. Lett.* **80**, 2145 (1998)

[130] F. Tassone *et al.*, *Chem. Phys. Chem.* **6**, 1752 (2005)

[131] G. R. Gathers, N. C. Holmes, J. A. Moriarti, and W. J. Nellis *J. Appl. Phys* **66**, 2962 (1989).

[132] D. Young, *Phase Diagrams of Elements*, University of California Press, Berkeley, (1991)

[133] C. Kittel, *Introduction to Solid State Physics*, Wiley, N.Y, (1976)

[134] D. J. Steinberg, *J. Chem. Phys. Sol.* **43**, 1173 (1982)

[135] N. S. Banger, N. Singh, and S. P. Singh, *Phys. Rev. B* **38**, 7415 (1988)

[136] B. N. Brockhouse, D. H. Dutton, and A. P. Miller, *Can. J. Phys.* **50**, 2915 (1972)

[137] M. Bernasconi, G.L. Chiarotti, P. Focher, S. Scandolo, E. Tosatti, and M. Parrinello, *J. Phys. Chem. Solids* **56**, 501 (1995)

[138] R. Martonak, J. A. Montoya, S. Scandolo, E. Tosatti, *unpublished*